

**VIRTUAL EARTHQUAKE ENGINEERING LABORATORY
WITH PHYSICS-BASED DEGRADING MATERIALS
ON PARALLEL COMPUTERS**

Thesis by

In Ho Cho

In Partial Fulfillment of the Requirements

for the Degree of

Doctor of Philosophy



California Institute of Technology

Pasadena, California

2012

(Defended January 25, 2012)

© 2012

In Ho Cho

All Rights Reserved

To Jesus from whom the wisdom comes;
To my family from whom my happiness comes

Acknowledgements

I'm deeply grateful to Professor Hall. He has been always fully supportive and willing to provide warm advice and suggestion, which actually turned out to be instrumental for my research outcome. Thanks also go to Professor Krishnan for his persistent support about parallel computers. Indeed, his persistent support and sharp advice are essential for my bold attempt. I'm really grateful to Professor Heaton and Professor Beck for their warm encouragement throughout the years in Caltech. I'm pretty sure I won't find better faculty members in any school all around the world. Special thank also goes to Dr. Aivazis for his wonderful class about parallel algorithm and kind support as a committee member.

It was you guys, Vanessa and Gokcan that I can happily stay here in Caltech for last four years, and thank you so much.

I'd like to express my love to my parents. You are the origin of my strength and all my creativity; your love is the origin of my happiness. It is the unconditional trust of my sister and brother that make me be strong and bold. I love you guys. Also, I'm deeply grateful to you, mother-in-law because I can always hear your voice of prayer.

I love you Jiwon. Without you, I was definitely not able to reach this moment. Also, I can't journey on in this evanescent place without your love. You already completed me more than I ever imagined.

I love you Erin and Joel more than any other earthly things. You are the most precious blessing to me. I hope you to remember that thanks to your smile, I can live and breathe every single moment.

Abstract

For the last few decades, we have obtained tremendous insight into underlying microscopic mechanisms of degrading quasi-brittle materials from persistent and near-saintly efforts in laboratories, and at the same time we have seen unprecedented evolution in computational technology such as massively parallel computers. Thus, time is ripe to embark on a novel approach to settle unanswered questions, especially for the earthquake engineering community, by harmoniously combining the microphysics mechanisms with advanced parallel computing technology.

To begin with, it should be stressed that we placed a great deal of emphasis on preserving clear meaning and physical counterparts of all the microscopic material models proposed herein, since it is directly tied to the belief that by doing so, the more physical mechanisms we incorporate, the better prediction we can obtain.

We departed from reviewing representative microscopic analysis methodologies, selecting out “*fixed-type*” multidirectional smeared crack model as the base framework for nonlinear quasi-brittle materials, since it is widely believed to best retain the physical nature of actual cracks. Microscopic stress functions are proposed by integrating well-received existing models to update normal stresses on the crack surfaces (three orthogonal surfaces are allowed to initiate herein) under cyclic loading.

Unlike the normal stress update, special attention had to be paid to the shear stress update on the crack surfaces, due primarily to the well-known pathological nature of the fixed-type smeared crack model—spurious large stress transfer over the open crack under nonproportional loading. In hopes of exploiting physical mechanism to resolve this deleterious nature of the fixed crack model, a tribology-inspired three-dimensional (3d) interlocking mechanism has been proposed. Following the main trend of tribology (i.e., the science and engineering of interacting surfaces), we introduced the base fabric of solid particle-soft matrix to explain realistic interlocking over rough crack surfaces, and the adopted Gaussian distribution feeds random particle sizes to the

entire domain. Validation against a well-documented rough crack experiment reveals promising accuracy of the proposed 3d interlocking model.

A consumed energy-based damage model has been proposed for the weak correlation between the normal and shear stresses on the crack surfaces, and also for describing the nature of irrecoverable damage. Since the evaluation of the consumed energy is directly linked to the microscopic deformation, which can be efficiently tracked on the crack surfaces, the proposed damage model is believed to provide a more physical interpretation than existing damage mechanics, which fundamentally stem from mathematical derivation with few physical counterparts.

Another novel point of the present work lies in the topological transition-based “*smart*” steel bar model, notably with evolving compressive buckling length. We presented a systematic framework of information flow between the key ingredients of composite materials (i.e., steel bar and its surrounding concrete elements). The smart steel model suggested can incorporate smooth transition during reversal loading, tensile rupture, early buckling after reversal from excessive tensile loading, and even compressive buckling. Especially, the buckling length is made to evolve according to the damage states of the surrounding elements of each bar, while all other dominant models leave the length unchanged.

What lies behind all the aforementioned novel attempts is, of course, the problem-optimized parallel platform. In fact, the parallel computing in our field has been restricted to monotonic shock or blast loading with explicit algorithm which is characteristically feasible to be parallelized. In the present study, efficient parallelization strategies for the highly demanding implicit nonlinear finite element analysis (FEA) program for real-scale reinforced concrete (RC) structures under cyclic loading are proposed. Quantitative comparison of state-of-the-art parallel strategies, in terms of factorization, had been carried out, leading to the problem-optimized solver, which is successfully embracing the penalty method and banded nature. Particularly, the penalty method employed imparts considerable smoothness to the global response, which yields a practical superiority of the parallel triangular system solver over other advanced solvers such as parallel preconditioned conjugate gradient method. Other salient issues on parallelization are also addressed.

The parallel platform established offers unprecedented access to simulations of real-scale structures, giving new understanding about the physics-based mechanisms adopted and probabilistic randomness at the entire system level. Particularly, the platform enables bold simulations of real-scale RC structures exposed to cyclic loading—H-shaped wall system and 4-story T-shaped wall system. The simulations show the desired capability of accurate prediction of global force-displacement responses, postpeak softening behavior, and compressive buckling of longitudinal steel bars. It is fascinating to see that intrinsic randomness of the 3d interlocking model appears to cause “*localized*” damage of the real-scale structures, which is consistent with reported observations in different fields such as granular media.

Equipped with accuracy, stability and scalability as demonstrated so far, the parallel platform is believed to serve as a fertile ground for the introducing of further physical mechanisms into various research fields as well as the earthquake engineering community. In the near future, it can be further expanded to run in concert with reliable FEA programs such as *FRAME3d* or *OPENSEES*. Following the central notion of “*multiscale*” analysis technique, actual infrastructures exposed to extreme natural hazard can be successfully tackled by this next generation analysis tool—the harmonious union of the parallel platform and a general FEA program. At the same time, any type of experiments can be easily conducted by this “*virtual laboratory*.”

Table of Contents

List of Figures	xi
List of Tables	xvi
Chapter 1 INTRODUCTION	1
Chapter 2 PHYSICS-BASED DEGRADING MATERIAL MODELS	6
2.1 Review of Microscopic Material Models	6
2.1.1 Continuum Elastoplastic Models	8
2.1.2 Smeared Crack Models	10
2.1.3 Particle-Lattice Models	13
2.2 Outline of Physics-Based Degrading Material Model	14
2.3 Revisit to “Fixed-Type” Multidirectional Smeared Crack Model	15
2.3.1 Hybrid Domain Concept	15
2.3.2 Strains on the Crack Surfaces and Criterion for Mode-I Cracking	16
2.3.3 Stress Update on the Crack Surfaces	17
2.4 Damage Models	24
2.4.1 Review of Damage Models	24
2.4.2 Consumed Energy-Based Damage Model	28
2.5 Poisson Effect and Transformation to Crack Coordinates	31
2.6 3d Interlocking Model for Nonlinear Shear	35
2.6.1 Random Particle Distribution	41
2.6.2 Interlocking during Cyclic Movement	44
2.6.3 Validation against an Interlocking Experiment	46

2.6.4	Effect of Number of Elements and Mean Diameter of Particles	48
2.7	“Smart” Reinforcing Steel Bar Model.....	50
2.7.1	Review of Previous Research	50
2.7.2	Challenges of Existing Models	53
2.7.3	Definition of Topological Group	55
2.7.4	Topological Transition: Longitudinal Bar Type	58
2.7.5	Remarks on Parallel Implementation.....	61
2.7.6	Generalized Menegotto-Pinto Steel Model.....	63
2.7.7	Example of Topological Transition-Based Buckling.....	66
2.7.8	Steel Bar Models Implemented in the Present Work.....	68
Chapter 3	PARALLELIZATION STRATEGIES	69
3.1	Outline of Parallel Platform Developed	69
3.2	Review of Parallel Computing in Broader Fields.....	71
3.3	Key Characteristics of the Serial Version Program.....	74
3.4	Quantitative Study on the Advanced Parallelization Strategies	76
3.5	Cost Model for Parallel Factorization	79
3.5.1	Behavior of Cyclic Allocation Scheme.....	79
3.5.2	Total Cost of Parallel Factorization with Cyclic Allocation.....	81
3.6	Optimized Parallel Factorizations with “Super Linear” Speedup	83
3.7	Parallel Triangular System Solving versus Parallel PCGM	86
3.8	“Divide-and-Conquer” for Embarrassingly Parallelizable Procedures	90
3.9	Issues on Load Balance and Error from Parallelization	94
3.10	Physical Mechanisms and Randomness Fed by Parallelization	95
3.11	Concluding Remarks about Parallelization Strategies	97

Chapter 4	APPLICATIONS TO REAL-SCALE STRUCTURES	98
4.1	H-Shaped Wall System under Cyclic Loading.....	98
4.2	4-story T-Shaped Wall System under Cyclic Loading.....	108
Chapter 5	CONCLUSION AND FUTURE DIRECTION	116
5.1	Conclusion.....	116
5.2	Future Directions.....	119
Appendices.....		120
Appendix A	Examples of poisson effect by equivalent strain method.....	120
Appendix B	Steel bar models	123
Appendix C	Detailed pseudocodes of parallel factorizations.....	128
Appendix D	Partial pipelined parallel factorization for banded system.....	134
Bibliography		138

List of Figures

Figure 1.1. Elementary school severely damaged by the M_w (moment magnitude) 7.0 Tahiti earthquake of January 12, 2010, showing the localized shear failure on shear wall system and a column on second floor (from USGS/EERI report 2010).	1
Figure 2.1. Microscopic numerical analysis methodologies, plotted over corresponding length scale and degree of physical counterparts required to calibrate salient parameters and to interpret prediction generated.	7
Figure 2.2. Schematic example of embedded crack trajectory (in bold straight line) with enforced continuity of the crack path attained from nonlocal strain concept.	8
Figure 2.3. Increasing deviation of crack surface direction from that of current principal strains: (a) representative volume of quasi-brittle material under shear; (b) after the onset of tensile crack, the compressive principal strain $\epsilon_3 \approx 0$ and direction of crack surface is almost coincident with that of principal strains; (c) under excessive shear, considerable difference between the two directions develops; (d) schematic illustration of microplanes at microscopic length scale for comparison.	10
Figure 2.4. Hybrid domain concept for microscopic stress evaluation on the crack surfaces: (Right top) Homogeneous domain for normal stresses and (Right bottom) heterogeneous domain impregnated with random particles for 3d interlocking to update shear stresses (Left: real-scale RC structure damaged by cyclic loading, from Palermo and Vecchio 2002).	16
Figure 2.5. Nonlinear tension softening model.	19
Figure 2.6. Work done by Mode-I cracking opening with nonlinear softening.	20
Figure 2.7. Microscopic stress function based on Thorenfeldt compression model augmented by tension regime and un/reloading paths (Left); sensitivity of curve shape to strengths (Right).	22
Figure 2.8. Tensile resistance development depending on previous compressive damage.	23
Figure 2.9. Progressive damage in matrix in vicinity of ideal sphere.	28
Figure 2.10. Interpretation of damage factor d as an area ratio, and possible inclusion of the lateral confinement/hydraulic pressure dependence by the expansion of stress function g . $d_{ic} (\geq 0)$ stands for the degree of the initial lateral confinement.	30
Figure 2.11 Example of stress update with Poisson effect consideration	34

Figure 2.12. The base couple of rigid particle-soft matrix for 3d interlocking model being proposed herein (Left); Typical asperity model in tribology for comparison (Right).	35
Figure 2.13. Permanent plastic damage to the soft matrix by cyclic movement.....	35
Figure 2.14. Micrographs revealing micro-cracking along the aggregate boundaries of a concrete specimen: (Top) Actual cross section of concrete specimen showing crack patterns emphasized by arrows; (Bottom) Clearly visible cracks after image processing (from Elkadi 2005).....	36
Figure 2.15. Projections of contacting area of the ideal hemisphere with diameter D_{max}	37
Figure 2.16. Degradation of tangent shear stiffness with several friction coefficients: (a) when 3d hemisphere is used; (b) 2D semicircle is adopted for interlocking mechanism, exhibiting relatively stiff nature than that with 3d hemisphere.....	39
Figure 2.17. Variation of tangent shear stiffness depending on crack opening.	39
Figure 2.18. Interlocking states during cyclic loading (all shear strain and shear stress terms signify those on the crack surfaces).	44
Figure 2.19. Validation setup of 3d interlocking model against experiment: (a) actual experimental specimen; (b) numerical modeling of specimen with initial Mode-I crack, marked by arrows in the middle layer [for visualization purpose, only 25 element blocks are shown]; (c) random particle distribution along the middle layer of 2500 elements....	47
Figure 2.20. Horizontal slip-resultant force responses (force is represented by corresponding shear stress).....	47
Figure 2.21. Normalized maximum horizontal forces with varying element numbers for two random particle distributions—Normal and Uniform distributions.....	49
Figure 2.22. Effect of particle size on resultant horizontal force from 3d interlocking model.....	49
Figure 2.23. Initiation of compressive buckling and postbuckling behavior of longitudinal steel bar under compression (adapted from Dhakal and Maekawa 2002a).....	51
Figure 2.24. Study of reinforcing steel bar system from the idealized to realistic case: (a) typical reinforcing bar test setup with single spacing; (b) simplified bar system with horizontal ties represented by ideal springs; (c) realistic reinforced system of composite material..	53
Figure 2.25. Basic topological groups: (Left) longitudinal steel group with initial buckling lengths initially assigned; (Right) The set of base unit consisting of one bar and its surrounding elements set.....	57

Figure 2.26. Criterion for topological transition according to damage on surrounding elements (gray color signifies at least partially crushed state of the element while white relatively intact state).....	58
Figure 2.27. Example of topological transition and evolving buckling lengths.	60
Figure 2.28. Schematic description of parallel update of compressive buckling of steel bars by means of “ <i>master-slaves</i> ” strategy.....	61
Figure 2.29. Longitudinal steel hysteresis model with compressive buckling and tensile rupture.....	63
Figure 2.30. Contrast between buckling modes intentionally generated: (Middle) a cyclically loaded column consisting of a longitudinal steel bar and three layers of surrounding elements; (Left) when two bottom layers failed first; (Right) only bottom layer failed...	66
Figure 2.31. Predicted stress-strain response revealing different buckling lengths triggered by topological transition (Left), which are based on the compressive failure of surrounding elements (Right).....	67
Figure 2.32. Onset of early buckling captured by the simulations revealing distinct initiation point of buckling due primarily to evolving buckling length by topological transition.....	67
Figure 3.1. Nonoverlapping domain/tasks decomposition strategy, widely used in “ <i>explicit</i> ” algorithms.	72
Figure 3.2. Coarse-grained domain/tasks decomposition strategy (e.g., used in hierarchical multiscale analysis), notably with the distinct communication schemes.	72
Figure 3.3. Partially overlapping domain/tasks decomposition strategy (e.g., some GIS algorithms with intrinsic “ <i>nonlocality</i> ”).	73
Figure 3.4. Costs of parallel factorizations attained from numerical simulations of a test system (size=2040): parallel Gaussian elimination (dashed line) and parallel factorization followed by triangular system solving (solid line).....	77
Figure 3.5. Costs of look-ahead and pipelined factorization normalized by that of broadcasting method, all attained from simulations of a test system (size = 19176).....	78
Figure 3.6. Super linear speedup attained from simulations of a test structure (system size $n = 32400$; bandwidth = 8145).....	85
Figure 3.7. Cost comparison between parallel PCGM and parallel triangular system solving.....	89
Figure 3.8. Master-slaves for all trivially parallelizable tasks along with nonoverlap uniform domain decomposition.	91

Figure 3.9. Speedup in nonlinear element updating procedure by “ <i>divide-and-conquer</i> ” strategy, attained from simulations of a test model consisting of 2784 concrete and 3372 steel bar elements.....	91
Figure 3.10. Column-based cyclic allocation on all processors for factorization and solving.....	92
Figure 3.11. (a) Thorenfeldt compressive model generalized by un/reloading model; (b) tension softening regime defined on three orthogonal crack surfaces; (c) the fabric of rigid hemisphere-soft indentation proposed by the authors for nonlinear shear across opened crack; (d) Reinforcing steel bar model incorporating compressive buckling.	96
Figure 4.1. H-shaped wall system (DP1) details.....	99
Figure 4.2. Reinforcement layout for H-shaped wall system (DP1).....	100
Figure 4.3. Unstructured random distribution of ideal particles over entire H-shaped RC wall system; the random particles are intended to realize the irregular asperity configuration, not the actual aggregate sizes.....	101
Figure 4.4. Applied displacement history to DP1 (by courtesy of D. Palermo and F. J. Vecchio).102	
Figure 4.5. Ultimate damage on flange part showing U-shaped and flexural cracking (Palermo and Vecchio 2002, with permission from ACI publishing).	102
Figure 4.6. Ultimate damage on web part exhibiting distributed diagonal cracks and localized sliding planes with vertical directivity (Palermo and Vecchio 2002, with permission from ACI Publishing).	103
Figure 4.7. Effect of 3d interlocking model on the global force-displacement responses (simulated up to 12 mm near the peak load-carrying capacity).....	104
Figure 4.8. Deformed shape (amplified) with/without 3d interlocking model (Note: by introducing the 3d interlocking mechanism, the localized damage with vertical directivity marked in dashed arrow can be captured).....	105
Figure 4.9. Cost plot of factorization and nonlinear element update after normalization by the cost for $p = 16$	106
Figure 4.10. Influence of damage model on the rapid postpeak softening response (both simulations includes 3d interlocking model, run up to 15 mm).....	107
Figure 4.11. Overall geometry of TW2.....	108
Figure 4.12. Reinforcing bar details with all cover concrete thickness 19 mm.	109

Figure 4.13. Applied displacement history (TW2).	110
Figure 4.14. Effect of 3d interlocking model on global force-displacement response; Negative displacement corresponds to the case of flange under tension while the positive range signifies flange under compression, as depicted in insets.....	112
Figure 4.15. Deformed shape (amplified) at the last step of the simulation, revealing concentrated severe damage at boundary part of web and localized damage with diagonal directivity (marked by dashed arrows) by virtue of 3d interlocking model.	112
Figure 4.16. Contrast of stress-strain responses from longitudinal steel bars depending on the locations: the outermost positions of web toe (left) and of flange (right); Superimposed plot of deformed steel bars at bottom floor only (top).....	114
Figure 4.17. Evolution of compressive buckling length of the longitudinal steel at the outermost position of web toe; right inset shows actual damage states of the specimen (from Thomsen and Wallace 2004).	115

List of Tables

Table 2.1. Steel bar type definition and characteristics	54
Table 2.2. Data structure in smart steel bar model.....	60
Table 3.1. Flow of serial version of displacement-controlled nonlinear FEA program.....	74
Table 3.2. Total time cost comparison of full-/partial- parallel factorizations without/with prudent numbering [sec]	84
Table 3.3. Pseudocode of the optimized parallel algorithm for the upper triangular system, successfully exploiting column-based cyclic distribution and banded nature	86
Table 3.4. Pseudocode of parallel PCGM for $\mathbf{Kx} = \mathbf{b}$	87
Table 3.5. Cost of parallel PCGM, parallel factorization, and parallel triangular system solving in [sec] (system size $n = 32400$; bandwidth = 8145).	88
Table 4.1. Concrete material property (DP1).....	100
Table 4.2. Steel material property (DP1)	100
Table 4.3. Concrete material property (TW2).....	109
Table 4.4. Steel material property (TW2)	110

Chapter 1 INTRODUCTION

Nonlinear analysis of complicated structures, especially involving irrecoverable damage and disintegration phenomena such as cracking and crushing, has been of central importance in a wide range of fields in science and engineering. Particularly, in the earthquake engineering community, accurate numerical simulation plays an essential role in increasing resilience of infrastructures during design stage, providing the optimal rehabilitation remedy, and even generating precise probabilistic fragility curves for loss estimation process—all against the most catastrophic and yet unpredictable natural hazard, earthquake.

As shown in figure 1.1, nonlinear shear and localized damage phenomena are still long-standing challenges of earthquake engineering field. As a demonstrative example, the key assumption of the popular fiber section model (i.e., plane section remains plane after deformation) hardly captures the abrupt emergence of localized cracks and highly disturbed strain fields on the domain.



Figure 1.1. Elementary school severely damaged by the M_w (moment magnitude) 7.0 Tahiti earthquake of January 12, 2010, showing the localized shear failure on shear wall system and a column on second floor (from USGS/EERI report 2010).

In the present study, a novel attempt has been made by developing a parallel simulation platform for nonlinear implicit finite element analysis of real-scale 3d RC structures. The uniqueness of this parallel platform lies in the fact that (1) it is almost the first parallel platform in terms of implicit nonlinear analysis of real-scale RC structures exposed to cyclic loading; (2) special attention has been paid to contain as much physically reasonable micromechanics as

possible in describing nonlinear behavior of materials; (3) it naturally holds unlimited extensibility to embrace more realistic phenomena such as compressive buckling of steel bars, localized failure of the domain with random material properties, etc.

Indeed, for the last decades we have seen tremendous progress in computing technology for solving engineering and scientific problems, which enables us to conduct numerical simulation of virtually any real-scale structures under extreme loadings. Furthermore, a multitude of sophisticated outcomes from persistent laboratory experiments provide unprecedented insight into microscopic damage mechanisms, which underlie random failure and localized damage phenomena of real-world structures. By virtue of such advances in different frontiers, time is ripe to embark on a bold attempt to directly link microscopic physics to real-scale structures exposed to extreme conditions, and to validate the physical mechanisms against “*actual*” structures of interest, rather than against idealized and controlled laboratory scale specimens.

In the present study, we made an attempt to incorporate as much microscopic, physical mechanisms as possible with the aid of elaborately optimized parallel computing technology. In some sense, the parallel platform calls for novel material models which are essentially rooted in physically reasonable mechanisms for degrading material phenomena. Otherwise, the parallel platform would merely become an assembly of a large number of processors, only saving the computation cost and reproducing “*expected*” responses from the idealized governing mechanisms. However, provided that the parallel simulation platform is made to play in concert with physical mechanisms, it is fundamentally certain that the more physical mechanisms are used, the more accurate prediction the platform will generate.

In chapter 2, we summarize existing microscopic analysis methodologies, particularly for quasi-brittle degrading materials, along with their strengths and shortcomings. Special attention has been paid to how much they hold “*physical counterparts*.” In light of the systematic review, we have chosen the multidirectional smeared crack model as the base mechanisms to describe the degrading quasi-brittle materials. Especially, we revisited “*fixed-type*” multidirectional smeared crack model, mainly to preserve the physical interpretation of real cracks, normally found from structures exposed to cyclic loading. To resolve the well-known pathological nature of the fixed-type smeared crack model, notably by means of a physically reasonable mechanism, we proposed

the tribology-inspired 3d interlocking model. Following the central notion of smeared crack model, all the nonlinearity of material is explained on the reduced crack surfaces and reliable microscopic stress functions are harmoniously suggested to give rise to an integrated normal stress-strain relationship on the crack surfaces.

Particularly, in section 2.6, we develop 3d interlocking mechanism. As mentioned before, the fixed-type smeared crack model holds pathological nature—namely, spurious large shear stress transfer over the open cracks when exposed to nonproportional loading. In fact, resolving this problem by use of physically plausible mechanism was the key motivation of the 3d interlocking model. Inspired by the main trend of tribology, we adopted the base fabric of rigid particle-soft matrix, of which interaction generates nonlinear shear stress on crack surfaces during cyclic loading. As many researchers in tribology utilized the Gaussian distribution to form the random asperity of rough crack surfaces, we used the Gaussian distribution to generate random particle sizes and then distributed them, notably over “*entire*” domain. To this aim, a hybrid domain assumption was made, which consists of two domains: homogeneous domain for normal stress on the crack surfaces and heterogeneous domain for shear stress on the crack surfaces. Validation of the 3d interlocking mechanism proposed has been carried out against a well-known rough crack experiment, revealing remarkable accuracy and possibility of the model.

In section 2.4, consumed energy based damage model is suggested. The damage model is bridging the gap between the normal and shear stress on the crack surfaces, which are weakly correlated on the hybrid domain assumption. The idea is based on the fact that “*damage*” is global and universal quantity and also can be represented by a tractable value such as scalar quantity, as widely done in damage mechanics. It is noteworthy that the proposed quantity for damage is explicitly rooted in consumed energy of the material, not in the implicit one such as the mathematically driven quantity. Therefore, the damage model proposed herein also holds clear physical counterparts in accordance with the main philosophy of the present parallel platform.

Section 2.7 suggests a “*smart*” reinforcing steel bar model under cyclic loading. Departing from well-established knowledge from a multitude of researchers, we integrate the advantageous characteristics of the existing models, giving rise to a generalized Menegotto-Pinto steel model with evolving buckling length. Compressive buckling is taken into account in conjunction with

progressive damage of surrounding quasi-brittle materials. Loss of adhesive energy of materials near the longitudinal steel bars is interactively and comprehensively considered to determine realistic evolution of buckling length at a specific time. In some sense, this provides a systematic platform of information flow between structural constituents of composite structures (e.g., between steel bars and surrounding concretes in the present application).

Chapter 3 is mainly concerned with parallelization strategies. It deals with the optimization of parallel algorithms to best fit the present problem, which can be characterized by “*implicit*” solving, considerably expensive cost in terms of memory and computation, displacement control strategy, penalty method employed for enhanced stability, and most important, highly nonlinear material behavior. We started from comprehensive comparison study on the advanced parallel algorithms, and then we tuned the selected pipelined algorithm to successfully embrace advantageous natures of the problem. Applications of the optimized algorithm to real-scale structures proved promising possibility of the parallel platform with desired scalability and parallel efficiency in nonlinear element-related tasks.

In chapter 4, we present applications of the platform to study real-scale RC structures loaded by inverted cyclic displacements up to severely damaged states—i.e., 3d H-shaped wall system and 4-story T-shaped wall system. Results from the numerical simulations confirm that the well-known pathological nature of fixed-type smeared crack model has been successfully resolved by the inclusion of 3d interlocking mechanism. It is also fascinating to observe that the randomness of particles, distributed over the entire domain for the 3d interlocking mechanism, appears to play an essential role to cause apparently “*localized*” damage, while the damage would otherwise happen in a smoothly scattered manner.

As demonstrated so far, harmonious combination of advanced parallel computing technology and microphysical mechanisms sparks our imagination as regards next steps.

Embracing more physical mechanisms —e.g., lateral confinement effect and hydraulic pressure dependence as well as parallel strategies for their nonlocal formulations—shall be natural extension of the present work. Furthermore, in the future research, we shall transplant the present

parallel platform into the well-established general analysis platform (e.g., *FRAME3d* or *Opensees*) for efficiently dealing with actual infrastructures of interest. In this fashion, we can conduct hazard analysis of any infrastructure subject to seismic loading, with unprecedented accuracy and efficiency. Specifically, in the attempt, major portion of the structure shall be handled by the general FEA platform while a specific critical portion of the structure will be investigated by the parallel platform in great detail. To some extent, such an analysis flow can be thought of as a real-scale extension of the notion of “*multiscale*” analysis technique. Eventually, this novel attempt will open the way to the “*virtual laboratory*” establishing the next-generation analysis platform.

Chapter 2 PHYSICS-BASED DEGRADING MATERIAL MODELS

2.1 *Review of Microscopic Material Models*

Before embarking upon detailed review of the microscopic analysis methodologies for degrading quasi-brittle materials, it is instructive to touch upon the other pole—the macroscopic and phenomenological methodology, particularly dominant in the earthquake engineering community. As an early effort, the global force-displacement responses of reinforced concrete (RC) structures were represented by heuristic hysteresis models in the form of nonlinear springs (Cheng et al. 1993) or equivalent beam-column systems (Colotti 1993). Recently, the most advanced and widely used one is the fiber section model (e.g., Gan and Hall 1995; Krishnan 2010), and especially for the degradation phenomena of RC beam-column (see a review by Spacone and El-Tawil 2004) the fiber section model has proved successful and efficient tool. Even slender RC wall system had been analyzed by the fiber section model by incorporating nonlinear spring (e.g., Orakcal and Wallace 2006). However, the fundamental assumption behind their formulations—plane section remains plane after deformation—poses an important challenge to general applications where shear effect is essential in nonlinear degradation. Although such macroscopic and phenomenological approaches are still dominant in practice, it is believed that they will gradually give the way to highly sophisticated and general microscopic approaches with the aid of evolution of computing capacity, just as what fiber section model has done for the last decades.

Turning to the microscopic approaches, we can classify the mainstreams into three categories: (1) continuum elastoplastic models, (2) smeared crack models with planes of degradation, and (3) particle and lattice models. The order of this category is intentionally organized to represent how much the formulation is sophisticated, especially with respect to physical aspects of cracks.

Figure 2.1 schematically illustrates the length scale of each representative simulation methodology along with degree of physical counterparts that is required to calibrate salient parameters or to interpret the responses predicted.

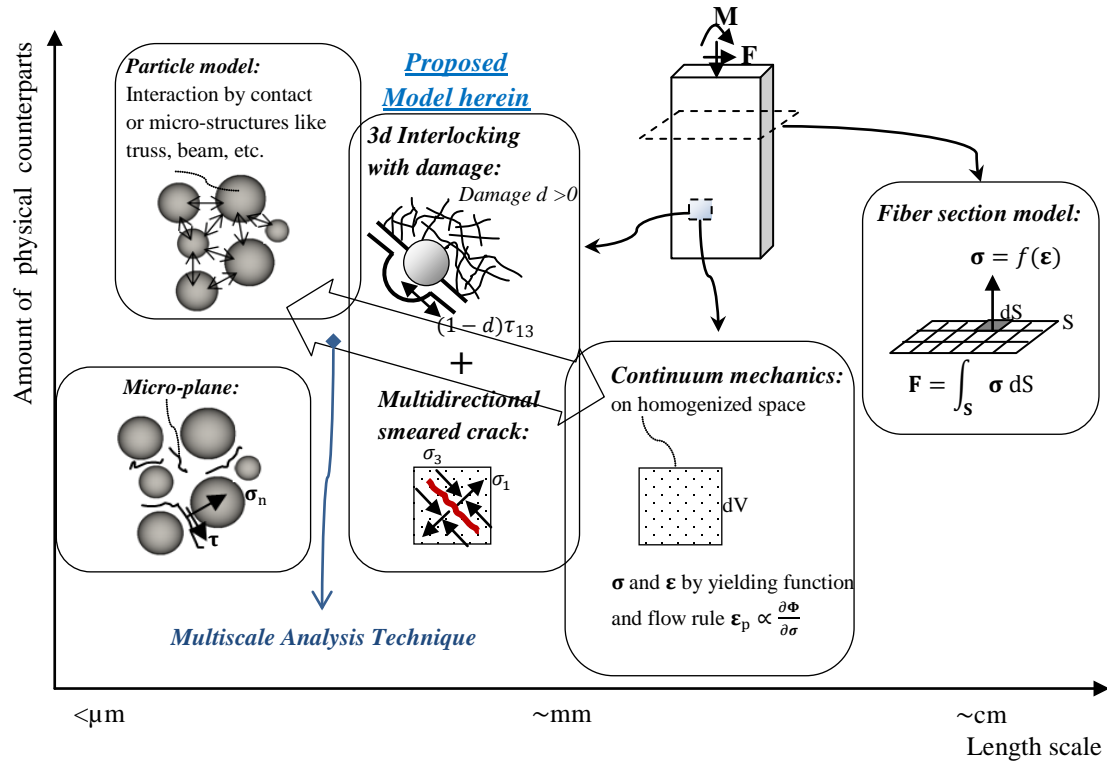


Figure 2.1. Microscopic numerical analysis methodologies, plotted over corresponding length scale and degree of physical counterparts required to calibrate salient parameters and to interpret prediction generated.

2.1.1 Continuum Elastoplastic Models

As the first category of representative microscopic approaches, we can find extensive effort to embrace nonlinear damage process into the continuum elastoplastic framework: one is referred to, for instance, papers by Simo and Ju (1987a, 1987b) for quasi-brittle material, Steglich et al. (2005) for ductile material under cyclic loading, and Hicher et al. (2008) for soils exposed to cyclic force. Even localized phenomena such as shear band were embedded within an element level with a specific emergence criterion which is based on the mathematical condition of tangent stiffness $D_{ijkl}^{(T)}$ and geometric information of the slip (e.g., Ortiz 1987; Jirásek 1998). Such embedded cracks at element level are used to describe discrete cracks after finding crack direction and jump in displacement gradient which altogether met the localized failure criteria as

$$[\dot{\epsilon}_{ij}] = D_{ijkl}^{(T)} [\dot{\epsilon}_{kl}], \quad (2.1)$$

where strain rate jump has kinematic relationship with discontinuity direction \mathbf{n} and displacement gradient jump \mathbf{g} as $[\epsilon_{ij}] = 1/2(g_i n_j + g_j n_i)$.

This approach is regarded to be good for predicting localized failure of general materials, and even it is able to successfully capture the localized crack with continuous path across adjacent elements as depicted in figure 2.2. However, it is extremely sensitive to the tangent stiffness matrix adopted, which causes difficulty in applying this elegant method to RC structures undergoing severely damaged states by cyclic/seismic loading. Moreover, from the physical perspective, when subjected to cyclic or seismic loading, the damage often appears to be localized on a number of specific zones through crushing and pulverization rather than a simple line within an element.

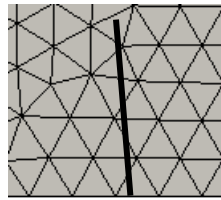


Figure 2.2. Schematic example of embedded crack trajectory (in bold straight line) with enforced continuity of the crack path attained from nonlocal strain concept.

In sum, one of the major advantages of the continuum-based approach is that it holds broad applicability to complicated three-dimensional structures, even subject to a wide range of multidirectional forces. Most of the continuum-based approaches, however, are significantly sensitive to the tangent stiffness, and there exists difficulty in handling the evolution of yielding surface under cyclic loading. Physical and realistic failure process such as fragmentation of quasi-

brittle materials are also hard to be explained by the continuum approaches with classical plasticity theories. Furthermore, many decisive parameters for yield function and flow rule are generally intractable since it is not easy to find their physical counterparts.

2.1.2 Smeared Crack Models

The second category of the microscopic approach is so-called smeared crack model, and they commonly adopt the notion of “*plane of degradation*” on which the nonlinear behavior is locally estimated. On the reduced space of plane of degradation, the normal and shear stresses are estimated from simple, fundamental rules proposed, and then transformed into the counterparts in the global, three-dimensional space, normally through some integration process.

In terms of definition of the plane of degradation, three major trends can be distinguished: (1) fixed crack model, (2) rotating crack model, (3) microplane model. Figure 2.3(b) and (c) shows gradually increasing deviation between two directions of initial crack and current principal strains inside the cracked material. In the fixed crack model, the plane of degradation is intentionally kept identical to the initial crack direction whereas in the rotating crack model, it is constantly evolved (rotated) so as to retain coaxiality between the two directions. It is obvious that in reality the deviation between the two directions might become markedly large as shown in figure 2.3(c). For clear comparison, the microplane model is given in figure 2.3(d), accompanied by a multitude of the plane of degradations at highly microscopic length scale.

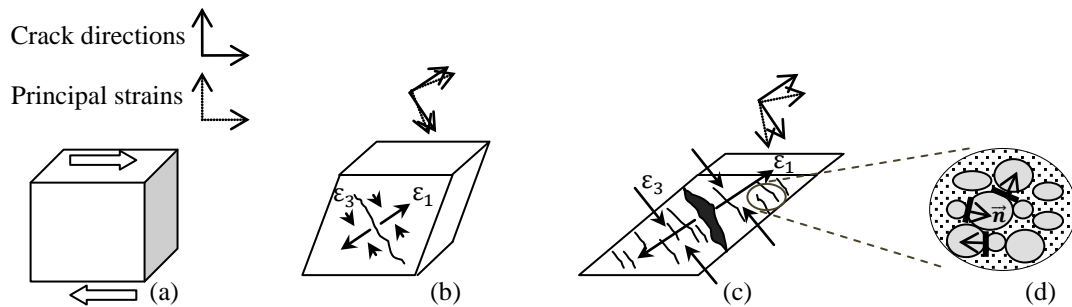


Figure 2.3. Increasing deviation of crack surface direction from that of current principal strains: (a) representative volume of quasi-brittle material under shear; (b) after the onset of tensile crack, the compressive principal strain $\epsilon_3 \approx 0$ and direction of crack surface is almost coincident with that of principal strains; (c) under excessive shear, considerable difference between the two directions develops; (d) schematic illustration of microplanes at microscopic length scale for comparison.

First, the fixed-type smeared crack model has the cardinal advantage of retaining the physical attribute of crack in such a way that the primary crack surface remains unchanged under subsequent loadings. On this account, fixed crack model shows good performance in predicting failure of quasi-brittle material, provided it is mainly governed by Mode-I crack. Many variants, after Rashid (1968), stem from this physically sound crack model to tackle various problems—e.g., nonorthogonal multiple crack model (de Borst and Nauta 1985) and adaptive fixed crack model (Weihe et al. 1998). Aiming at two-dimensional debonding problem found in composite

materials, for instance, Weihe et al. (1994) exploited the fixed crack model without secondary cracks in an attempt to describe the mixed mode failure. In their work, evolution of the strength-based fracture criterion is controlled by the dissipated energies, produced by Mode-I and Mode-II failure independently.

The downside of fixed crack model, however, is also well known. In the method, considerable strain change, which is induced by nonproportional loading, tends to result in spurious stresses parallel to the primary crack surface, eventually leading to unacceptable stress state even far larger than the material strengths. This deleterious attribute, therefore, gave rise to various supplementary alternatives. Adaptive fixed crack model by Weihe et al. (1998), for instance, was an attempt to unify fixed crack model and rotating crack model encompassing a wide range of materials from brittle to moderately ductile. On the framework of fixed crack model, additional multiple cracks are allowed to take place in order to accurately consider progressive degradation after onset of the primary crack. Regarding the threshold angle between the primary and secondary cracks, analytic criteria have been suggested by de Borst and Nauta (1985). Although such remedies of additional cracks remarkably improved the accuracy of fixed crack model, there still remain difficulties in defining the threshold angles, since the overall prediction is significantly affected by the artificially introduced angles.

Second, contrary to fixed crack model, the idea of rotating crack has played an important role in enhancing accuracy of analysis of degradation in structures made of quasi-brittle materials (Cope et al. 1980; Rots 1988; Jirásek and Zimmermann 1998). Since the rotated crack direction always coincides with that of principal strain (leaving only normal terms), it becomes more efficient to describe the nonlinearity in context of anisotropic material.

At the same time, many researchers actively detected and solved pathological attributes of rotating crack model—e.g., spurious stress transfer over large crack opening and mesh-induced directional bias. Among such strategies, a representative one is so-called “*nonlocal formulation*” (well summarized by Bažant and Jirásek 2002). With the aid of such elegant improvements, modified rotating crack model had been proved successful in studying fracture mechanism of quasi-brittle materials. In terms of stress invariant as the major ingredient of the criteria, rotating crack model holds considerable analogy (in some sense competing) with the classical plasticity model (Crisfield 1997). In particular, Weihe et al. (1998) showed that as ductility of material increases, the superiority of rotating crack model over fixed crack model becomes greater. When RC structures exhibit moderate ductility, mainly resulting from the reinforcing steel, rotating crack model is believed to provide better capability for failure prediction of RC structures than fixed crack model.

It should be stressed, however, that the rotating crack model essentially tends to lose the physical characteristics of actual cracks by employing the notion of “*rotation*” of crack. In fact, in a great number of experiments of RC structures, which undergo severe nonlinear damage due to cyclic loading, the “*rotating*” phenomenon of cracks is rarely observed. In other words, the

rotating crack model is rooted in the artificial concept of “*coaxiality*,” which precludes the method from incorporating further physical mechanisms to deal with complicated nonlinear behavior of real-world structures.

Third, in the microplane model (Bažant 1984; Carol and Prat 1990), the planes of degradation are considerably many and micro-scale, compared to other smeared crack models. Microplane model and its numerous variants are regarded to be powerful for capturing realistic fracture behavior of quasi-brittle material, and its universal applicability enables it to straddle a wide range of materials. Shortcoming of the microplane model, however, is that there intrinsically exists loss of physical counterparts of the decisive parameters for particular quasi-brittle materials such as concrete. And the existence of dependence on number of sampling points had been shown (Weihe et al. 1998), which means it always requires expensive computational cost.

2.1.3 Particle-Lattice Models

The last category of the representative microscopic analysis methodologies is so-called particle and lattice models, which are considered to be the most physics-rooted approach. In the method, all the nonlinear behavior of material is fundamentally regarded as the interaction among the particle constituents. For two-dimensional (2D) domain, some made attempts to describe the macroscopic nonlinear behavior mainly by means of contact between particles or inter-particle structures such as truss and frames at microscopic level. Since early attempts (Kawai 1980; Cundall and Strack 1979), there has been persistent improvement. For instance, in the work of van Mier et al. (2002), the 2D lattice beam model is utilized to study phenomena related to uniaxial tensile fracture, and the disorder of material is realized by probabilistic scattering of strength and stiffness with Weibull/Gaussian distribution. For 3d domain, Cusatis et al. (2003a, b) remarkably sophisticated the previous lattice models (Jirásek and Bažant 1995a,b; van Mier et al. 2002) by incorporating lateral confinement dependence, shear behavior with friction and cohesion effect, and lattice struts which transmit both axial force and shear force. Also, 3d lattice beam model has been developed for investigating fracture mechanism in relatively larger scale (Man and van Mier 2008).

Due to their novelty and abundance of physical counterparts, the particle and lattice approaches are regarded to be promising methods with broad spectrum, covering tensile fracture, localization, fragmentation, etc. And they also appear to be efficient tools for elucidating relationship between micro- and macrocharacteristics of quasi-brittle heterogeneous materials. Recently, such an action of bridging different scales gradually forms mainstream by virtue of multiscale analysis techniques (e.g., Miehe et al. 2010).

The limitations of this physics-rooted approach, however, pose a significant challenge. Generally, it calls for the essential prerequisite for the main analysis—the expensive probabilistic modeling with particles (or nodes), which makes the approach restricted to small laboratory scale specimens. Also, there might be some ambiguity in the cardinal mechanisms behind the microparticle interaction since we always have to, to some extent, assume what's actually happening inside the quasi-brittle materials. Furthermore, applying this approach to complex loading cases, in which damage is mainly tied with substantially fluctuating shear loads (e.g., inverted cyclic and seismic loading), is generally intractable.

2.2 Outline of Physics-Based Degrading Material Model

On the basis of the review addressed so far, the goal of present work is to integrate the key advantages of the various microscopic analysis methodologies in such a way that physical attributes are uncompromised and melted well into the formulation in as much detail as possible. First, in hopes of exploiting its universality and practical applicability, continuum approach is adopted as the main framework, which would serve as a powerful platform for detailed modeling of arbitrary three-dimensional structures made of quasi-brittle material and intricate reinforcing materials.

Next, in order to fully retain the physical nature of crack, “*fixed-type*” multidirectional smeared crack model, which can allow three orthogonal crack surfaces, is being exploited with the least need of introducing ambiguous parameters. Aforementioned shortcoming of the fixed crack model, i.e., spurious large stress transfer under nonproportional loading, has been overcome by 3d interlocking model proposed herein. Providing accurately degraded shear stiffness, the 3d interlocking model is following the central notion of tribology. Whereas the traditional particle and lattice models mainly deal with the particle-particle interaction by use of a sort of link or contact, the present interlocking model is focusing on the particle-matrix interaction in the light of the actual crack surfaces. It is noteworthy, however, that some effort has been made to retain the key advantage of the particle and lattice model: consideration of the realistic microstructure of the heterogeneous material. It is included in the present work in a way that the ideal particles, ranging actual aggregate sizes, are probabilistically generated from the Gaussian distribution and then randomly scattered, notably over entire domain.

In the fixed-type smeared crack context, the microscopic stress function is responsible for updating normal stress on the crack surfaces, whereas shear stress on the crack surfaces is separately generated from the 3d interlocking model. This independent microscopic stresses update gave rise to the hybrid domain concept—homogeneous domain for normal stress and heterogeneous domain with random particles for shear stress on the crack surfaces. Whereby, there exists weak correlation between normal and shear microscopic stresses update, which would be inconsistent with realistic material behavior. To fill the gap between those stress components on the crack surfaces, mainly by a physically reasonable manner, we suggested the consumed energy-based damage model, which we are concerned with in section 2.4.

In the light of these attractive features, the integrated material model suggested herein is believed to be a highly balanced microscopic approach, encompassing the continuum approach, the smeared crack model, and the particle-lattice models. Such favorable characteristics of physics-rooted approach, of course, were made accessible by virtue of cutting-edge parallel computing technology. Regarding the parallel platform of the present program, one is referred to chapter 3, which is mainly dealing with parallelization strategies.

2.3 Revisit to “Fixed-Type” Multidirectional Smeared Crack Model

The multidirectional and orthogonal smeared crack model adopted herein is based on the total strain rather than the decomposed strain which is common in plasticity theory. Since the multidirectional crack model constantly retains the nature of actual crack throughout the analysis, the anisotropy of the quasi-brittle material is readily taken into account. For comparable approaches one is referred to various works in literature, e.g., Vecchio and Collins (1986), and Selby and Vecchio (1993, 1997); the clear contrast to their works lies in the scale of the present orthogonal crack, which is assumed to be far smaller than that used in practical smeared crack models. Indeed, it is by “*averaged*” crack normally accompanied by coarse mesh that they explain the overall nonlinearity of reinforced structures, while present crack is designed to correspond to actually visible crack on the damaged structure. Further sophistication has been made for even invisible crack size (microcracks) by others. For instance, at highly microscopic length scale such total strain-based methods have been actively proposed and utilized by such researchers as Bažant and Gambarova (1984), Bažant et al. (1994).

2.3.1 Hybrid Domain Concept

The heart of multidirectional smeared crack model is the introduction of a number of planes of degradation, which is denoted as crack surfaces hereafter, consisting of three orthogonal surfaces. It is on the crack surfaces that the update of current normal and shear stresses is carried out. In the present study, a hybrid domain concept (illustrated in figure 2.4) is employed for separate evaluation of normal and shear stresses on the crack surfaces, which can be understood as a balanced approach between fully heterogeneous domain concept in lattice-particle models and homogenized domain concept in standard continuum models.

On one hand, for the normal stress on the crack surfaces which is essentially tied to the normal strain on the crack surface, we regard the domain as homogeneous, and any point within the domain is assumed to share the identical material properties involving decisive parameters for Mode-I tensile cracking and nonlinear compressive behavior. By this homogeneity assumption, normal stress update from the unified microscopic stress function in accordance with current normal strain on the crack surfaces becomes straightforward. Details as to the microscopic stress function proposed shall be given in section 2.3.3.

On the other hand, for the shear stress on the crack surfaces, the domain is treated as heterogeneous and impregnated with random particles to feed realistic asperity configuration of possible rough crack surfaces to the 3d interlocking mechanism. In conjunction with “*fixed-type*”

smear crack framework where the no rotation of opened Mode-I crack is allowed, the 3d interlocking mechanism would be primarily responsible for updating current shear stress on the crack surfaces. As will be dealt with in detail, such preserved information as to Mode-I crack opening plays an essential role in introducing tribology-inspired 3d interlocking mechanism.

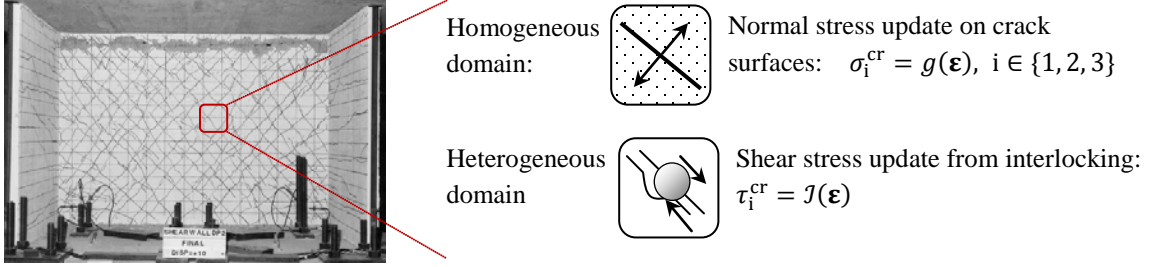


Figure 2.4. Hybrid domain concept for microscopic stress evaluation on the crack surfaces: (Right top) Homogeneous domain for normal stresses and (Right bottom) heterogeneous domain impregnated with random particles for 3d interlocking to update shear stresses (Left: real-scale RC structure damaged by cyclic loading, from Palermo and Vecchio 2002).

2.3.2 Strains on the Crack Surfaces and Criterion for Mode-I Cracking

At every loading step, the total strain is transformed into its counterpart on crack surfaces, ϵ^{cr} as

$$\epsilon^{cr} = \mathbf{P} \mathbf{T} \epsilon, \quad (2.2)$$

$$\epsilon^{cr} \equiv \begin{Bmatrix} \epsilon_n^{cr} \\ \gamma_s^{cr} \end{Bmatrix} \text{ with } \epsilon_n^{cr} \equiv \begin{Bmatrix} \epsilon_1^{cr} \\ \epsilon_2^{cr} \\ \epsilon_3^{cr} \end{Bmatrix} \text{ and } \gamma_s^{cr} \equiv \begin{Bmatrix} \gamma_1^{cr} \\ \gamma_2^{cr} \\ \gamma_3^{cr} \end{Bmatrix}, \quad (2.3)$$

with ϵ = current total strain tensor, \mathbf{T} = transformation matrix from eigen analysis of ϵ , and \mathbf{P} is for Poisson effect for which full description shall be given in section 2.5. Unlike strength-based formulation, the present total strain-based smeared crack model detects the onset of Mode-I tensile crack on the basis of current principal strain. Once the maximum principal strain exceeds the given strain threshold ϵ_{th} , we assume that physical Mode-I crack initiates, and thereafter \mathbf{T} is fixed:

$$\max(\text{eig}(\epsilon(\tau))) > \epsilon_{th} \rightarrow \mathbf{T}(t) = \mathbf{T}(\tau) \text{ for } \forall t \geq \tau. \quad (2.4)$$

In a similar fashion, possibly two more Mode-I cracks can take place

$$\varepsilon_i^{\text{cr}}(t) > \varepsilon_{\text{th}} \text{ for } \forall t \geq \tau, i \in \{1,2\} \quad (2.5)$$

with $\varepsilon_1^{\text{cr}} < \varepsilon_2^{\text{cr}} < \varepsilon_3^{\text{cr}}$, $\varepsilon_k^{\text{cr}} \in \text{diag}(\boldsymbol{\varepsilon}^{\text{cr}})$.

2.3.3 Stress Update on the Crack Surfaces

Local stress $\boldsymbol{\sigma}^{\text{cr}}$ defined on the crack surfaces is divided into normal stress $\boldsymbol{\sigma}_n^{\text{cr}}$ and shear stress $\boldsymbol{\tau}_s^{\text{cr}}$ for which distinct microscopic stress update procedures are suggested:

$$\begin{aligned} \boldsymbol{\sigma}^{\text{cr}} &\equiv \begin{Bmatrix} \boldsymbol{\sigma}_n^{\text{cr}} \\ \boldsymbol{\tau}_s^{\text{cr}} \end{Bmatrix}, \\ \boldsymbol{\sigma}_n^{\text{cr}} &\equiv \begin{Bmatrix} \sigma_1^{\text{cr}} \\ \sigma_2^{\text{cr}} \\ \sigma_3^{\text{cr}} \end{Bmatrix} = \begin{Bmatrix} g(\varepsilon_1^{\text{cr}}, d, d_{ic}) \\ g(\varepsilon_2^{\text{cr}}, d, d_{ic}) \\ g(\varepsilon_3^{\text{cr}}, d, d_{ic}) \end{Bmatrix}, \\ \boldsymbol{\tau}_s^{\text{cr}} &\equiv \begin{Bmatrix} \tau_1^{\text{cr}} \\ \tau_2^{\text{cr}} \\ \tau_3^{\text{cr}} \end{Bmatrix} = \begin{Bmatrix} \mathcal{J}(\boldsymbol{\varepsilon}^{\text{cr}}, d, d_{ic}) \\ \mathcal{J}(\boldsymbol{\varepsilon}^{\text{cr}}, d, d_{ic}) \\ \mathcal{J}(\boldsymbol{\varepsilon}^{\text{cr}}, d, d_{ic}) \end{Bmatrix}, \end{aligned} \quad (2.6)$$

where g is a microscopic normal stress update function; d is the consumed energy-based damage variable; d_{ic} is an internal variable accounting for initial lateral confinement.

It is noteworthy that each normal stress is exclusively related to the associated normal strain on the crack surface. Hence, the orthotropic nature of the cracked material in three dimension is readily taken into account. We shall provide detailed formulation for damage factor d in the later chapter, as well as the degree of lateral confinement d_{ic} . \mathcal{J} represents the microscopic shear stress update function by the 3d interlocking mechanism proposed herein to account for nonlinear shear stress on the crack surface.

It should be noted that in the present formulation each normal stress is directly correlated only to the associated normal strain on the crack surface—for instance, σ_2^{cr} is updated by stress update function g with respect to $\varepsilon_2^{\text{cr}}$. In this context, the influence of shear strain on the normal stress is neglected on the crack surfaces. Contrarily, shear stress on the crack surface is explicitly tied to the normal strain on the crack surface as reflected from the fact that the shear stress update function, \mathcal{J} takes the whole crack strain tensor $\boldsymbol{\varepsilon}^{\text{cr}}$ rather than a single strain term. Hence, current

formulation of multidirectional smeared crack model can be characterized by one-directional normal-shear coupling, i.e., only the influence of normal strain on shear stress is weakly active.

It is of importance to note, however, that in the present formulation, all terms of crack stresses are implicitly correlated each other through the consumed energy-based damage variable d , since all the crack strain terms are coherently used for estimating current consumed energy of the damaged material at each time step.

Rather than proposing a completely new model for describing microscopic tensile/compressive behavior, which would naturally necessitate laborious, systematic validations against a multitude of experiments, we tried to integrate the advantageous attributes of the previous accomplishments, departing from well-established tension/compression models for quasi-brittle materials.

We acknowledge that the existing tension/compression models are less likely to hold general applicability due to essentially different boundary condition, loading condition, and most important, possible inclusion of composite materials. Indeed, the “*plane of degradation*,” denoted as crack surface herein, is a sort of reduced space on which more simplicity holds compared to the original higher space, e.g., three 2D planes substitute the original 3d space in the present work. On the plane of degradation, it is assumed that uniaxial stress condition is locally met, and that normal stress on the crack surfaces can be obtained from the microscopic stress function, which had proven reliable from a multitude of experiments subject to uniaxial loading. Such simple and efficient normal stress update procedures at a reduced space, in particular for dealing with extreme cyclic loading, are the key advantage of most of the smeared crack models. Contrariwise, elasto-plasticity approach inevitably calls for highly complicated mathematical procedure to take into account cyclic loading conditions such as multiple yielding functions; comparable works for soil can be found in Hicher et al. (2008) and for ductile material in Steglich et al. (2005).

In the presence of considerable hydraulic pressure or lateral confinement, however, the use of such uniaxial hysteresis models might not be justifiable any longer, and it would require a special remedy such as expansion of compressive curve and increasing strength according to lateral constraint conditions. As a possible remedy to such conditions, the lateral confinement condition shall be handled by introducing the internal variable d_{ic} , which accounts for the degree of initial lateral confinement in a physically clear manner. Thus, detailed development as to d_{ic} shall be implemented in the future work.

2.3.3.1 Microscopic Tension Model

Amongst many tensile models, we adopted the model by Moelands and Reinhardt (Reinhardt 1984), which incorporates both linear softening and nonlinear softening behavior in a simple manner. We can rewrite this nonlinear softening model in terms of total strain in eq. (2.7). As easily seen in figure 2.5, the parameter $c = 1.0$ leads to the linear softening model, and otherwise it would correspond to nonlinear softening. In the all numerical simulations herein, the nonlinear softening rule was set by $c = 0.31$. This value is recommended by the reference (Reinhardt 1984), indeed it performs reasonably in all the simulations presented herein.

$$\sigma_i^{cr} = \begin{cases} \frac{f_t}{\varepsilon_t} \varepsilon_i^{cr} & \text{for } 0 < \varepsilon_i^{cr} \leq \varepsilon_t \\ f_t \left[1 - \left(\frac{\varepsilon_i^{cr} - \varepsilon_t}{\varepsilon_u - \varepsilon_t} \right)^c \right] & \text{for } \varepsilon_t < \varepsilon_i^{cr} \leq \varepsilon_u \\ \approx 0 & \text{for } \varepsilon_i^{cr} > \varepsilon_u \end{cases} \quad (2.7)$$

where ε_i^{cr} is the normal strain on i_{th} crack surface, $i \in \{1,2,3\}$; f_t and ε_t are the tensile strength and the corresponding strain, respectively; ε_u is the ultimate tensile strain retaining resistance; $c \in [0.31, 0.1]$ is the softening parameter.

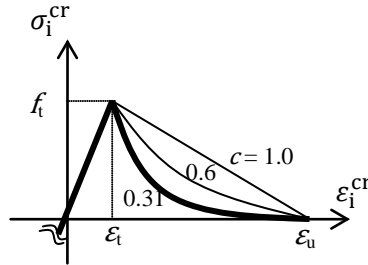


Figure 2.5. Nonlinear tension softening model.

It is of interest to investigate the relationship between the work done by the tensile crack opening and Mode-I fracture energy G_f^I . Let $W_t(\varepsilon)$ be the work done by the tensile opening, which can be calculated by integrating eq. (2.7) up to the present strain ε , and then we can easily confirm that it tends to approach a certain maximum limit. For instance figure 2.6 shows evolution of W_t with some test values (i.e., $f_t = 5$ MPa, $\varepsilon_t = 0.1667e-3$, $\varepsilon_u = 0.02$), and when $c = 0.31$, $W_t(\varepsilon_u) \rightarrow (0.2633 \varepsilon_t + 0.2366 \varepsilon_u) f_t$. In fact, this converged value is relatively very small compared to the total consumed energy pertaining to all possible microcracks in random directions, which are physically tied to the lateral expansion under compression.

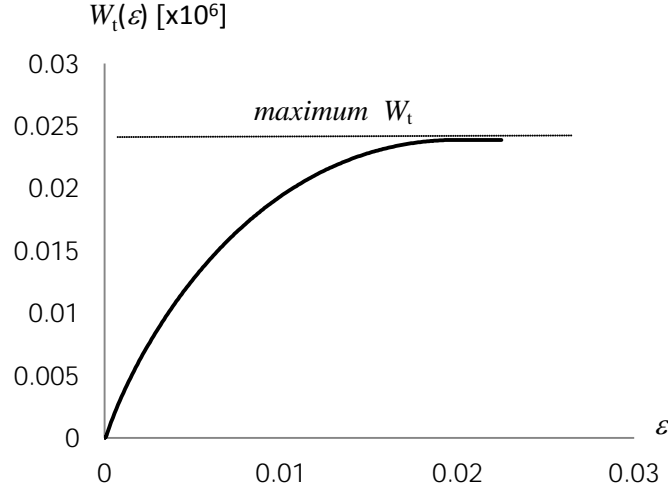


Figure 2.6. Work done by Mode-I cracking opening with nonlinear softening.

With the same sample values, we can further derive the relationship between the ultimate tensile strain ε_u and the Mode-I fracture energy, G_f^I (normally regarded as material constant). It is of practical importance to have this relationship between such a material-dependent property and decisive parameters used in microscopic stress update function. Adopting the notation of “*crack band width*” h (e.g., Bažant and Oh 1983), within which the damage is assumed to be concentrated, we can easily obtain

$$W_t(\varepsilon_u) - W_t(\varepsilon_t) = f_t \left[(\varepsilon_u - \varepsilon_t) - \frac{(\varepsilon_u - \varepsilon_t)}{1.31} \right] = \frac{G_f^I}{h}, \quad (2.8)$$

$$\therefore \varepsilon_u = 0.237 \left(\frac{G_f^I}{f_t h} + 0.237 \varepsilon_t \right), \quad (2.9)$$

where G_f^I is Mode-I fracture energy in $[\frac{J}{m^2}]$ and h is crack band width in $[m]$.

Thus, from eq. (2.9), the ultimate tensile strain ε_u retaining resistance can be systematically defined in terms of the material constants—fracture energy and the crack band width.

2.3.3.2 Microscopic Compression Model

As a base model for compressive behavior on the crack surfaces, the Thorenfeldt (1987) concrete model had been adopted among the various compressive base curves, and the expression of the model is given in eq. (2.10). This choice has been made for the reason that the model is believed to be one of the most balanced models with sufficient accuracy and efficiency for concrete, covering a wide range of strengths.

$$\sigma_i^{cr} = -f_c' \cdot x \left(\frac{n}{n-1 + x^{n-k}} \right), \quad (2.10)$$

where σ_i^{cr} = current normal stress on i th crack surface [MPa], $i \in \{1, 2, 3\}$,

f_c' = compressive strength [MPa],

$$x = \frac{\varepsilon_i^{cr}}{\varepsilon_0},$$

ε_i^{cr} = normal strain on i th crack surface, $i \in \{1, 2, 3\}$,

ε_0 = strain at the compressive strength,

$$n = 0.80 + f_c'/17,$$

$$k = \begin{cases} 1 & \text{for } 0 > \varepsilon_i^{cr} > \varepsilon_0, \\ 0.67 + f_c'/62 & \text{for } \varepsilon_i^{cr} < \varepsilon_0. \end{cases}$$

By differentiation, we can obtain initial slope as given in eq. (2.11), and it is used for all initial stiffness for all numerical simulation herein.

$$\left. \frac{\partial \sigma_i^{cr}}{\partial \varepsilon_i^{cr}} \right|_{\varepsilon_i^{cr}=0} = -\frac{f_c'}{\varepsilon_0} \left[\frac{n}{n-1} \right] \quad (2.11)$$

During the severe cyclic loading, concrete material undergoes complicated damage responses. Karsan and Jirsa (1969) proposed a quadratic formula of un/reloading paths in terms of normalized compressive strain, in which the unloading takes place along a straight line connecting two points, ε_r and ε_p :

$$\frac{\varepsilon_p}{\varepsilon_0} = 0.145 \left(\frac{\varepsilon_r}{\varepsilon_0} \right)^2 + 0.13 \left(\frac{\varepsilon_r}{\varepsilon_0} \right) \quad \text{for } \varepsilon_r > 2\varepsilon_0, \quad (2.12)$$

with ε_p = end point of unloading path on the strain axis, ε_r = strain from which unloading starts, ε_0 = strain at the compressive strength.

To include reasonable behavior under high compressive strain region, Taucer et al. (1991) adopted the above model for compressive strain less than $2\varepsilon_0$ and suggested a model for the compressive strain larger than $2\varepsilon_0$ as

$$\frac{\varepsilon_p}{\varepsilon_0} = 0.707 \left(\frac{\varepsilon_r}{\varepsilon_0} - 2 \right) + 0.834 \quad \text{for } \varepsilon_r \leq 2\varepsilon_0, \quad (2.13)$$

Although a multitude of nonlinear un/reloading models have been proposed since then, this simplified linear path unloading model is believed to serve as a balanced model without loss of accuracy and efficiency. Figure 2.7(left) shows the adopted un/reloading model embedded into the Thorenfeldt concrete model. Reloading is assumed to take place along the unloading path until current strain reaches ε_r . As seen in figure 2.7(right), the compressive response exhibits drastic changes in shapes according to the varying compressive strengths. The initial stiffness becomes larger with increasing strength, and higher strength makes the curve sharper, likely causing more brittle compression failure.

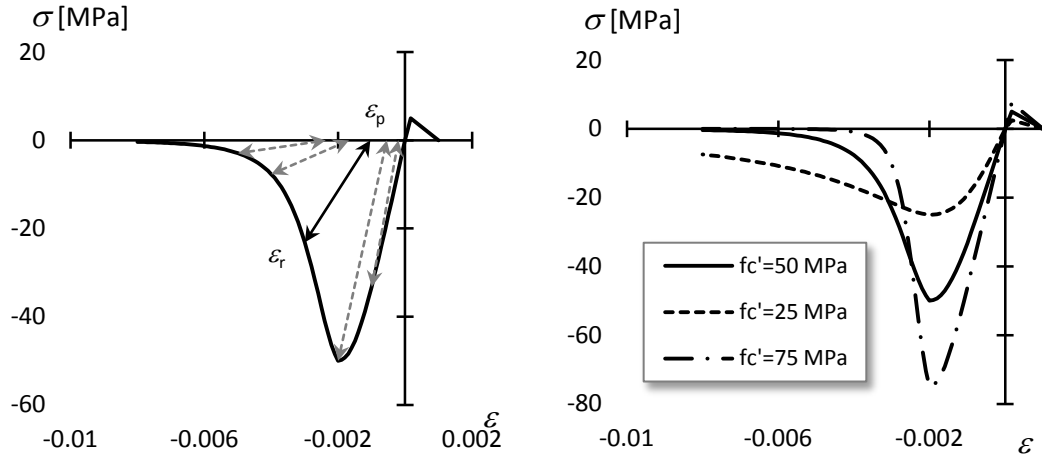


Figure 2.7. Microscopic stress function based on Thorenfeldt compression model augmented by tension regime and un/reloading paths (Left); sensitivity of curve shape to strengths (Right).

Tension resistance of concrete appeared to be dependent on the previous compressive damage. Since current un/reloading model includes residual strain ε_p , ensuing tensile resistance is assumed to take effect from that strain point ε_p . Also, excessive compressive damage previously happened leads to total loss of tensile strength, which is plausible in a physical sense. Therefore, tensile strength is assumed to disappear once compressive strain exceeds the strain at peak compressive strength (ε_0). Early development of tensile resistance during the unloading process

by tensile loading and total loss of tensile resistance due to excessive compressive damage are shown in figure 2.8.

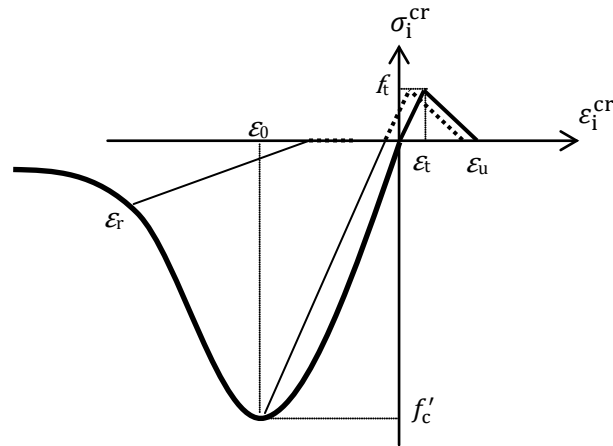


Figure 2.8. Tensile resistance development depending on previous compressive damage.

2.4 Damage Models

Continuum damage theories have received a great deal of attention, because they can describe “*damage*” of material in a physically appealing manner. Damage is characterized by a number of microscopic degradation mechanisms such as growth and coalescence of voids or development of microcracks during loading. On the variational approach and plasticity theory, a systematic formulation for damage has been derived from the thermodynamics of irreversible process and internal state variables (e.g., Simo and Ju 1987a, 1987b). Particularly for the localization phenomena, the damage model was enhanced such that the gradient term was incorporated on the nonlocal framework by Peerlings et al. (1996), from which an extension was undertaken by de Borst (2001) in order to embrace the advantageous features of plasticity theory.

2.4.1 Review of Damage Models

To grasp the central concepts of previous damage models, a brief review of some damage theories shall be given, and then a consumed energy-based damage model being proposed herein will be addressed in what follows.

2.4.1.1 Elasticity-Based Gradient Damage Theory

The elasticity-based gradient damage theory by Peerlings et al. (1996) can be summarized by followings. The stress-strain relation is given,

$$\boldsymbol{\sigma} = (1 - \omega(\kappa^d)) \mathbf{D}^e \boldsymbol{\varepsilon}, \quad (2.14)$$

where $\boldsymbol{\sigma}$ = stress tensor, \mathbf{D}^e = Hookean stiffness matrix, $\boldsymbol{\varepsilon}$ = strain tensor, $\omega(\kappa^d)$ = scalar-valued damage variable ranging from 0 to 1 which stand for intact and fully damaged states, respectively, κ^d = scalar-valued history parameter depending on a loading function f^d , which takes the form as

$$f^d = \bar{\varepsilon} - \kappa^d, \quad (2.15)$$

where $\bar{\varepsilon}$ = nonstandard equivalent strain satisfying a partial differential equation (PDE), in a form of the Helmholtz-type equation as

$$\bar{\varepsilon} - g_d \nabla^2 \bar{\varepsilon} = \tilde{\varepsilon}. \quad (2.16)$$

In above, g_d is the gradient parameter which is defined as $\partial\sigma/\partial(\frac{\partial^2 \varepsilon^p}{\partial x^2})$ for instance in 1D case, and the local equivalent strain $\tilde{\varepsilon}$ is derived from the strain tensor $\boldsymbol{\varepsilon}$ as $\tilde{\varepsilon} = \tilde{\varepsilon}(\boldsymbol{\varepsilon})$.

As proposed by Peerlings et al. (1996), above Helmholtz-type relation between $\bar{\varepsilon}$ and $\tilde{\varepsilon}$ stems from the Taylor expansion of the local equivalent strain $\tilde{\varepsilon}(\mathbf{x} + \boldsymbol{\xi})$ which is primarily used in nonlocal theory, i.e., weighted averaging procedure to give the nonlocal equivalent strain $\bar{\varepsilon}(\mathbf{x})$:

$$\bar{\varepsilon}(\mathbf{x}) = \frac{1}{V} \int_V \gamma(\boldsymbol{\xi}) \tilde{\varepsilon}(\mathbf{x} + \boldsymbol{\xi}) dV, \quad \text{with} \quad \frac{1}{V} \int_V \gamma(\boldsymbol{\xi}) dV = 1, \quad (2.17)$$

where $\gamma(\boldsymbol{\xi})$ is a weigh function and $\boldsymbol{\xi}$ is a position vector from the material point at \mathbf{x} to the infinitesimal volume dV within the domain V of interest.

By the inclusion of second-order gradient term in the formulation of nonlocal independent variable, the damage process zone is effectively controlled in an elegant manner, mainly in terms of the so-called “*internal length*” which mathematically arises during the Taylor expansion. Furthermore, the size effect is well captured by the use of the internal length. Of course, this necessitates additional effort to determine a meaningful value for the internal length of quasi-brittle materials through “*fitting*” against experimental data—e.g., for RC structure by impact like loading (de Borst 2001); for glass-fiber-reinforced polypropylene by tension loading (Geers et al. 1999).

Apart from such a special treatment for the determination of internal length, however, one of the key shortcomings of this approach is that the additional PDE for $\bar{\varepsilon}$ in eq. (2.16) always calls for additional boundary condition, which usually resorts to a premise with little physical interpretation, although sophisticated recommendations were suggested by such researchers as Lasry and Belytschko (1988), Mühlhaus and Aifantis (1991).

2.4.1.2 Gradient Plasticity Theory

In plasticity, the strain rate is generally decomposed into two parts as

$$\dot{\boldsymbol{\varepsilon}} = \dot{\boldsymbol{\varepsilon}}^e + \dot{\boldsymbol{\varepsilon}}^p, \quad (2.18)$$

where elastic strain rate relates to the stress rate $\dot{\boldsymbol{\sigma}} = \mathbf{D}^e \dot{\boldsymbol{\varepsilon}}^e$, and the plastic strain rate normally results from a plastic potential function Φ and the equivalent plastic strain rate $\dot{\varepsilon}^p$ such that

$$\dot{\boldsymbol{\varepsilon}}^p = \dot{\varepsilon}^p \frac{\partial \Phi}{\partial \boldsymbol{\sigma}}.$$

In this theory, the plastic loading function is defined by

$$f^p = \tilde{\sigma}(\boldsymbol{\sigma}) - \bar{\kappa}(\nabla^2 \varepsilon^p). \quad (2.19)$$

The consistency condition $\dot{f}^p = 0$ yields a Helmholtz equation for the plastic strain rate,

$$\dot{\varepsilon}^p + \frac{g_d}{h} \nabla^2 \dot{\varepsilon}^p = -\frac{1}{h} \frac{\partial \tilde{\sigma}}{\partial \boldsymbol{\sigma}} : \dot{\boldsymbol{\sigma}}, \quad (2.20)$$

where the hardening modulus is written by $h = -\frac{\partial \bar{\kappa}}{\partial \varepsilon^p}$ followed by the gradient constant $g_d = -\frac{\partial \bar{\kappa}}{\partial \nabla^2 \varepsilon^p}$. It should be stressed that the above equation holds only in the plastic region whereas the counterpart of elasticity-based gradient damage theory can apply to entire domain. Although there exist some practical remedies to this restriction, (e.g., de Borst and Pamin 1996), for the better alternative, de Borst (2001) suggested the gradient plastic-damage model as will be outlined in the following section.

2.4.1.3 Gradient Plastic-Damage Model

In order to integrate the attractive gradient damage model and the plasticity formalism for explanation of plastified material parts, possibly found in intact material between microcracks or voids, de Borst (2001) modified the elasticity-based gradient damage model to incorporate plastic strain as

$$\boldsymbol{\sigma} = (1 - \omega) \mathbf{D}^e (\boldsymbol{\varepsilon} - \boldsymbol{\varepsilon}^p). \quad (2.21)$$

The plastic strain rate still obeys plastic potential function Φ as $\dot{\boldsymbol{\varepsilon}}^p = \dot{\varepsilon}^p \frac{\partial \Phi}{\partial \boldsymbol{\sigma}}$ with equivalent plastic strain rate $\dot{\varepsilon}^p$, and the plastic loading function controls the emergence of them as

$$f^p = \tilde{\sigma}(\hat{\boldsymbol{\sigma}}) - \bar{\kappa}(\varepsilon^p), \quad (2.22)$$

where the resulting consistency relation from $\dot{f}^p = 0$ yields with hardening modulus $h = -\frac{\partial \bar{\kappa}}{\partial \varepsilon^p}$:

$$\dot{\varepsilon}^p = -\frac{1}{h} \frac{\partial \tilde{\sigma}}{\partial \hat{\boldsymbol{\sigma}}} : \dot{\hat{\boldsymbol{\sigma}}}, \quad (2.23)$$

and the effective stress is now defined as a function of stress tensor and damage:

$$\hat{\sigma} = \frac{\sigma}{1-\omega(\bar{\kappa})}. \quad (2.24)$$

2.4.2 Consumed Energy-Based Damage Model

Starting from the valuable knowledge of previous damage models summarized so far, we propose a novel damage model which is fundamentally based on the consumed energy of the material. The estimation of the consumed energy is conducted in the reduced space defined by the crack surfaces, i.e., effectively on the present multidirectional smeared crack model framework. The damage information attained from the framework, in turn, affects other physical mechanisms such as 3d interlocking model, which are also incorporated in the multidirectional smeared crack model framework.

Notably, the consumed energy is assumed to be directly related to the disintegration process of the material, which is most likely caused by excessive compression, cyclic, or seismic loading. In this context, the energy dissipated solely by the Mode-I tensile cracking is intentionally excluded for the estimation of the consumed energy used in the new damage model. Physically, this separation of consumed energy stems not only from the fact that the energy dissipated by Mode-I cracking is always bounded by the upper limit (as numerically shown in section 2.3.3), but also from the fact that the upper limit is relatively small compared to the total cohesive energy of the material.

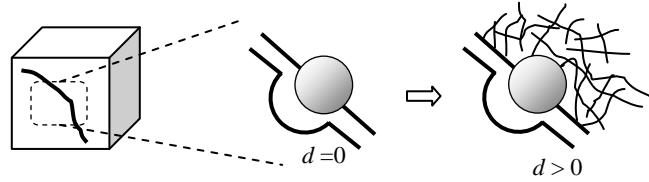


Figure 2.9. Progressive damage in matrix in vicinity of ideal sphere.

As illustrated in figure 2.9, the damage in matrix in vicinity of ideal sphere can accumulate with excessive loading, essentially weakening shear stress transfer across open crack surfaces.

Many isotropic damage models assume that the damage factor reduces all stress terms, generally in a simple form of $\boldsymbol{\sigma} = (1 - d)\mathbf{D}_e\boldsymbol{\varepsilon}$ with \mathbf{D}_e elastic material stiffness matrix. Contrariwise, in the present formulation only the shear resistance, which is defined on the crack surfaces by means of the 3d interlocking mechanism, is exclusively reduced by the damage factor as illustrated by eq. (2.25).

$$\tilde{\boldsymbol{\sigma}}^{\text{cr}} \equiv \begin{bmatrix} 1 & & & & \\ & 1 & & & \\ & & 1 & & \\ & & & (1-d) & \\ & & & & (1-d) \\ & & & & & (1-d) \end{bmatrix} \boldsymbol{\sigma}^{\text{cr}}, \quad (2.25)$$

with $\boldsymbol{\sigma}^{\text{cr}}$ is local stress on the crack surfaces whereas $\tilde{\boldsymbol{\sigma}}^{\text{cr}}$ stands for that after consideration of the consumed energy-based damage model.

The underlying reason for this selective reduction of stress is twofold—firstly, in the present smeared crack formalism, the microscopic compression model defined on crack surfaces already provides “*softened*” normal stress in accordance with the current compressive strain beyond the peak point. Secondly, it is rooted in the physical observation that the damage, induced by the compressive deformation, always brings about the disintegration of matrix, and consumes the cohesive energy between material ingredients, e.g., particles and surrounding matrix in concrete. Indeed, it is physically reasonable to look on the disintegration of matrix induced by compressive deformation as the primary “*cause*” of damage, not as “*result*” of damage.

In this context, the damage factor d being proposed is primarily governed by the microscopic compression function g defined on the crack surfaces. Also, it depends on the minimum elastic strain energy density W_{\min} , which is defined as the energy obtained by integrating the ideal linear stress functions up to $\varepsilon_{\min}^{(i)}$ (the minimum compressive strains ever experienced in i_{th} crack direction). Thus, the novel damage factor d is proposed as

$$d \equiv \frac{W_{\min} - \sum_{i=1}^3 \int_0^{\varepsilon_{\min}^{(i)}} g(\varepsilon_i^{\text{cr}}) d\varepsilon_i^{\text{cr}}}{W_{\min}}, \quad (2.26)$$

$$\varepsilon_{\min}^{(i)}(t) = \min_{\tau \leq t} \varepsilon_i^{\text{cr}}(\tau), \quad (2.27)$$

$$W_{\min} = \sum_{i=1}^3 \frac{1}{2} \frac{\partial g}{\partial \varepsilon_i^{\text{cr}}} \Big|_{\varepsilon_i^{\text{cr}}=0} \times \varepsilon_{\min}^{(i)2}. \quad (2.28)$$

As shown in figure 2.10, the damage factor d can be envisaged by the area ratio of the region between two stress lines to the triangular region. It should be noted that the area between two stress lines, i.e., straight line and the compression curve denoted by g , always guarantees the essential characteristic of damage factor such that

$$\frac{\partial d}{\partial t} \geq 0 \text{ for } \forall t > 0, \text{ and } 0 \leq d \leq 1. \quad (2.29)$$

In fact, the common underlying notion of all the damage models is that the irreversible degradation of material can be traced by a scalar-valued damage factor d (or damage vector) ranging from 0 to 1, which indicate intact state and completely disintegrated material state, respectively.

Also, the unique advantage of the present definition of damage factor lies in the extensibility of the damage model for the lateral confinement/hydraulic pressure dependence. They can be effectively taken into account by simply enlarging the stress function g in an appropriate way. It shall correspond to larger compressive strength and smoother postpeak stress path as depicted in figure 2.10.

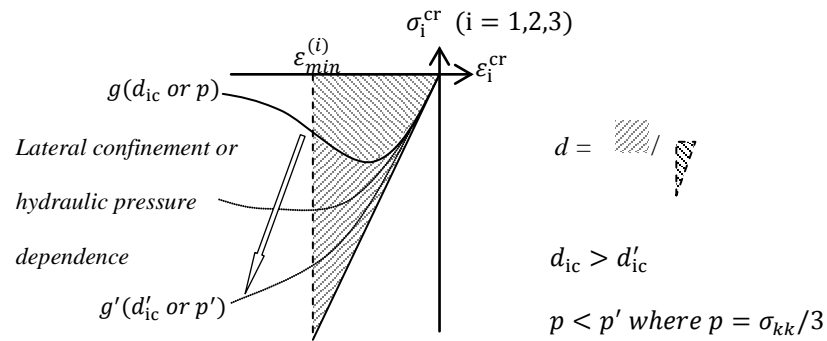


Figure 2.10. Interpretation of damage factor d as an area ratio, and possible inclusion of the lateral confinement/hydraulic pressure dependence by the expansion of stress function g . $d_{ic} (\geq 0)$ stands for the degree of the initial lateral confinement.

2.5 Poisson Effect and Transformation to Crack Coordinates

When composite materials undergo compressive deformation state, laterally placed stiff material can cause confinement condition due to the Poisson effect, e.g., concrete surrounded by lateral steels. Such a lateral confinement considerably affects compressive response of quasi-brittle material in a passive manner; the notation of “*passive*” is used to distinguish it from hydraulic pressure-induced lateral confinement, which is denoted as “*active*.” Being “*passive*” lateral confinement signifies that the origin of the confinement (e.g., lateral steel bars in RC structures) does not provide additional external loading to the structure, but rather serves as a constraint to deformation in the lateral directions. Thus, the Poisson effect dominates the induced stress in the lateral direction, normal to the principal loading direction. Contrarily, “*active*” lateral confinement (e.g., by hydraulic pressure) means that the ingredient of lateral constraint actively provides external forces to the structure. Hence, the combination of the Poisson effect and multi-axial, external pressures governs the induced stress in the lateral direction.

In the present study, we restrict our attention to such a “*passive*” lateral confinement condition where the Poisson effect is predominant. This limitation is justifiable in broad practical situations in earthquake engineering involving normal RC infrastructures exposed cyclic/seismic loading, which we are mainly concerned with herein. Naturally, the inclusion of “*active*” condition shall be a future extension for more generality.

Another concern of some interest is the “*uniformity*” of the lateral confinement. Particularly, under the hydraulic pressure, the material is most likely to experience the uniform multi-axial stress condition, throughout the volume under pressure, whereas laterally deployed reinforcing components cannot fully reproduce such a perfectly uniform multi-axial stress condition on the volume. Of course, highly dense lateral reinforcements or some plate form composites which is fully encapsulating the brittle part in the core can be regarded to mimic such a uniform, multi-axial stress conditions on the volume. In the present work, we adopted the premise of “*uniform*” realization of lateral confinement, on which we proceed with our formulation. However, this assumption should be appropriately resolved in the future research, and the nonlocal formulation of the Poisson effect would be a successful remedy, since the influence of reinforcing steel bars is physically effective over some bounded region, markedly decaying with the distance from the bars. Indeed, such a concept of decaying effect over the volume and appropriate volume averaging is the central notion of “*nonlocal*” formulation. Therefore, reasonable consideration of lateral confinement in conjunction with nonlocal formulation should be a next essential extension of the present study.

For describing the Poisson effect in three-dimensional structures, many approaches have been suggested, e.g., “*prestrain*” concept proposed by Selby and Vecchio (1993, 1997) in which fictitious lateral force is introduced for the Poisson effect in a three-dimensional element. In the

present work, “*equivalent strain*” method by Feenstra et al. (1998) has been employed due to its efficiency and clarity.

To elucidate the key concept, it is worth revisiting fundamental idea of the equivalent strain method, and an illustrative example is given. We can first rearrange the stress-strain relation for the linear elastic three-dimensional case, with normal terms only, as

$$\begin{Bmatrix} \sigma_1 \\ \sigma_2 \\ \sigma_3 \end{Bmatrix} = \frac{1}{(1+\nu)(1-2\nu)} \begin{bmatrix} E & 0 & 0 \\ 0 & E & 0 \\ 0 & 0 & E \end{bmatrix} \begin{bmatrix} 1-\nu & \nu & \nu \\ \nu & 1-\nu & \nu \\ \nu & \nu & 1-\nu \end{bmatrix} \begin{Bmatrix} \varepsilon_1 \\ \varepsilon_2 \\ \varepsilon_3 \end{Bmatrix}. \quad (2.30)$$

By introducing equivalent strain, denoted $\{\varepsilon\}^*$ below, from multiplication with the matrix of Poisson ratio, we obtain

$$\begin{Bmatrix} \sigma_1 \\ \sigma_2 \\ \sigma_3 \end{Bmatrix} = \begin{bmatrix} E & 0 & 0 \\ 0 & E & 0 \\ 0 & 0 & E \end{bmatrix} \begin{Bmatrix} \varepsilon_1 \\ \varepsilon_2 \\ \varepsilon_3 \end{Bmatrix}^*. \quad (2.31)$$

As can be seen in eq. (2.31), each normal stress can be directly calculated from the corresponding equivalent strain term, which provides a sort of orthogonal situation. Thus, we can systematically construct the procedures for strain transformation into crack direction followed by the Poisson effect consideration as

$$\boldsymbol{\varepsilon}^{\text{cr}} = \mathbf{P} \mathbf{T} \boldsymbol{\varepsilon}, \quad (2.32)$$

where the Poisson ratio matrix $\mathbf{P} \in \mathbb{R}^{6 \times 6}$ is defined by

$$\mathbf{P} \equiv \begin{bmatrix} \frac{1-\nu}{(1+\nu)(1-2\nu)} & \frac{\nu}{(1+\nu)(1-2\nu)} & \frac{\nu}{(1+\nu)(1-2\nu)} & 0 \\ \frac{\nu}{(1+\nu)(1-2\nu)} & \frac{1-\nu}{(1+\nu)(1-2\nu)} & \frac{\nu}{(1+\nu)(1-2\nu)} & 0 \\ \frac{\nu}{(1+\nu)(1-2\nu)} & \frac{\nu}{(1+\nu)(1-2\nu)} & \frac{1-\nu}{(1+\nu)(1-2\nu)} & 0 \\ 0 & 0 & 0 & \mathbf{I} \end{bmatrix}, \quad (2.33)$$

and the typical transformation matrix $\mathbf{T} \in \mathbb{R}^{6 \times 6}$, which is obtained from the eigen analysis of current strain $\boldsymbol{\varepsilon}$, is in the form of

$$\mathbf{T} = \begin{bmatrix} \mathbf{T}_{11} & \mathbf{T}_{12} \\ \mathbf{T}_{21} & \mathbf{T}_{22} \end{bmatrix}, \quad (2.34)$$

$$\mathbf{T}_{11} = \begin{bmatrix} \cos^2 \theta_{x1} & \cos^2 \theta_{y1} & \cos^2 \theta_{z1} \\ \cos^2 \theta_{x2} & \cos^2 \theta_{y2} & \cos^2 \theta_{z2} \\ \cos^2 \theta_{x3} & \cos^2 \theta_{y3} & \cos^2 \theta_{z3} \end{bmatrix}, \quad (2.35)$$

$$\mathbf{T}_{12} = \begin{bmatrix} \cos \theta_{x1} \cos \theta_{y1} & \cos \theta_{y1} \cos \theta_{z1} & \cos \theta_{x1} \cos \theta_{z1} \\ \cos \theta_{x2} \cos \theta_{y2} & \cos \theta_{y2} \cos \theta_{z2} & \cos \theta_{x2} \cos \theta_{z2} \\ \cos \theta_{x3} \cos \theta_{y3} & \cos \theta_{y3} \cos \theta_{z3} & \cos \theta_{x3} \cos \theta_{z3} \end{bmatrix}, \quad (2.36)$$

$$\mathbf{T}_{21} = 2 \begin{bmatrix} \cos \theta_{x1} \cos \theta_{x2} & \cos \theta_{y1} \cos \theta_{y2} & \cos \theta_{z1} \cos \theta_{z2} \\ \cos \theta_{x2} \cos \theta_{x3} & \cos \theta_{y2} \cos \theta_{y3} & \cos \theta_{z2} \cos \theta_{z3} \\ \cos \theta_{x3} \cos \theta_{x1} & \cos \theta_{y3} \cos \theta_{y1} & \cos \theta_{z3} \cos \theta_{z1} \end{bmatrix}, \quad (2.37)$$

$$\mathbf{T}_{22} = \begin{bmatrix} c \theta_{x1} c \theta_{y2} + c \theta_{y1} c \theta_{x2} & c \theta_{y1} c \theta_{z2} + c \theta_{z1} c \theta_{y2} & c \theta_{z1} c \theta_{x2} + c \theta_{x1} c \theta_{z2} \\ c \theta_{x2} c \theta_{y3} + c \theta_{y2} c \theta_{x3} & c \theta_{y2} c \theta_{z3} + c \theta_{z2} c \theta_{y3} & c \theta_{z2} c \theta_{x3} + c \theta_{x2} c \theta_{z3} \\ c \theta_{x3} c \theta_{y1} + c \theta_{y3} c \theta_{x1} & c \theta_{y3} c \theta_{z1} + c \theta_{z3} c \theta_{y1} & c \theta_{z3} c \theta_{x1} + c \theta_{x3} c \theta_{z1} \end{bmatrix}, \quad (2.38)$$

with $c \theta_{y1} = \cos \theta_{y1}$ (with θ_{y2} representing the angle between global y-axis and 2nd principal direction).

Then, in the aforementioned microscopic stress update procedure, the total strain $\boldsymbol{\epsilon}^{\text{cr}}$ on the crack surfaces is used as the key to describing all the nonlinear degradation on three orthogonal crack surfaces. The updated stress $\boldsymbol{\sigma}^{\text{cr}}$ on the crack surfaces will then be transformed back into the global stress $\boldsymbol{\sigma}$ by following the well known virtual strain energy density concept:

$$\boldsymbol{\sigma} = \mathbf{T} \boldsymbol{\sigma}^{\text{cr}}. \quad (2.39)$$

As an illustrative example, consider a unit cubic element laterally confined by horizontal steels to understand the flow as to the Poisson effect consideration addressed so far. Suppose a concrete element with $\nu = 0.15$ is uniaxially compressed and the transversal reinforcing steels has material properties as $E_{\text{steel}} = 200 \text{ GPa}$, $\sigma_y = 50 \text{ MPa}$, $A = 0.01 \text{ m}^2$.

Current strain is given by $\boldsymbol{\epsilon} = \{5.045 \times 10^{-5}, 5.045 \times 10^{-5}, -4.0 \times 10^{-4}, 0, 0, 0\}^T$.

Then from eq. (2.32), we obtain

$$\boldsymbol{\epsilon}^{\text{cr}} = \{-1.185 \times 10^{-5}, -1.185 \times 10^{-5}, -4.035 \times 10^{-4}, 0, 0, 0\}^T.$$

As described in figure 2.11, after the nonlinear analysis, we can obtain current concrete stress, which is in equilibrium with lateral forces induced by transverse steels, as

$$\boldsymbol{\sigma} = \{-4.043 \times 10^5, -4.043 \times 10^5, -1.375 \times 10^7, 0, 0, 0\}^T$$

Note that the transformation by \mathbf{T} changes only the sequence of strain in ascending order and leaves the values unchanged.

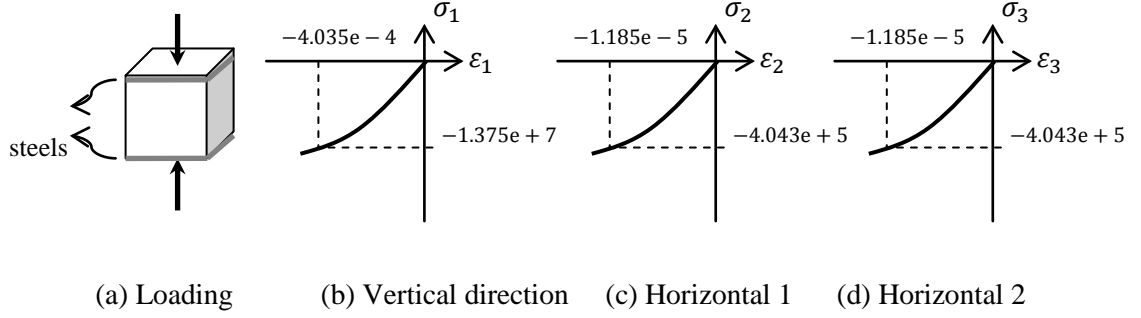


Figure 2.11 Example of stress update with Poisson effect consideration

We can also obtain the steel stress, which remains in the elastic range: $\sigma_{\text{steel}} = 1.01075 \times 10^7$ with $\epsilon_{\text{steel}} = 5.045 \times 10^{-5}$. From the force comparison in horizontal directions, we can confirm that the equilibrium is exactly met; force by steel is $4 \times (\sigma_{\text{steel}} A) = 4.043 \times 10^5$ and force by concrete is -4.043×10^5 where the area of concrete is 1.0 for the unit cube. Further illustrative examples with different lateral confinement conditions are provided in appendix A.

2.6 3d Interlocking Model for Nonlinear Shear

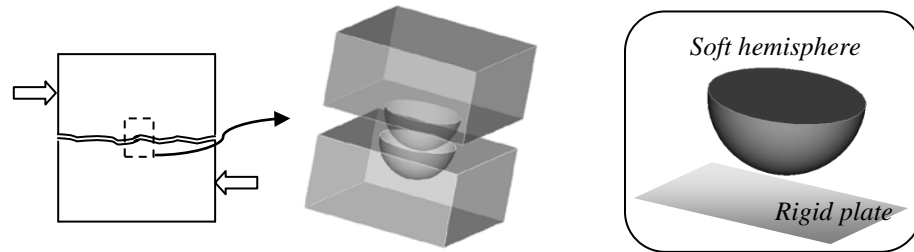


Figure 2.12. The base couple of rigid particle-soft matrix for 3d interlocking model being proposed herein (Left); Typical asperity model in tribology for comparison (Right).

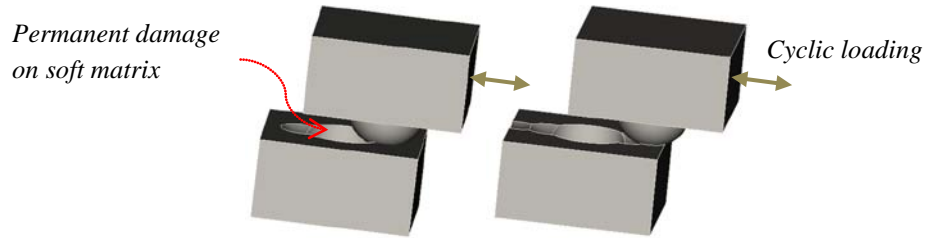


Figure 2.13. Permanent plastic damage to the soft matrix by cyclic movement.

The underpinning of Walraven's 2D interlocking model (1994) is that the stress transfer over opened crack directly depends on contacting areas between 2D semicircle and its indentation, and that a probabilistic method is used for the distributing of actual aggregate sizes. The major advantage of the 2D interlocking model is not only that a physically appealing mechanism generates the nonlinear stress, but also that a probability theory offers the access to the realistic asperity configuration of the rough crack surfaces.

Departing from this physically and probabilistically attractive 2D interlocking model, we have derived a 3d interlocking model, which serves as a decisive mechanism in describing the degradation of tangent shear stiffness at cracked phase. Once Mode-I crack opens, shear transfer is determined by the ideal particle-indentation couple. Figure 2.12(left) shows the base couple of rigid particle-soft matrix while figure 2.12(right) for reference depicts a typical asperity model consisting of rigid plate and soft hemisphere widely used in tribology (after Greenwood and Williamson 1966). The single asperity model in tribology assumes that the plastic deformation happens on the hemisphere part due to severe contact with rigid flat plate (e.g., Jackson and Green 2005). Conversely, in the present work, it is assumed that the permanent plastic

deformation occurs at soft matrix part only, and the ideal sphere remains intact during the whole cyclic loading process (see figure 2.13).

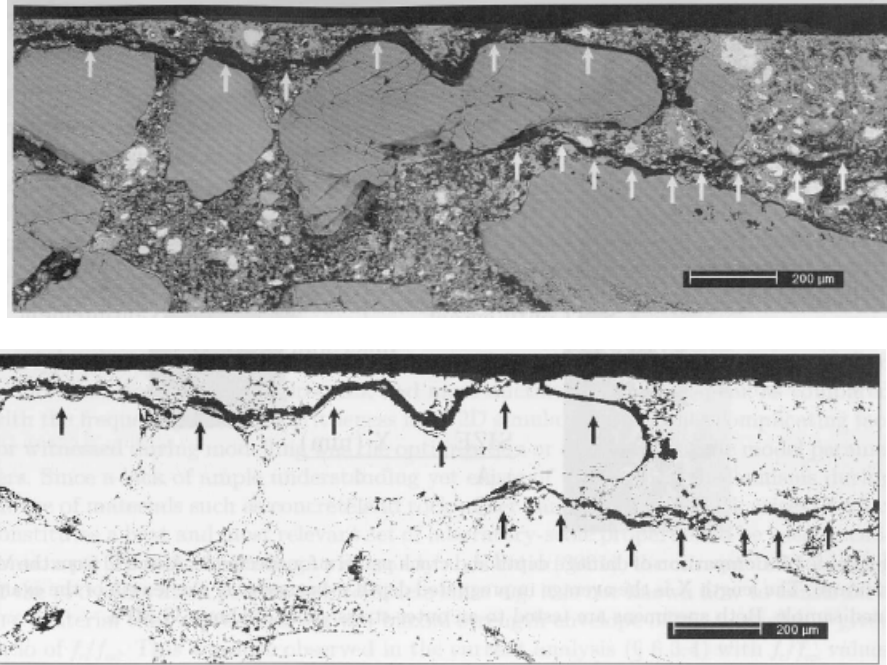


Figure 2.14. Micrographs revealing micro-cracking along the aggregate boundaries of a concrete specimen: (Top) Actual cross section of concrete specimen showing crack patterns emphasized by arrows; (Bottom) Clearly visible cracks after image processing (from Elkadi 2005).

This assumption adopted herein is strongly tied to the physical nature of microcracking in actual concrete. As shown in figure 2.14, under excessive loading the micro-cracking tends to develop in the weak matrix first, and to grow along the boundaries of relatively stiff aggregates. Such irregular, zigzagged configurations of opened crack surfaces can be realistically described by a large number of the fabrics of rigid sphere-soft indentation.

In the light of the physics-rooted reasoning addressed so far, we rigorously obtained nonlinear shear resistance as shall be given in what follows. Let us assume that one ideal particle of diameter D_{\max} causes shear resistance. If it is displaced by d relative gap distance between crack surfaces, we can obtain the horizontal and vertical projections of contact area of the moving sphere in terms of d (see shaded area in figure 2.15).

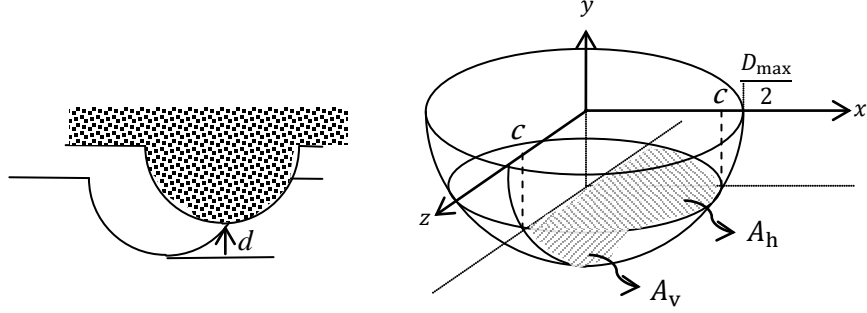


Figure 2.15. Projections of contacting area of the ideal hemisphere with diameter D_{\max} .

With $c = \sqrt{\left(\frac{D_{\max}}{2}\right)^2 - d^2}$ as depicted in figure 2.15 and the formula of $\int \sqrt{a^2 - z^2} dz = \frac{1}{2} (z\sqrt{a^2 - z^2} + a^2 \arctan(\frac{z}{\sqrt{a^2 - z^2}}))$, we obtain the projected areas of hemisphere as

$$A_h = \frac{\pi c^2}{2}, \quad (2.40)$$

$$A_v = 2 \int_0^c \sqrt{\left(\frac{D_{\max}}{2}\right)^2 - z^2} - d \, dz, \quad (2.41)$$

$$\therefore A_v = \left(\frac{D_{\max}}{2}\right)^2 \arctan\left(\frac{c}{d}\right) - c \times d. \quad (2.42)$$

Again, it should be stressed that on the present multidirectional smeared crack model, notably being “fixed-type,” the actual crack directions are realistically retained, and thus it is reasonable to regard shear transfer to be directly pertaining to the interlocking mechanism over an open crack. Therefore, the tangent shear stiffness can be thought to be directly affected by contacting areas. In this context, we obtain the tangent shear stiffness in terms of relative distance d and areas:

$$G \propto [A_v + \mu A_h], \quad (2.43)$$

$$\begin{aligned} \therefore G \propto & \left[\left(\frac{D_{\max}}{2}\right)^2 \arctan \sqrt{\left(\frac{D_{\max}}{2d}\right)^2 - 1} - d \sqrt{\left(\frac{D_{\max}}{2}\right)^2 - d^2} \right. \\ & \left. + \frac{\pi}{2} \mu \left(\left(\frac{D_{\max}}{2}\right)^2 - d^2\right)\right]. \end{aligned} \quad (2.44)$$

For a concise form, introducing $\tilde{\varepsilon} = \frac{2d}{D_{\max}}$ and normalization with $\left(\frac{D_{\max}}{2}\right)^{-2}$ yield

$$G \propto \left[\arctan \sqrt{(\tilde{\varepsilon})^{-2} - 1} - \tilde{\varepsilon} \sqrt{1 - \tilde{\varepsilon}^2} + \frac{\pi}{2} \mu (1 - \tilde{\varepsilon}^2) \right]. \quad (2.45)$$

It is natural to expect considerable difference in strength between the ideal particle and the soft matrix, which can be envisaged as the strength difference between aggregates and cement paste for an instance of concrete. Hence, appropriate reduction is taken into account by use of a reduction factor, denoted C_{cs} herein. Although C_{cs} has physical meaning of strength difference of the key constituents, determining a proper value is not tractable. So, it has been chosen from interlocking test (Fig. 2.20), giving $C_{cs} = 1.66e - 4$, and this value was used in all numerical simulations presented here. Finally, the tangent shear stiffness on crack surface is proposed as

$$G(\tilde{\varepsilon}) = C_{cs} \frac{G_0}{(1 + \mu)} \frac{2}{\pi} \left[\arctan \sqrt{(\tilde{\varepsilon})^{-2} - 1} - \tilde{\varepsilon} \sqrt{1 - \tilde{\varepsilon}^2} + \frac{\pi}{2} \mu (1 - \tilde{\varepsilon}^2) \right], \quad (2.46)$$

where G_0 = elastic shear modulus; μ = friction coefficient, 0.4 is used throughout the simulations; $\tilde{\varepsilon} = \frac{2d}{D_{\max}}$; C_{cs} is the reduction factor according to the strength difference between particle and matrix (attained as $1.66e - 4$).

We can see the relationship between $\tilde{\varepsilon}$ and ε in one-dimensional case given by

$$\varepsilon = \frac{d}{L} = \frac{d}{D_{\max}/2} \frac{D_{\max}/2}{L} = \tilde{\varepsilon} \frac{D_{\max}/2}{L}, \quad (2.47)$$

$$\therefore \tilde{\varepsilon} = \frac{L}{D_{\max}/2} \times \varepsilon. \quad (2.48)$$

where L = length of element and ε = normal strain to the crack surfaces.

As seen in figure 2.16, the tangent shear stiffness decreases with $\tilde{\varepsilon}$ (or equivalently with d) such that $G|_{\tilde{\varepsilon}=0 \text{ or } d=0} = C_{cs} G_0$ and $G|_{\tilde{\varepsilon}=1 \text{ or } d=0.5D_{\max}} = 0.0$. To expand on the necessity of 3d interlocking model, in which 3d hemisphere rather than 2D semicircle has been adopted, the shear stiffness reduction obtained from 2D semicircle model (by Walraven 1994) is provided in figure 2.16(b). According to figure 2.16, it is apparent that 2D semicircle-based interlocking model would reproduce larger shear stiffness than 3d hemisphere case, which would render it less favorable for alleviating the problem of interest, i.e., over-stiff shear transfer across opened crack.

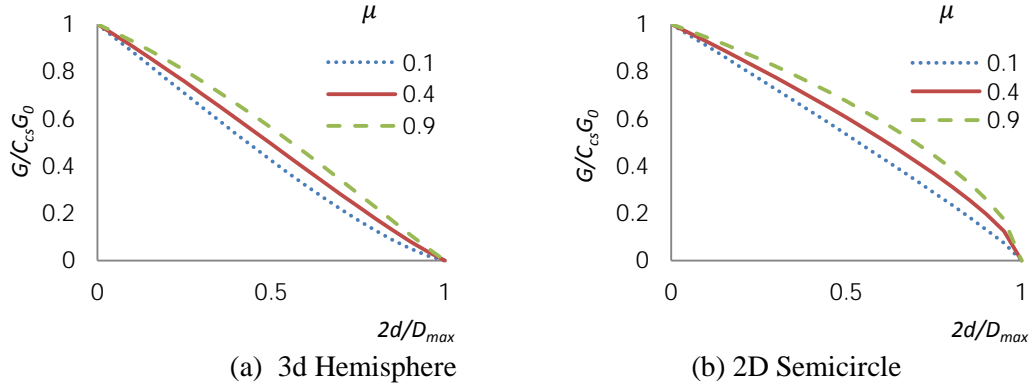


Figure 2.16. Degradation of tangent shear stiffness with several friction coefficients: (a) when 3d hemisphere is used; (b) 2D semicircle is adopted for interlocking mechanism, exhibiting relatively stiff nature than that with 3d hemisphere.

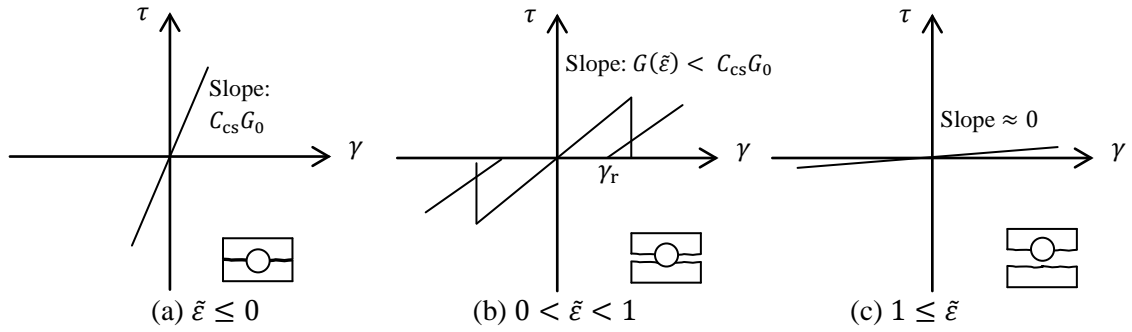


Figure 2.17. Variation of tangent shear stiffness depending on crack opening.

As shown in figure 2.17(a), when the crack is completely closed, the maximum tangent shear stiffness is regained according to the interlocking mechanism proposed. It is noteworthy that once tensile crack takes place, we always employ interlocking mechanism for evaluating nonlinear shear stiffness, which leads to the “weak” upper limit of tangent shear stiffness in the presence of Mode-I crack—cf. “strong” upper limit proposed by Regan (1971) in which full initial shear stiffness is ideally regained after complete closure of tensile crack. The choice of the weak upper limit has been made because such a strong upper limit can be realized only when a small number of discrete tensile cracks appear and then completely close in a well-controlled condition, which is generally far from the situation of structures of interest exposed to severe cyclic/seismic loading. In figure 2.17(c), we can see that if the crack fully opens, more than half of the ideal particle size, there remains no resistance to shear.

In the intermediate stage when the crack begins to reopen, as depicted in figure 2.17(b), the shear resistance between crack surfaces is governed by the interlocking mechanism described so far. No resistance is assumed during unloading process which is comparable with a sort of fully irrecoverable damaged state. During reloading process somewhat early resistance is gained as denoted by re-contacting shear strain γ_r in figure 2.17(b). This might result from the remaining debris of matrix, left by shearing off and grinding. However, this early resistance during reloading gradually disappears as the horizontal displacement increases, so an expression for γ_r has been suggested such that $\gamma_r \rightarrow \gamma_{\max}$ as $\gamma \gg 0$:

$$\begin{aligned}\gamma_r &= |\gamma_{\max}| \times \{a + b(1 - e^{(-c \times |\gamma_{\max}|)})\} \quad \text{for } \gamma > 0, \\ \gamma_r &= |\gamma_{\min}| \times \{a + b(1 - e^{(-c \times |\gamma_{\min}|)})\} \quad \text{for } \gamma < 0,\end{aligned}\tag{2.49}$$

where a, b , and c are positive constant with $a + b = 1$; γ_{\max} (γ_{\min}) maximum (minimum) shear strain ever experienced on the crack surfaces. Some recommended values, i.e., $a = 0.8$; $b = 0.2$; $c = 1.0$, have shown favorable performance throughout all simulations presented herein.

2.6.1 Random Particle Distribution

Walraven (1981) showed a probability density function considering a surface and actual aggregates, and applied it to the numerical simulation of the rough crack experiment, particularly by use of two-dimensional finite elements and semicircle-matrix interaction (Walraven 1994). The goal of the present work, however, is to describe the overall degradation of shear resistance of real-scale structures under cyclic/seismic loading, mainly by use of physically reliable interlocking mechanisms. Indeed, in such a realistic situation a large number of distributed cracks rather than a discrete crack are most likely to appear and on the account govern the nonlinear behavior. Along each of the distributed cracks, a large number of shear transfers over microscopic cracks play in concert to give resultant shear resistance. This fact led us to the attractive notion of tribology.

To describe asperity contact, Jackson and Green (2005) derived analytical expressions of contact area and force of a single asperity on the elasto-plastic framework. And then they generated random asperity heights from the uncompromised Gaussian distribution for the entire contact surface, and performed integration to draw resultant global force-slip relationship. In a similar fashion, some used the simplified exponential form of Gaussian distribution (Polycapou and Etsion 1999; Liu et al. 2000) for better asperity distribution. Since random scattering from Gaussian distribution appeared to reproduce sufficient accuracy in their studies, present platform has adopted the Gaussian distribution as the base probability distribution for generating particle sizes for the 3d interlocking model.

To clarify the distribution process of ideal particle, let \mathcal{D} be a homogeneous random field of ideal particle size for the interlocking mechanism in the physical domain Ω . In the present study, Ω represents the entire domain of structure on which nonlinear degradation is defined.

Here, it is instructive to review the key concept behind the random field theory. The random field \mathcal{D} can be completely defined by a correlation function ρ and a probability distribution function f , due to the assumed characteristic of homogeneity, which stands for the invariance of the statistical parameters of the field under translation on the domain. In structural mechanics, there are typically three types of correlation function $\rho(\mathbf{x}_1, \mathbf{x}_2)$ with l (so-called *correlation length*) for decay with increasing distance between two points:

$$\text{Triangular: } \max \left\{ 0, 1 - \frac{|\mathbf{x}_1 - \mathbf{x}_2|}{l} \right\}, \quad (2.50)$$

$$\text{Exponential: } \exp \left(-\frac{|\mathbf{x}_1 - \mathbf{x}_2|}{l} \right), \quad (2.51)$$

$$\text{Gaussian: } \exp\left(-\frac{|\mathbf{x}_1 - \mathbf{x}_2|^2}{l^2}\right). \quad (2.52)$$

According to an application of finite element reliability method to study of elasto-viscoplastic material's localized failure (Gutiérrez and de Borst 1999), the correlation length has important effect on the onset of localization modes—the probability of asymmetric failure modes is reversely proportional to the correlation length. Small correlation length essentially means sharper imperfections (or defects) distribution on the field, causing more likely asymmetric localization failure modes than symmetric modes (i.e., cross-diagonal shear bands).

Among a number of methods (see Li and der Kiureghian 1993), in the present study the midpoint methods has been adopted to discretize the random field \mathcal{D} into a vector of random variable $\mathbf{D} = \{D_1, D_2, \dots\}$ associated with a probability density function $f_{\mathbf{D}}$. Following the notion of the mid-point method as done by many (e.g., Carmeliet and de Borst 1995, Gutiérrez and de Borst 1999), a random variable D_i defined on a subdomain $\Omega_i \in \Omega$ can be represented by

$$D_i = \mathcal{D}(\mathbf{x}_i^c), \quad (2.53)$$

where \mathbf{x}_i^c is a vector representing the center of the subdomain Ω_i .

Furthermore, we assumed Ω_i to be equal to a finite element of the structure under consideration, as commonly done (e.g., Gutiérrez and de Borst 1999). In this context, each subdomain, i.e., a finite element, holds one ideal particle size which is generated from the Gaussian distribution.

Particularly, Carmeliet and de Borst (1995) performed a systematic study on stochastic nonlocal damage model in which heterogeneity of material property for localized failure and nonlocal formulation for mesh objectivity are harmoniously introduced. In line with nonstandard continuum via nonlocal formulation, they make the autocorrelation coefficient similar to nonlocal damage model as

$$\rho(\boldsymbol{\tau}) = e^{-(|\boldsymbol{\tau}|^2/\theta^2)}, \quad (2.54)$$

with $\boldsymbol{\tau}$ is the separation vector of two points \mathbf{x} and $\mathbf{x} + \boldsymbol{\tau}$ and θ is the correlation length.

Departing from this similarity of definition, they can compare the effect of two length parameters, namely “*internal length*” in nonlocal formulation and “*correlation length*” in random field theory. Their study showed that the internal length plays dominantly in terms of energy dissipation during fracture process and spreading-out of damage in the nonlocal damage model appears to be prevalent in the tensile loading tests.

It should be noted that the particle size is normally larger than a finite element size. After averaging through the standard finite element analysis procedure, the random particles over a large number of finite elements would mimic the irregular asperity heights. Therefore, the particle is not the realization of actual aggregate, for instance in the case of concrete material, but a sort of effective realization of rough crack surfaces which is still significantly dependent on the aggregate sizes.

2.6.2 Interlocking during Cyclic Movement

Physical interpretation of the interaction between the rigid particle and the soft matrix provides clear insight into realistic behavior of cyclic shear resistance of the 3d interlocking mechanism presented herein. Figure 2.18(a) shows that linear shear stress-strain increase with a slope $G(\tilde{\epsilon})$ which corresponds to the current crack opening. In this particular illustration, the gap remains fixed, and therefore the slope is estimated constant. When the loading is reversed, the permanently damaged soft matrix would leave no active contacting between the opened crack surfaces. Hence, little shear resistance is found in the range of $0 < \gamma < \gamma_{\max}$ as shown in figure 2.18(b).

In many experimental results, it is widely observed that re-contacting occurs before the horizontal displacement reaches the previous maximum point from which unloading took place. Such a re-contacting is represented in terms of re-contacting shear strain γ_r here as given in eq. (2.49). When the current strain lies between this re-contacting shear strain γ_r and the previous maximum strain γ_{\max} , as shown in figure 2.18(c), we can expect development of some shear resistance with reduced tangent shear stiffness $\alpha_1 G(\tilde{\epsilon})$ where $\alpha_1 \in (0, 1)$. As reloading further proceeds beyond γ_{\max} , it is assumed that full contacting has been now achieved, and afterward shear stress is regarded to obey interlocking mechanism as depicted in figure 2.18(d).

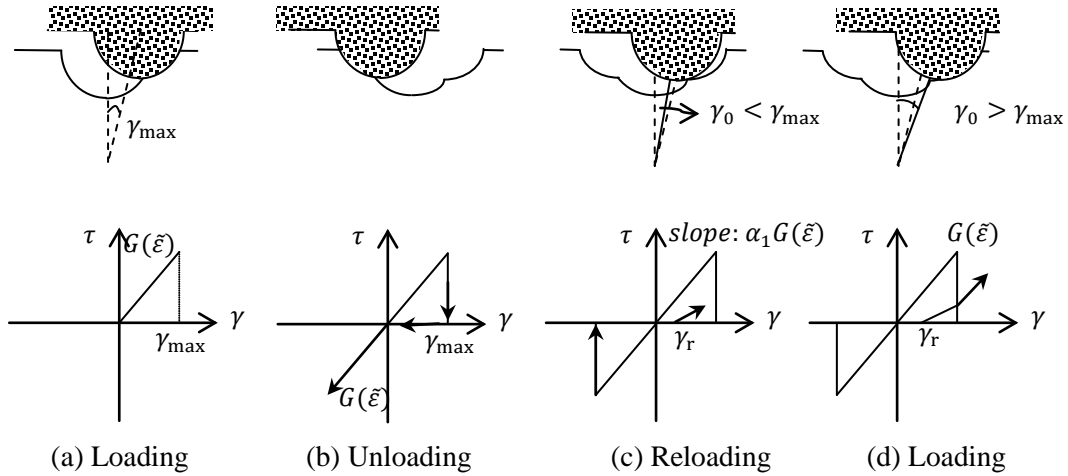


Figure 2.18. Interlocking states during cyclic loading (all shear strain and shear stress terms signify those on the crack surfaces).

On this physically apparent reasoning, we can construct tangent shear stiffness matrix \mathbf{G}^{cr} defined on crack surfaces. At each incremental step, new tangent shear stiffness G_{ij}^{cr} should be updated from the 3d interlocking model with current crack stains as

$$\mathbf{G}^{\text{cr}} \equiv \begin{bmatrix} \frac{\partial \tau_{12}^{\text{cr}}}{\partial \gamma_{12}^{\text{cr}}} & 0 & 0 \\ 0 & \frac{\partial \tau_{23}^{\text{cr}}}{\partial \gamma_{23}^{\text{cr}}} & 0 \\ 0 & 0 & \frac{\partial \tau_{13}^{\text{cr}}}{\partial \gamma_{13}^{\text{cr}}} \end{bmatrix} = \begin{bmatrix} G_{12}^{\text{cr}} & 0 & 0 \\ 0 & G_{23}^{\text{cr}} & 0 \\ 0 & 0 & G_{13}^{\text{cr}} \end{bmatrix}, \quad (2.55)$$

$$G_{ij}^{\text{cr}} \equiv \begin{cases} G_0 & \text{for } \varepsilon_i^{\text{cr}}, \varepsilon_j^{\text{cr}} \leq 0 \\ \alpha_1 G(\tilde{\varepsilon}) & \text{otherwise} \end{cases}, \quad (2.56)$$

with $\varepsilon_i^{\text{cr}}$ = normal crack strain in i_{th} normal direction to the crack surfaces, $i \in \{1,2,3\}$; $\tilde{\varepsilon} = \frac{2L}{D_{\text{max}}} \times \max(\varepsilon_i^{\text{cr}}, \varepsilon_j^{\text{cr}})$.

$$\alpha_1 \equiv \begin{cases} 1.0 & |\gamma| \geq |\gamma_{\text{max}}| \\ (0.0, 1.0) & |\gamma_r| \leq |\gamma| < |\gamma_{\text{max}}| \\ 0.0 & |\gamma| < |\gamma_r| \end{cases} \quad (2.57)$$

2.6.3 Validation against an Interlocking Experiment

The bottom line of the 3d interlocking model proposed is that the degradation of shear stiffness mainly results from the particle-matrix interaction, particularly in the presence of the opened Mode-I crack. In order to validate the interlocking model, a well-documented experiment of rough crack by Briseghella and Gori (1984) had been selected. In the experimental program, a plain concrete block of dimension $0.2 \times 0.2 \times 0.2$ m is initially separated into two parts leaving a discrete rough Mode-I crack with width 1 mm. Afterwards, the lower block is horizontally loaded in a reversed cyclic manner by displacement-control.

The nonlinear analysis performed consists of two stages: the first stage is for generating the initial Mode-I cracking in the middle layer, followed by the second stage for horizontal cyclic loadings. For the numerical simulation, the cracked blocks in figure 2.19(a) were modeled by three layers of finite elements in vertical direction (each layer consists of 2500 hexahedral elements). As shown in figure 2.19(b), the middle layer was intentionally designed to hold initial Mode-I cracking as well as ensuing interlocking behavior. The arrows depicted in figure 2.19(b) stand for the directions normal to the cracked surface. At the very first stage of the simulation, ideal particles were generated from Gaussian distribution and assigned to all elements on the middle layer, and the configuration of the random distribution across the middle layer is shown in figure 2.19(c) from which spatially unstructured nature of this distribution can be easily confirmed.

The goal of this research is to achieve realistic degradation of shear stiffness due to interlocking, so boundary condition are assigned such that the applied horizontal slips are totally absorbed by the middle layer, reproducing horizontal resisting force.

Overall, a set of physical processes is repeatedly happening with increasing horizontal loading in both experiment and numerical simulation: As the horizontal loading is applied, the contacting area between rigid sphere and soft matrix begins to generate shear resistance, and nonzero slope on the graph represents such an active contact. After reversal of the horizontal loading, unloading phase takes place with almost zero slope as shown in the graph, since the matrix has been permanently damaged by the precedent loading excursion, leaving no active contact to produce shear resistance. During the reversed loading excursion, however, if the horizontal slip reaches the previously maximum point, undamaged matrix starts to resist slip by re-contact with solid sphere.

Figure 2.20 shows the horizontal slip and resultant force responses from the experiment and prediction. For clarity, the unloading and reloading paths with zero slopes are not shown in the figure, and only ascending and descending paths with non-zero slopes are shown in figure 2.20(b). As easily seen, the overall nonlinear response of shear force transfer over the rough crack surfaces are successfully predicted by the interlocking model proposed. The predicted range of

the peak forces well agrees with the experimental results. Particularly, up to 0.6 mm of slip, very weak resistance is observed, and this might be due to the fact that initial gap between the particle and the indentation may exist. And such a partial contact at initial loading stages had been realized by reducing the contacting areas, only at the early stage of the interlocking simulation.

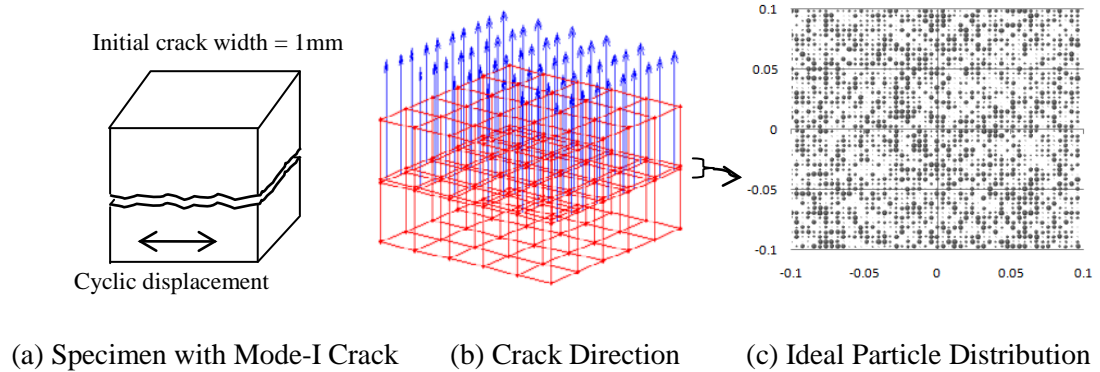


Figure 2.19. Validation setup of 3d interlocking model against experiment: (a) actual experimental specimen; (b) numerical modeling of specimen with initial Mode-I crack, marked by arrows in the middle layer [for visualization purpose, only 25 element blocks are shown]; (c) random particle distribution along the middle layer of 2500 elements.

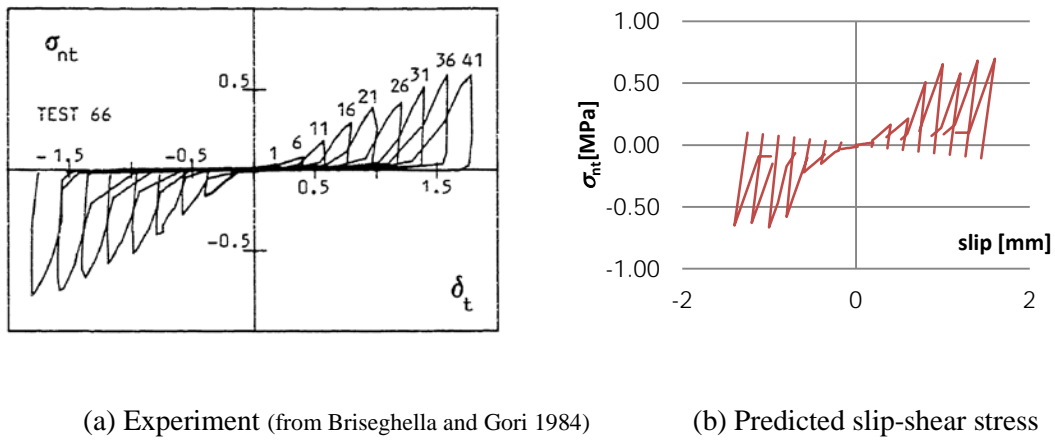


Figure 2.20. Horizontal slip-resultant force responses (force is represented by corresponding shear stress).

2.6.4 *Effect of Number of Elements and Mean Diameter of Particles*

Based on the well-received concept in tribology, the ideal particles are first probabilistically distributed over the entire domain, and from the midpoint method mentioned before every integration point of one element has been assigned with one identical particle size. Consequently, as the total number of elements increases through mesh refinement, the diversity of sizes and total number of particles also increases. One of the salient advantages of the present interlocking model is that we can enrich diversity of particle sizes without the explicit need of complicated re-modeling of entire particle or lattice system.

Specifically, the present interlocking mechanism imparts several favorable characteristics to the numerical update procedures: first, the instantaneous shear stress drawn from each particle-matrix interaction is independently estimated at every integration point level. Second, the element length L of each element is explicitly included in the formulation of interlocking model as reflected in eq. (2.46), and it can be automatically available on all elements. Third, the exact volume fraction of each element, via the common numerical integration procedure, allows the insensitivity of global shear force to the number of elements. It is of practical importance to note that all of those tasks are embarrassingly parallelizable by their nature. Indeed, all of the relevant tasks are well melted into the present parallel platform.

Figure 2.21 presents the parametric study on the element size, performed with two representative probability distributions having the same mean diameter 0.019 m: Normal distribution $\mathcal{N}(0.019, 0.00633^2)$ and uniform distribution $\mathcal{U}(0.0001, 0.038)$. The aforementioned rough crack experiment is numerically simulated with varying number of elements, $11^2 \sim 50^2$, and all other conditions are identical for both probability distributions. The vertical axis of figure 2.21 stands for the predicted maximum horizontal forces normalized by that of the simulation with 11^2 elements. According to figure 2.21, the insensitivity of resulting horizontal force to the number of elements is obvious, regardless of the type of probability distribution employed. This implies that mesh refinement appears to have little effect on the interlocking-induced shear force, of course given that the total cross-sectional shearing area is fixed.

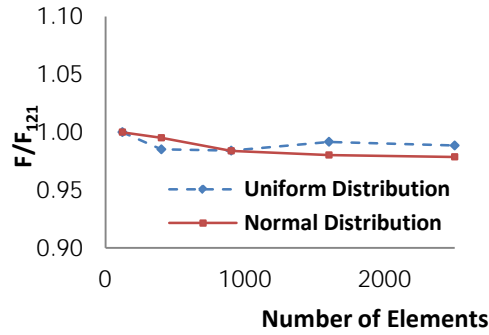


Figure 2.21. Normalized maximum horizontal forces with varying element numbers for two random particle distributions—Normal and Uniform distributions.

The mean value used in the probability distribution for random particle size, however, exhibits significant effect on the resultant horizontal forces. The contacting area for current tangent shear stiffness is obviously dependent on the particle size according to the formulation in eq. (2.46). This nonlinear dependence is clearly detected in the simulations by varying the mean value.

The uniform distribution has been temporarily adopted such that the mean value is controlled as needed and the range is fixed by [mean – 0.019 m, mean + 0.019 m]. Figure 2.22 gives the positive peak forces collected from the numerical simulations of the experiment with initial crack width of 1 mm. As expected, the increased mean size of particle distribution pushes upward the range of forces in a nonlinear manner. It should be noted that with a mean size larger than a certain value, e.g., 25 mm herein, the resulting horizontal forces appear to converge to the specific upper bound. This can be physically conceived by the situation in which sufficiently large-sized particles almost occupy their indentations.

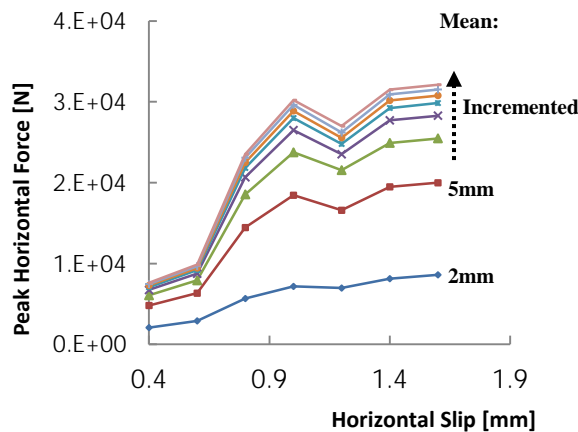


Figure 2.22. Effect of particle size on resultant horizontal force from 3d interlocking model.

2.7 “Smart” Reinforcing Steel Bar Model

2.7.1 Review of Previous Research

Kunnath et al. (2009) proposed a generic reinforcing ribbed steel model, primarily based on the existing phenomenological hysteresis models such as those by Menegotto and Pinto (1973) and Chang and Mander (1994), and they incorporated advanced concepts including the initiation of compressive buckling (along the line of Dhakal and Maekawa, 2002a), low-cycle fatigue fracture, and cyclic strength degradation.

In terms of postyield buckling, through comprehensive parametric study, Dhakal and Maekawa (2002a) suggested a simple buckling model which primarily requires only a few parameters—the yield strength f_y and slenderness ratio L/D as major factors, covering a wide range of strengths and hardening behaviors. They proposed an intermediate point $(\varepsilon^*, \sigma^*)$ at which substantial softening due to buckling takes place:

$$\frac{\varepsilon^*}{\varepsilon_y} = 55 - 2.3 \sqrt{\frac{f_y L}{100 D}}; \quad \frac{\varepsilon^*}{\varepsilon_y} \geq 7, \quad (2.58)$$

$$\frac{\sigma^*}{\sigma_1^*} = \alpha \left(1.1 - 0.016 \sqrt{\frac{f_y L}{100 D}} \right); \quad \sigma^* \geq 0.2 f_y, \quad (2.59)$$

where ε_y is the strain at the yield strength f_y [MPa]; L is bar length [m]; D is diameter of the cross section [m]; σ_1^* is the stress from the stress-strain relationship without consideration of buckling; α is the factor for linear hardening ($= 1.0$) and perfectly plastic ($= 0.75$). Once the current strain exceeds this intermediate point, the stress is suggested to decrease with the slope, 2% of initial stiffness until it reaches residual strength, 20% of yield strength, and thereafter stress is assumed to remain constant as illustrated in figure 2.23. The notable outcome of their study is that the initiation of buckling is dependent not only on L/D but also on the yield strength of the steel, as reflected in eq. (2.58) and eq. (2.59). It should be noted, however, that all their parametric studies are relying on some idealized premises: fixed ends boundary condition, monotonic axial loading, and a fiber section-utilizing FEA program with a predefined hysteretic steel model.

Dhakal and Maekawa (2002b) derived a simple method for estimating buckling length of longitudinal steels, with emphasis on RC column members. In their attempt, the horizontal reinforcing elements such as stirrups and ties were replaced by springs, and a predefined cosine function is used for representing deformation profile of longitudinal steel. Through a large number of validations against experimental results, they proposed a reliable, yet simple, method

to handle with buckling problem and effective tie spacing. However, the fact that this method is primarily restricted to one type of structural elements (i.e., RC column), and some underlying assumptions—exclusion of accurate damage state of confined concrete, idealized deformation mode shape of longitudinal steel, and horizontal ties with fixed end—altogether preclude this method from having general applicability.

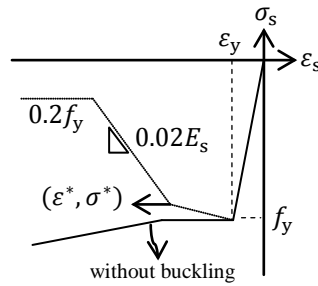


Figure 2.23. Initiation of compressive buckling and postbuckling behavior of longitudinal steel bar under compression (adapted from Dhakal and Maekawa 2002a).

Rodriguez et al. (1999) paid considerable attention to the postbuckling stress-strain behavior of reinforcing steel under cyclic loading, mainly in terms of the reduced modulus theory and a parameter pertaining to the maximum tensile strain ever reached. The suggested method appears to be capable of reproducing the buckling phenomenon, even at the unanticipated state (i.e., state of positive strain and negative stress) after reversal from excessive tension, which is consistent with the conclusion from many experimental results by Suda et al. (1996).

Monti and Nuti (1992) combined plasticity theory and empirical buckling model so as to cover various hardening models in the generic formulation, for the reinforcing steel subjected to both monotonic and cyclic loading. Their work markedly revealed the significant correlation between L/D and the onset of buckling; specifically, the buckling behavior appeared to be pronounced for the steels with L/D larger than 5. It should be stressed, however, that this approach was essentially restricted to the longitudinal steel bar with short length of single tie spacing, and all other major factors were neglected for the clarity of the study.

Pantazopoulou (1998) pointed out the significant role of properties of surrounding system (e.g., material property and amount of tie, compressive strain of core concrete, etc.) around the longitudinal steel bar after extensive review of confined RC column tests. He proposed an interrelationship among concrete deformation, required effective confinement and allowable tie spacing, mainly through mathematical and mechanical derivations as well as empirical model. It is noteworthy that he tried to describe the buckling and postbuckling behavior of longitudinal steel as a problem of entire system surrounding the longitudinal bar, not as a problem of the bar

itself. To elucidate the main goal of his research, however, he intentionally excluded the effect of cover concrete and shear distortion of the RC member.

Bae et al. (2005) performed a multitude of experiments on the buckling of reinforcing bars under monotonic loading condition, and presented intriguing factors such as initial geometric imperfection (in terms of eccentricity over diameter) and the ratio of the ultimate strength to the yield strength. This markedly implies that actual buckling can take place at lower stress or strain level than that of laboratory test since significant imperfection in geometry and interaction with surrounding element are most likely to exist in real RC structures exposed to cyclic loading.

It is of great importance to note, however, that all of existing formulations as to reinforcing bar buckling commonly rely on key assumptions—namely, ideally assumed deformation shape of longitudinal steel (mostly regarded as harmonic function), horizontally fixed ties, firmly fixed two ends of longitudinal steel bar allowing no horizontal displacement. In reality, the initially vertical alignment of longitudinal steel deforms in a very complicated way due to the rigorous interaction with surrounding system: cover and core concrete, horizontal steels such as ties and stirrups, and other longitudinal steels. This implies that longitudinal steel deforms in a rather arbitrary way, not in accordance with the idealized shape, and considerable horizontal movement of any segments of longitudinal steel are always predominant prior to the onset of buckling. Due to significant damage on cover and core concrete, the buckling appears to allow some movement of horizontal ties and stirrups. These deviations from the key premises of previous researchers becomes more pronounced when we include shear distortion of the RC member, which is essential in general three-dimensional RC elements such as relatively deep beam-column and shear wall system exposed to cyclic/seismic loading. All of these realistic phenomena render the previous formulations less effective in applications to general, real-scale RC structures exposed to cyclic/seismic loading.

2.7.2 Challenges of Existing Models

As mentioned before, previous studies as to reinforcing steel bar under monotonic/cyclic loading have provided tremendous insight into their nonlinear behavior, but at the same time they appear to have intrinsic restriction in several ways.

On one hand, a multitude of investigations (e.g., Kunnath et al. 2009; Dhakal and Maekawa 2002a; Rodriguez et al. 1999; Monti and Nuti 1992) of bar behavior under monotonic and cyclic loading has been conducted by idealized conditions as shown in figure 2.24(a)—namely, fixed ends allowing no rotational and translational movement, by enforcing the axial line (dashed lines) in figure 2.24 (a) to be unchanged. Also no surrounding entities are included for interfering lateral deformation along the length of the bar within the spacing. All of these postulations render the resultant resistance of bar weaker than that in actual reinforced system.

On the other hand, in the previous studies (Pantazopoulou 1998; Dhakal and Maekawa 2002b), the interaction between longitudinal bars and horizontal hoops are idealized by use of the assumed shape of longitudinal bar (mostly in harmonic function), and fixed springs for horizontal entities as depicted in figure 2.24(b). Contrarily, in reality the initially vertical alignment of longitudinal steel deforms in a very complicated way due to the rigorous interaction with surrounding system: cover/core concrete and horizontal steels such as ties and hoops as shown in figure 2.24(c).

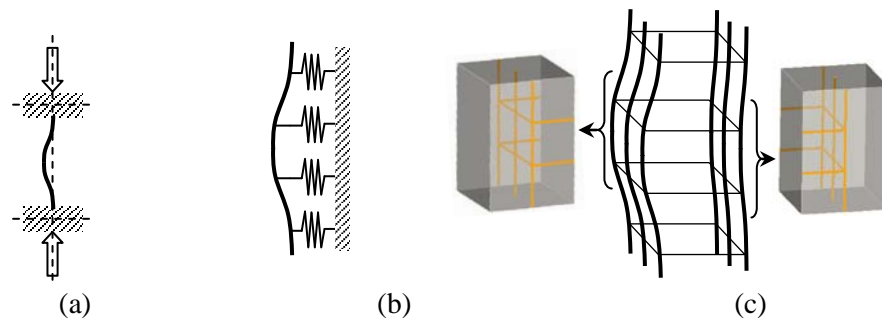




Figure 2.24. Study of reinforcing steel bar system from the idealized to realistic case: (a) typical reinforcing bar test setup with single spacing; (b) simplified bar system with horizontal ties represented by ideal springs; (c) realistic reinforced system of composite material.

Therefore, departing from both valuable understanding and some restrictions from previous studies, we aimed to propose a “*smart*” reinforcing steel model, which can be applied to general three-dimensional RC structures. Indeed, the advanced analysis platform with parallel computing offers unprecedented access to a great deal of microstates of materials and structural systems as

well as related information, and thus we can embark upon novel study as to the interaction between reinforcing bars and surrounding concrete in a systematic, topological information-based way. In essence, the “*smart*” reinforcing steel model is mostly dealing with information as to microstates of materials, topological state of the system, etc., giving rise to new paradigm of analysis of composite structures.

To this aim, bar elements can be classified into a number of types by distinct geometric attribute and interrelation with surrounding element set as given in table 2.1.

Table 2.1. Steel bar type definition and characteristics

	Type	Relation with Surrounding Element Set \mathcal{S} (SES)	Geometric Attribute
Steel bar	Perfectly bonded bar	Permanent SES; No change in buckling length	Simple curve 
	Longitudinal bar	Evolving SES and buckling length by compressive damage on SES	
	Tie	Only two end vertices possess SES; Degrading due to failure of ends' SES	
	Hoop	Only one key vertex holds SES; Degrading according to the key SES	Closed curve 

2.7.3 Definition of Topological Group

We start from presenting a systematic construction of a longitudinal steel group, which is defined by a set of connected bar elements as shown in figure 2.25. The topological information—two vertexes and directional vector of each bar herein—is queried to construct the longitudinal steel group.

First, following the notion of typical topology, we shall denote e^0 as a vertex, e^1 an edge, e^2 a face, and e^3 a volume.

We shall denote by LS the collection of all edges (i.e., longitudinal steel elements).

$$LS = \{e_1^1, e_2^1, \dots, e_{n_s}^1\}, \quad (2.60)$$

where e_i^1 signifies i_{th} edge (or i_{th} longitudinal steel element) and n_s is the number of total edges (or total longitudinal steel elements).

We shall define $C_0(e_i^1)$ as a set of two vertices e_j^0 and e_k^0 corresponding to both ends of the edge e_i^1 :

$$C_0(e_i^1) = \{e_j^0, e_k^0\}, \quad 1 \leq j \text{ and } k \leq n_n, \quad j \text{ and } k \in \mathbb{Z} \quad (2.61)$$

with n_n = number of total vertices (or nodes) of the structure. Also the directional vector defined by the two vertices is denoted as $\vec{C}_0(e_i^1)$.

In a similar fashion, we shall denote $C_1(e_i^2)$ as a set of edges constructing the face e_i^2 and also $C_2(e_i^3)$ as a set of all faces belong to the volume e_i^3 .

Thus, we can define a longitudinal steel group such that

$$LS = \cup_{j=1}^{n_{ls}} LS_j, \quad \cap_{j=1}^{n_{ls}} LS_j = \emptyset, \quad (2.62)$$

$$LS_j = \{e_i^1, i \in J_j\}, \quad (2.63)$$

where n_{ls} is the total number of longitudinal steel group estimated and the index set J_j satisfies

$$\begin{aligned} n(C_0(e_i^1) \cap C_0(e_k^1)) &= 1 \text{ and } \|\vec{C}_0(e_i^1) - \vec{C}_0(e_k^1)\| \ll 1.0, \\ \text{for } \forall i \neq k, \quad i \text{ and } k &\in J_j. \end{aligned} \quad (2.64)$$

In this simple manner, we can systematically construct whole set of longitudinal steel group. It is of interest to note that the criterion, eq. (2.64), proposed for the index set J_j of j_{th} longitudinal steel group can be further sophisticated to include more general situations, but eq. (2.64) is sufficient for the normal longitudinal steel bars with which the present study is mainly concerned for now.

The i_{th} longitudinal steel bar and its surrounding elements compose a set of base unit BU_i , ($1 \leq i \leq n_s$) as

$$BU_i = \{e_i^1\} \cup \{e_j^3, j \in B_i\} = \{e_i^1\} \cup \mathcal{S}_i \quad (2.65)$$

where the index set B_i satisfies

$$\{e_i^1\} \cap C_1(C_2(e_j^3)) = e_i^1, \quad \text{for } \forall j \in B_i \quad (2.66)$$

and in particular, we denote by \mathcal{S}_i only the surrounding elements of the base unit BU_i .

This concept for base unit is independent of particular family of finite element of three-dimensional body. Any three-dimensional elements sharing the edge representing the longitudinal steel bar will fall into the base unit of the bar. Hence, this systematic framework can hold for any three-dimensional finite element modeling.

For instance, figure 2.25 illustrates basic topological groups addressed so far. According to figure 2.25(left) five bars compose a longitudinal steel group LS_1 , and initial buckling length $L_b^{(i)}$ of i_{th} bar is assigned with original length of the bar $kL_0^{(i)}$. As generally accepted, the effective length factor k is set 0.5 which corresponds to fixed-ends condition. As shown in figure 2.25(right), four cubic elements compose the surrounding elements set \mathcal{S}_1 , and the set of base unit BU_1 consists of the steel (1) and \mathcal{S}_1 .

Longitudinal steel group: LS_i

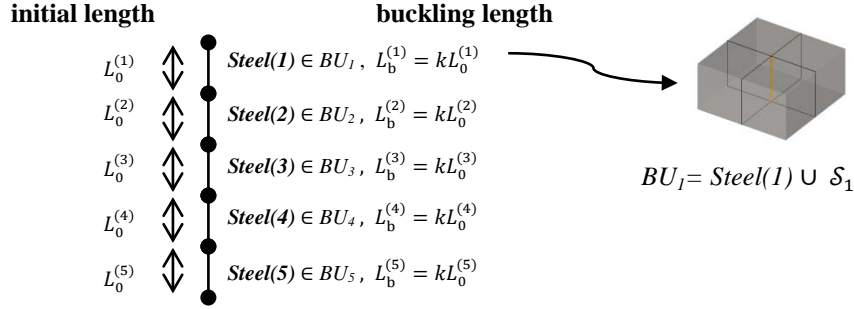


Figure 2.25. Basic topological groups: (Left) longitudinal steel group with initial buckling lengths initially assigned; (Right) The set of base unit consisting of one bar and its surrounding elements set.

In order to trigger topological transition of the base unit, we defined a new internal variable linked to the material nonlinearity of the surrounding elements. As loading (or time) step moves forward, update of the internal variable according to the assigned material nonlinearity happens at the set of base unit, and it provides information as to whether or not topological transition should occur, which will in turn, lengthen the buckling lengths of the longitudinal steel group.

It should be stressed that the present platform mainly focuses on the progressive buckling over the damaged space of structure. It is somewhat different from the progressive event over a certain period of time. Of course, the current progressive buckling happens over time, but the main interest we are concerned herein is the progressive buckling over space.

The determination of topological transition is fundamentally based on the physical phenomena, such as crushing, spalling, fragmentation, and so on, and we shall describe later the criteria adopted in present study. Generally, it can embrace any approaches to the material nonlinearity (e.g., classical plasticity, smeared crack model, particle model and so on) since what's important is only to convey the internal variable from S_1 to the corresponding steel, which can signal topological transition.

2.7.4 Topological Transition: Longitudinal Bar Type

Physically, it is hard to expect the onset of compressive buckling of longitudinal bar when some portion of the surrounding elements did not crush (or spall). This reasoning is based on the fact that the buckling is considerably affected by the bond between steel bars and surrounding elements, as well as the remaining resistance of uncrushed parts of surrounding elements. Therefore, as briefly illustrated in figure 2.26, a criterion for the updating of buckling length has been made in such a way that the topological transition can be triggered only when all surrounding elements enter at least partially crushed state. After the transition, we regard that bars lose their surrounding elements, and in turn, they can coalesce with adjacent bars, constructing new base unit pivoting around the lengthened bar.

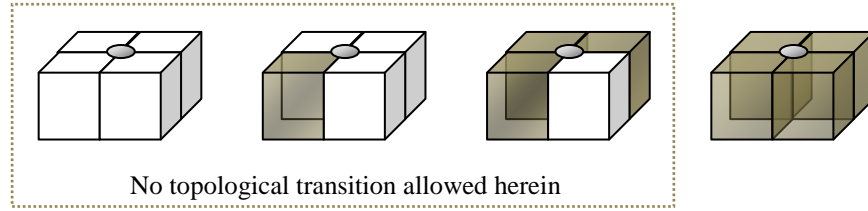


Figure 2.26. Criterion for topological transition according to damage on surrounding elements (gray color signifies at least partially crushed state of the element while white relatively intact state).

Recalling \mathcal{S}_m as a set of surrounding elements of a steel bar e_m^1 , topological transition of BU_m can be correlated to the dissipated energy of surrounding elements in \mathcal{S}_m as

$$\int_{\mathcal{S}_m} \sigma \, dV \geq E_{th}, \quad (2.67)$$

with a specific energy threshold E_{th} .

In the present smeared crack context, the total strain on the crack surface can be directly related to the dissipated energy. Therefore, above condition can be realized in terms of total strains defined on the three orthogonal crack surfaces. To this aim, two internal state variables are introduced: one is defined at each integration point level and the other at the element level.

It is noteworthy that Mode-I tensile crack is assumed to be incapable of causing topological transition. Unlike particular situations such as pure pull-out tests, the bond in the composites can

be regarded strong enough, and the concrete after complete closure of a Mode-I crack appears to fully regain its compressive resistance in real-scale RC structures.

We first introduce the internal state variable defined on the integration point level. Let $\alpha_i^{(k)}$ be an internal state variable of k_{th} crack surface, $k \in \{1,2,3\}$, defined on i_{th} integration point, describing uncrushed state by 1 and crushed state by 2

$$\alpha_i^{(k)} = \begin{cases} 1 & \text{for } \min_t \varepsilon_k^{cr} \geq \varepsilon_{th} , \\ 2 & \text{otherwise,} \end{cases} \quad (2.68)$$

with ε_{th} strain threshold for entering crush phase, which is assumed in this study as the strain associated with the compressive strength.

Then, we can further define an element level internal variable φ_j which can signify intact, partially crushed, and fully crushed states of an element by use of simple integer values, 0, 1, and 2 respectively. In detail, when all the integration points in an element undergo crushed phase we assign 2 to φ_j . When only some of the integration points in an element enter crushed phase, we regard the element partially crushed denoted by 1, while intact state of an element is denoted by 0 if none of the integration points experiences crushed phase. With the aid of the simple integer-based state variable we have

$$\varphi_j = \begin{cases} 0 & \text{for } \beta_j \leq \text{NINT}^{(j)} \times 3, \\ 1 & \text{for } \text{NINT}^{(j)} \times 3 \leq \beta_j \leq \text{NINT}^{(j)} \times 6, \\ 2 & \text{for } \beta_j \geq \text{NINT}^{(j)} \times 6, \end{cases} \quad (2.69)$$

with $\text{NINT}^{(j)}$ = number of total integration points of j_{th} element $\in \mathcal{S}_m$ and

$$\beta_j = \sum_{i=1}^{\text{NINT}^{(j)}} \sum_{k=1}^3 \alpha_i^{(k)}. \quad (2.70)$$

For the conservative prediction, if all surrounding elements enter partially crushed phase, the topological transition is assumed to take place, which can be ascertained by

$$\sum_{j=1}^{n(\mathcal{S}_m)} \varphi_j \geq n(\mathcal{S}_m), \quad (2.71)$$

where $n(\mathcal{S}_m)$ means the number of surrounding elements in \mathcal{S}_m . Hence, once above condition is violated, the topological transition is triggered and the buckling length of the corresponding reinforcing bar can evolve by merging with adjacent bars' buckling lengths. Table 2.2 summarizes the data structure needed for the smart steel bar model. And this structure is efficiently queried for the parallel implementation as dealt with in later section.

Table 2.2. Data structure in smart steel bar model

Data	Data Holder
Integration point level, internal state variable $\alpha_i^{(k)}$, $k \in \{1,2,3\}, \quad i \leq \text{NINT}^{(j)}$	$e_j^3 \in \mathcal{S}_m, \quad j \leq n(\mathcal{S}_m)$ solid elements in $\mathcal{S}_m \in BU_m$
Element level, internal state variable φ_j	
Evolving buckling length $L_b^{(m)}$	$e_m^1 \in BU_m$

As shown in figure 2.27, for instance, among five bars, three bars at the bottom merged to form the new base unit having the lengthened buckling length due to the topological transition caused by crushing of the surrounding elements.

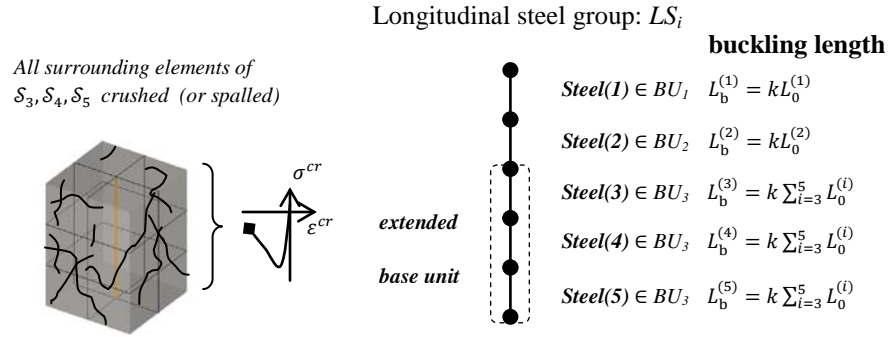


Figure 2.27. Example of topological transition and evolving buckling lengths.

2.7.5 Remarks on Parallel Implementation

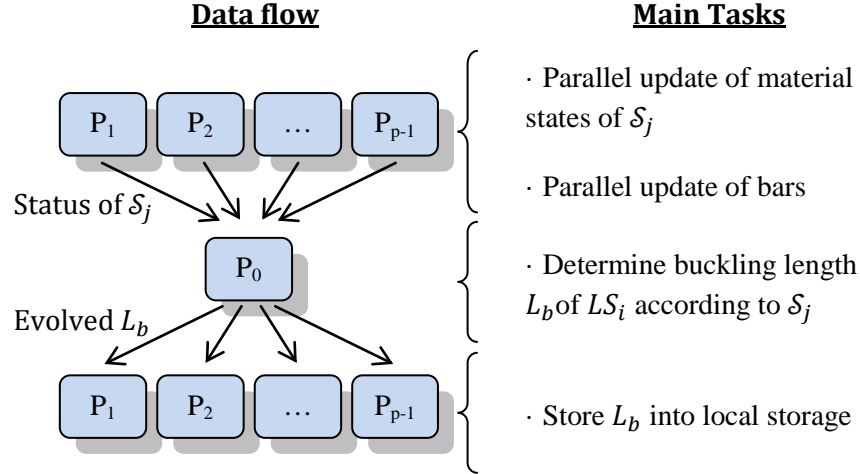


Figure 2.28. Schematic description of parallel update of compressive buckling of steel bars by means of “master-slaves” strategy.

Like nonlinear element update procedures, the compressive buckling length update tasks are carried out by means of “master-slaves” parallel strategy. Figure 2.28 provides schematic description as to which data is transferred between slave processors ($P_1 \sim P_{p-1}$) and the master processor (P_0), which tasks are concurrently performed on slaves, and which job should be done on the master processor.

Intuitively, some tasks are embarrassingly parallelizable, which are including updating nonlinear material states of both surrounding elements of \mathcal{S}_j and nonlinear bars, and storing the evolved buckling lengths into local storage. However, determination of new buckling length according to current damage status of all \mathcal{S}_j is to be effectively done on the master processor.

Reasons behind this parallel strategy are related to the nonoverlapping domain decomposition rule adopted in the platform. As will be dealt with in detail in section 3.8, the longitudinal steels are distributed such that no subdomains share the same steel bar, and thus, each steel bar resides exclusively on a subdomain. In particular, the nonoverlapping domain decomposition is carried out mainly with respect to the solids elements, not the steel bars.

Suppose, for instance, a particular set of surrounding element \mathcal{S}_j which is related to a steel bar e_j^1 , both constructing a set of base unit $BU_j = \{e_j^1\} \cup \mathcal{S}_j$. And such a nonoverlapping domain decomposition in terms of solid elements might lead to the situation that not all entities of \mathcal{S}_j are lying on a subdomain Ω_k which holds the steel bar e_j^1 , i.e., $e_j^1 \in \Omega_k$ but $\mathcal{S}_j \not\subset \Omega_k$. Furthermore, it

is natural to expect that a longitudinal steel bar group LS_i is most likely to span several subdomains, e.g., $LS_i \subset \cup_k \Omega_k$.

Therefore, to effectively overcome such data complexity as to steel bars, we adopted a straightforward parallel strategy to update buckling lengths of all longitudinal steel groups by means of the master-slaves concept.

2.7.6 Generalized Menegotto-Pinto Steel Model

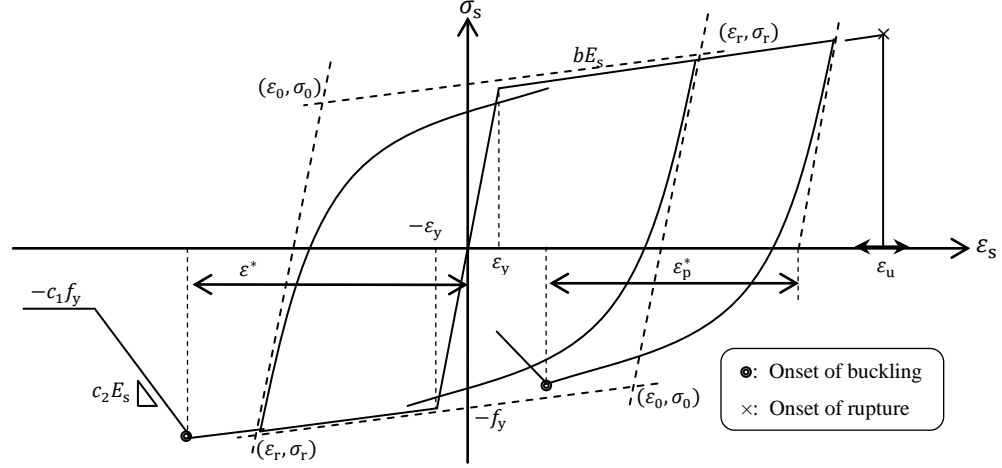


Figure 2.29. Longitudinal steel hysteresis model with compressive buckling and tensile rupture.

One of the most reliable cyclic hysteresis models for reinforcing steel bar under cyclic loading is the one proposed by Menegotto and Pinto (1973), and there have been a large number of variants of it. The Menegotto-Pinto (MP) steel model enables the smooth transition during the reversal loading, which is in accordance with the Bauschinger effect. The original MP steel model updates current stress from a fairly simple constitutive relation:

$$\sigma' = b\epsilon' + \frac{(1-b)\epsilon'}{(1 + \epsilon'^R)^{1/R}} \quad (2.72)$$

where $b = E_2/E_s$, $\epsilon' = (\epsilon - \epsilon_r)/(\epsilon_0 - \epsilon_r)$, $\sigma' = (\sigma - \sigma_r)/(\sigma_0 - \sigma_r)$. As shown in figure 2.29, (ϵ_0, σ_0) means the intersection point between two asymptotes with slopes E_2 and E_s , and (ϵ_r, σ_r) indicates the point from which un/reloading began. The transition parameter R can be obtained by

$$R(\xi) = R_0 - \frac{a_1 \xi}{a_2 + \xi} \quad (2.73)$$

where R_0 , a_1 , and a_2 are constants (20.0, 18.5, and 0.15 were recommended), which can be attained from calibration against experiments.

And the ξ at iteration step (i) is defined as

$$\xi^{(i)} \equiv \frac{|\epsilon_r^{(i-1)} - \epsilon_0^{(i)}|}{\epsilon_y} ; \quad |\epsilon_r^{(j)}| \geq \epsilon_y \text{ for } \forall j, \quad (2.74)$$

which means that at current excursion ξ is the normalized distance between the strain of the previously converged un/reloading point and the strain at the current intersection point. It should be noted that the minimum absolute value of ε_r is set as the strain at yielding point, and ξ remains unchanged during local un/reloading situations (i.e., when un/reloading happens within the previous maximum and minimum strain range in an arbitrary number).

Although there have been many sophisticated modifications of the MP steel model—notably, Kunnath et al. (2009) made an attempt to include bar buckling, low-cycle fatigue failure, and cyclic degradation—in the present study we focused on the effect of evolving buckling length mainly by the rigorous interaction with surrounding brittle materials. Hence, the simple generalization of the MP steel model has been suggested herein to include compressive buckling and tensile rupture.

In order to tackle the buckling length of bar in a simple and balanced manner, we started from the work by Dhakal and Maekawa (2002a). Primarily following the key notion of Dhakal and Maekawa (2002a), the proposed longitudinal steel model has the intermediate point ε^* at which compressive buckling initiates. The strain of the intermediate point is calculated from eq. (2.58), originally proposed by Dhakal and Maekawa, and the plateau of monotonic response prior to hardening regime is not included for simplicity.

Apparently, the length term plays an essential role in determining the initiation of compressive postyield buckling as seen in eq. (2.58). This is true even for the elastic buckling, recalling the Euler formula $\pi^2 EI / (kL)^2$ for the critical force. In order to provide a physically accurate value to the buckling length, the topological transition information is being queried to ascertain the active buckling length L_b of each base unit. For instance, buckling length of a steel bar in a base unit BU_m is estimated by

$$L_b \equiv \sum_{L_0^{(i)} \text{ of } e_i^1 \in BU_m} k L_0^{(i)}. \quad (2.75)$$

And, in turn, this evolved buckling length feed the latest information to the process of new buckling initiation point ε^* as

$$\frac{\varepsilon^*}{\varepsilon_y} = 55 - 2.3 \sqrt{\frac{f_y}{100} \frac{L_b}{D}}; \quad \frac{\varepsilon^*}{\varepsilon_y} \geq 7, \quad (2.76)$$

where ε^* is the intermediate strain where buckling initiates; ε_y and f_y are the strain and stress [MPa] at yielding; L_b is the buckling length calculated; D is diameter of the cross section; k is effective length factor set as 0.5 for fixed boundary condition.

Once the current strain exceeds this intermediate point ε^* calculated from eq. (2.76), the stress decreases with the slope $c_2 E_S$ (recommended: $c_2 = 2\%$) until it reaches residual strength $c_1 f_y$ (recommended: $c_1 = 20\%$), and thereafter stress is assumed to remain constant as depicted in figure 2.29.

At the same time, the excessive tensile strain during the cyclic loading can cause compressive buckling by employing the fixed strain parameter concept of Rodriguez et al. (1999). As shown in figure 2.29, if the strain parameter ε_p^* reaches ε^* after reversal from tension, compressive buckling is assumed to occur, being able to capture early buckling at positive strain after large tensile loading. As widely accepted, compressive buckling has little effect on the subsequent tensile response. Therefore, the unloading response after onset of buckling is assumed to head to the maximum strain point previously reached. This can be physically understood by the process that the longitudinal steel largely bent due to the compressive buckling tends to regain the longest length previously had, and then fully recover its tensile resistance.

2.7.7 Example of Topological Transition-Based Buckling

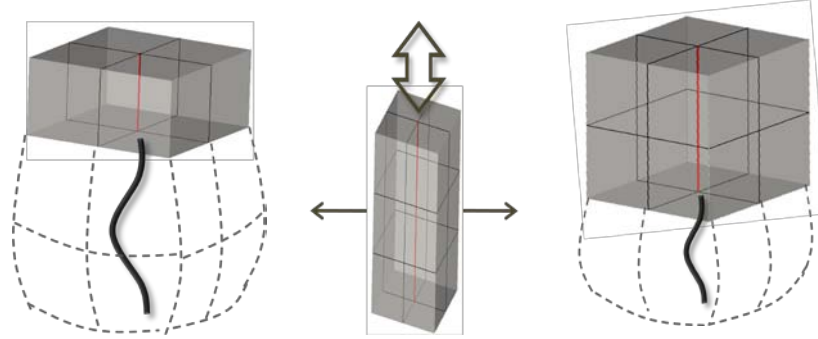


Figure 2.30. Contrast between buckling modes intentionally generated: (Middle) a cyclically loaded column consisting of a longitudinal steel bar and three layers of surrounding elements; (Left) when two bottom layers failed first; (Right) only bottom layer failed.

To investigate the distinct buckling behavior due to different compressive failure of surrounding elements, a simple example of three layers block including longitudinal steel bars is imposed by cyclic vertical loading as shown in figure 2.30(middle). Deformed shapes of bars are exaggerated in dashed lines (figure 2.30 left and right). And relatively weak compression properties are assigned to two bottom layers (left) while to one bottom layer only (right). As shown in figure 2.30(left), since surrounding elements in the two bottom layers crushed first, we expect buckling length twice longer than that from one weak bottom layer only (right).

Such a situation has been exactly predicted by simulations as presented in figure 2.31, and topological transition appears to precisely lengthen the buckling length of the longitudinal bar. Figure 2.31(left) shows stress-strain response of longitudinal steel bar at bottom layer which confirms obviously different compressive buckling behavior of aforementioned two cases. For a reference, figure 2.31(right) provides completely crushed states of surrounding elements at the bottom layer obtained from the simulations.

It is of interest to note that early buckling behavior by reversal from excessive tensile loading is also successfully captured by the simulation as shown in figure 2.32. According to figure 2.32, even the early initiation of compressive buckling reveals strong dependence on the evolving buckling length, as expected.

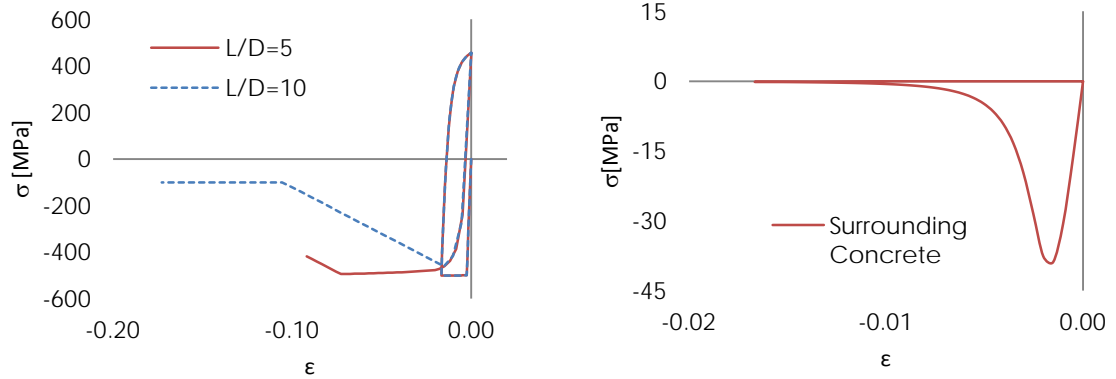


Figure 2.31. Predicted stress-strain response revealing different buckling lengths triggered by topological transition (Left), which are based on the compressive failure of surrounding elements (Right).

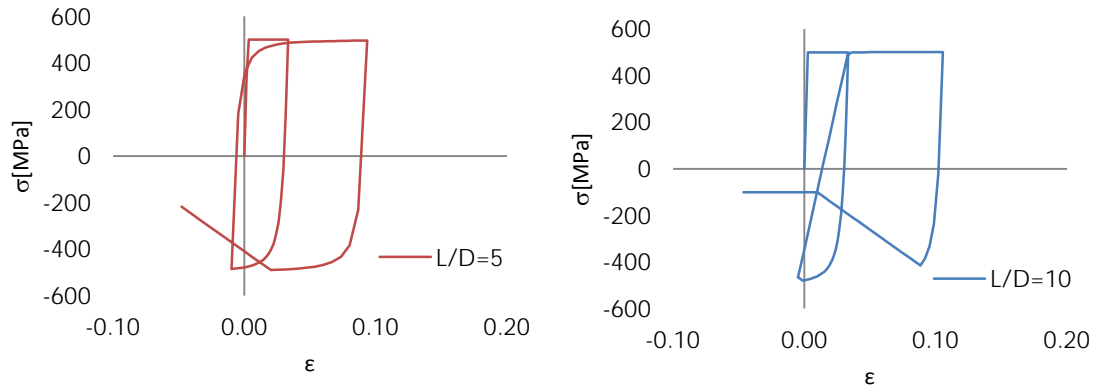


Figure 2.32. Onset of early buckling captured by the simulations revealing distinct initiation point of buckling due primarily to evolving buckling length by topological transition.

2.7.8 Steel Bar Models Implemented in the Present Work

Departing from simple bilinear steel model, compressive buckling effect has been incorporated into the bilinear steel bar model, and afterwards it has been further extended to the well known MP steel model. Hence, in the present platform, three types of steel bar models are available—namely, bilinear, bilinear with compressive buckling, and Menegotto-Pinto with compressive buckling. All the buckling models are utilizing the information from topological transition as demonstrated so far.

Detailed input format related to each steel bar model is provided in appendix B.

Chapter 3 PARALLELIZATION STRATEGIES

3.1 Outline of Parallel Platform Developed

As the computing capacity evolves, the desire to accurately predict nonlinear behavior of RC structure to its ultimate state has been also increasing. Especially researchers in earthquake engineering have been the most enthusiastic pioneers who quickly absorbed state-of-the-art analysis technology with the newest computing power. For instance, in studying shear wall system, one of the most complicated structural elements often employed to resist shear by seismic loading, there has been drastic change in attempts to increase accuracy with the aid of advanced computing capability: from the simplified nonlinear spring model connecting two rigid bodies (Cheng et al. 1993) or equivalent beam-column model (Colotti 1993), the fiber section model incorporating nonlinear shear spring (Orakcal and Wallace 2006), and to continuum-based shear wall model that allows investigation of complicated system, such as RC elements repaired with fiber-reinforced polymer or partly repaired shear wall system (Kim and Vecchio 2008; Vecchio et al. 2002). Similar evolution in analysis of RC beam-column element is well documented in a review by Spacone and El-Tawil (2004).

In the computational point of view, the intrinsic obstacles to the advanced microscopic analysis are the memory shortage and expensive computation cost, normally found in the fiber section model and crack-embedded continuum model. Furthermore, the intensive global iterations (and/or local iterations for state values) for the converged solution are essential in most cases.

Therefore, there has been a multitude of attempts to develop parallel FEA platform: ParaDyn (Hoover et al. 1995; DeGroot et al. 1997), ParAble (Danielson and Namburu 1998; Danielson et al. 2008), Parallel explicit dynamic FEA program on heterogeneous workstation (Sziveri and Topping 2000), and so on. More detailed review of parallel processing in civil engineering can be found in a paper by Sotelino (2003).

However, most of the precedents are restricted to limited fields; some focused on the methodologies as to parallel computing of large scale structure while others dealt with monotonic forces such as shock or blast loading, running on “*explicit*” dynamic analysis program which is characteristically easy to be parallelized. On the contrary, parallelizing “*implicit*” nonlinear FEA programs is difficult due to its nature, which is still being tackled by many researchers. Furthermore, there has been little attempt to convert an existing FEA program for RC structure to its parallel version. Specifically, the displacement-controlled nonlinear FEA program for RC structure has been rarely developed in a parallel version, although it is very important in earthquake engineering since cyclically loaded test is essential in assessment of the resistance of structure against earthquake loading.

In the present work, efficient parallelization strategies, by which an existing displacement-controlled nonlinear FEA program is transformed into its parallel version, has been suggested. Especially the parallel platform is mainly aimed at the moderate size structures, and focused on embracing physics-based mechanisms. Being “*moderate*” means that the size of structure is sufficiently big for a single or several processors in terms of time cost, but it does not necessarily require more than several hundred processors.

In this chapter, a review of key features of the existing serial version shall be addressed first after touching upon other parallel algorithms in broader areas of engineering and science. Then quantitative comparison among the representative advanced parallel strategies shall be provided, leading to a selection of a parallel strategy to be tuned for the present problem later. As will be discussed in detail, by virtue of the penalty method, the modified Newton-Raphson (NR) iteration using initial stiffness still retains superiority in the parallel version. An optimized parallel triangular system solving with the factorized stiffness also achieves superiority over other advanced parallel solvers such as parallel preconditioned conjugate gradient method (PCGM). Other parallelization issues regarding cyclic global data distribution, “*divide-and-conquer*” strategy, domain decomposition, and so on shall also be dealt with.

Brief summary of the physics-based degrading material models which became available by the parallel platform shall be given. Furthermore, practical applications to real-scale three-dimensional RC structures exposed to the cyclic loading shall be provided in the ensuing chapter to ensure the parallel efficiency of the developed implicit, nonlinear parallel analysis program.

3.2 Review of Parallel Computing in Broader Fields

Indeed, the parallel computing has been obtaining tremendous attention in fields of general engineering and science in order to tackle a multitude of problems we encounter. In this section, some of the representative works and their notable characteristics are summarized, giving valuable insight into productive understanding as regards those attempts with parallel algorithms.

Rahul and Suvranu De (2010) proposed a coarse-grained parallel algorithm mainly suitable for multiscale analysis on parallel platform. In the proposed coarse-grained algorithm, a number of “*master*” processors are responsible for macroscopic analysis whereas each master processor can spawn a sufficient number of “*slaves*” to conduct microscopic analysis. By comparing costs from numerical simulations, they demonstrated that their coarse-grained algorithm holds better efficiency than a naive algorithm with one master node and many slaves. It should be noted that, however, the parallel implementation and conclusion are essentially rooted in simulations of *explicit* multiscale analysis, and therefore direct extension of their schemes to highly intricate cases involving *implicit* nonlinear analysis might not guarantee the desired parallel efficiency.

Namazifard and Parsons (2004) established an algebraic framework for parallelizing multigrid method. Using MPI library and distributed memory environment, remarkable parallel performance has been proven from simulation tests of large scale three-dimensional solid mechanics problems.

Even in field of GIS (geographic information system), some problem-optimized parallel algorithms have been suggested by Clematis et al. (1998). Rather than simple cases where “*local*” computation is dominant (hence easily parallelizable), they mainly tried to tackle “*nonlocal iterative*” problems (e.g., drainage basins extraction) by proposing efficient parallelization strategies. Here, nonlocality stands for the circumstances that clear, simple division of the domain is nearly impossible. In their work, first, they showed that the “*virtual memory*” strategy—each processor often needs to access indispensable data of the contiguous subdomains through the tuple space—tends to perform poorly due to the required communication overhead in their problems under consideration. Then, they proposed as a successful alternative the “*large overlap subdomains*” strategy, in which the subdomain on a processor is statistically defined to hold extended region of the domain rather than clearly divided one. In this way, the communication cost required to access the tuple space can be considerably reduced while keeping the increased memory cost for the overlapping portion is relatively small.

Based on the characteristics addressed so far, distinct domain/tasks decomposition strategies are illustrated, and typical parallelization scheme for most “*explicit*” algorithms is given as well (figure 3.1 ~ figure 3.3). It is apparent that the parallelization strategy is essentially problem-dependent, and each strategy holds its own advantage and shortcoming. Therefore, special

attention should be paid at the early stage of establishing parallelization scheme for a problem under consideration, so that the parallelized engine successfully takes into account the degree of locality of major tasks, balanced use of communication, and possibility of data distribution over processors available.

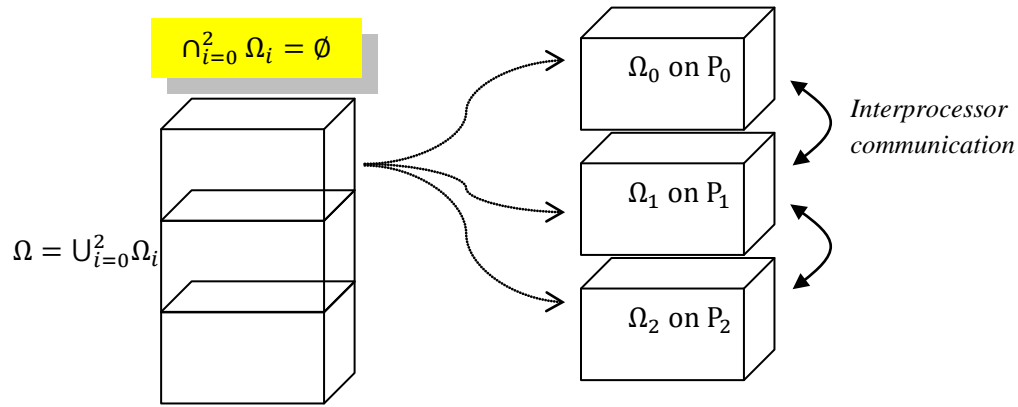


Figure 3.1. Nonoverlapping domain/tasks decomposition strategy, widely used in “*explicit*” algorithms.

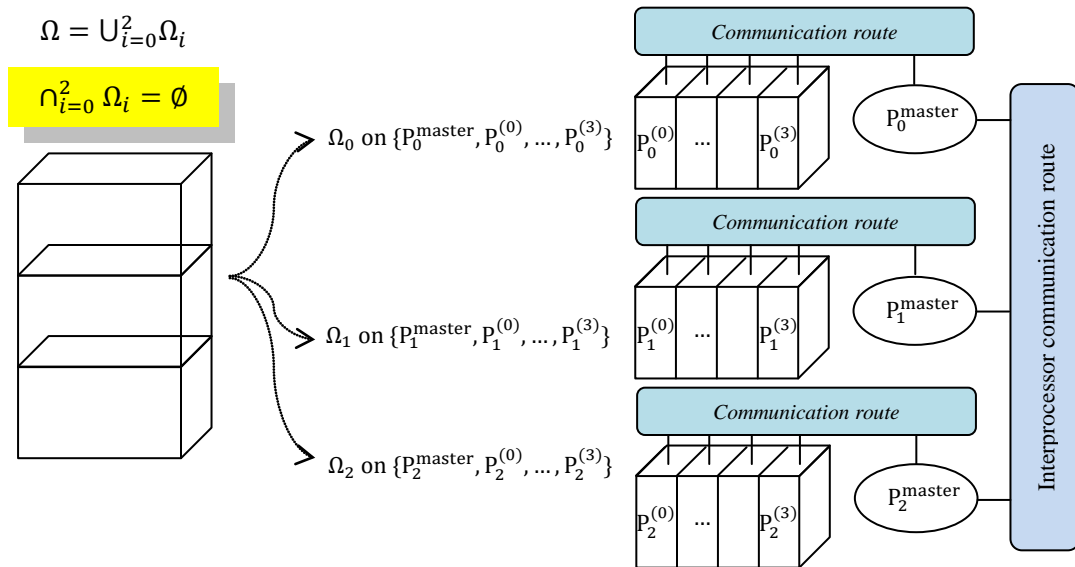


Figure 3.2. Coarse-grained domain/tasks decomposition strategy (e.g., used in hierarchical multiscale analysis), notably with the distinct communication schemes.

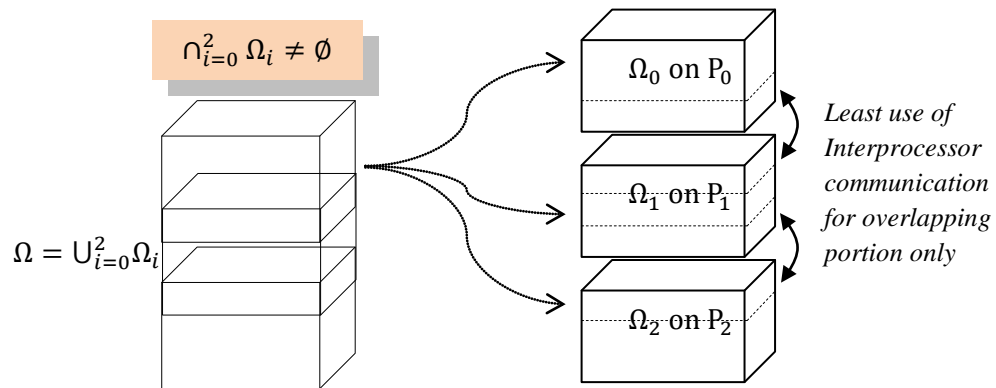


Figure 3.3. Partially overlapping domain/tasks decomposition strategy (e.g., some GIS algorithms with intrinsic “nonlocality”).

3.3 Key Characteristics of the Serial Version Program

As summarized in table 3.1, the main stream is twofold: static analysis (A) for initial loading followed by nonlinear analysis (B). At the beginning of the nonlinear analysis (B–1) the global stiffness matrix is augmented by additional penalty elements and then stored in its factorized form (B–2). The ensuing displacement-controlled analysis stage consists of the two major loops: main iteration loop (B–3) to obtain the required external forces corresponding to the target displacement and inner iteration loop (C) for modified NR-iteration using the factorized stiffness.

Although the full NR-iteration is common in most nonlinear analysis for its fast convergence rate, the modified NR-iteration using initial stiffness had been adopted to fully take advantage of the penalty method. Indeed, the penalty method essentially imparts sufficient smoothness to the global force-displacement response, and as it turned out in most numerical simulations, marching with initial stiffness yields the converged response in several iteration steps, allowing us to perform triangular system solving with \mathbf{K}_{LU} repeatedly. Consequently, we can save expensive cost in tangent stiffness reconstruction and its redistribution along processors, leaving only two factorizations in static and nonlinear analysis stages—notably, they are still significant bottlenecks in the main execution stream.

Table 3.1. Flow of serial version of displacement-controlled nonlinear FEA program

A. Static Analysis Stage: $\mathbf{K}\mathbf{u} = \mathbf{F}$
B. Displacement-controlled nonlinear analysis stage:
B–1. Augment stiffness by penalty method
$K_{ij} = K_{ij} + K_{penalty} \times \gamma_{ij}$
where $K_{ij} \in \mathbf{K}$, $K_{penalty} \gg \max(\mathbf{K})$,
$\gamma_{ij} = \begin{cases} 1 & \text{when related to penalty element} \\ 0 & \text{otherwise} \end{cases}$
B–2. Factorize \mathbf{K} and store into \mathbf{K}_{LU}
B–3. Displacement loading loop: Find external
force $\Delta\mathbf{F}$ corresponding to $\Delta\mathbf{u}$

C. Modified NR-iteration using \mathbf{K}_{LU}

Solve $\mathbf{K}_{LU}\delta\mathbf{u}^i = \delta\mathbf{F}_{temp}^i$ at step i

When converged, $\Delta\mathbf{u} = \sum \delta\mathbf{u}^i$; $\Delta\mathbf{F} = \sum \delta\mathbf{F}_{temp}^i$

3.4 Quantitative Study on the Advanced Parallelization Strategies

Parallelization is essentially problem dependent, and how successfully embracing the distinct features of the problem under consideration appears to be crucial. Although qualitative analysis of a separate parallel algorithm is widely available, quantitative comparison among advanced parallel algorithms is not well documented so far. So, a comparative study on the parallel strategies, particularly in terms of factorization, has been conducted. Then optimizations of the selected parallel algorithm are suggested to exploit the unique features: highly banded nature and small portion of the stiffness matrix being affected by addition of penalty elements.

Among a multitude of the advanced parallel strategies, three representative ones, in terms of factorization, are studied herein: (1) broadcasting, (2) pipelining, and (3) look-ahead method (e.g., Casanova et al. 2009). Associated pseudocodes are provided in appendix C.

Before moving forward, it is useful to denote the key procedures of serial version factorization. Let $P(k)$ be the preparation procedure at step k : preparation of factors for the sub rows below the k_{th} diagonal term performed on the processor P_k (P_k = the processor holding the k_{th} column and diagonal term). Let $U(k)$ be the update procedure at step k : update of submatrix $A_{i,j}$ for $i, j > k$ with the precalculated factors with k_{th} diagonal term.

The first and simplest parallelization strategy is the broadcasting scheme using direct broadcasting command in MPI (i.e., *MPI_Bcast*) at each step. The key stream can be summarized as: $P(k) \rightarrow \text{broadcasting to all processors} \rightarrow U(k)$. It is remarkably easy to understand and implement, and indeed the broadcasting command can be almost freely interleaved into the routine. The key drawback of this approach, however, is that all other processors need to wait until the data from the sender processor P_k until $P(k)$ is fully finished on P_k at each step, causing unnecessary waiting cost between processors. Furthermore, the broadcasting command itself possesses communication inefficiency as the number of processors increases.

To expand on this adverse nature, it is instructive to review the cost analysis of two algorithms—(1) parallel factorization followed by triangular system solving (Karniadakis and Kirby 2003) and (2) parallel Gaussian elimination (Casanova et al. 2009) —both based on simple broadcasting approach, and the total costs generally read

$$\text{Total running time} \approx \frac{\alpha'}{p} + \beta'p, \quad (3.1)$$

where $\alpha' = \alpha \times n^3 / 3$; $\beta' = (\beta n^2 / 2 + L)$ or $(\beta n^2 + L)$ for the former and the latter, respectively. And α is basic operation cost per element; β is transfer cost per element; L is communication startup cost; n is system size; p is the total number of processors.

Detailed derivation of the cost model given in eq. (3.1) shall be addressed in section 3.5.

If $n \gg p$, then the first term in eq. (3.1) will govern the total running time, and we can achieve an asymptotic parallel efficiency of order 1. For a moderate size of n , however, the effect of the second term in eq. (3.1) cannot be ignored, and simply increasing the total number of processors cannot guarantee the parallel efficiency. Indeed, the total cost will undesirably increase with the growth in the number of total processors by the second term of eq. (3.1), as shown in figure 3.4. Hence, the simple broadcasting scheme is assumed to be the simplest yet poorest one in the later discussion, and used as the comparison base for other advanced parallel strategies.

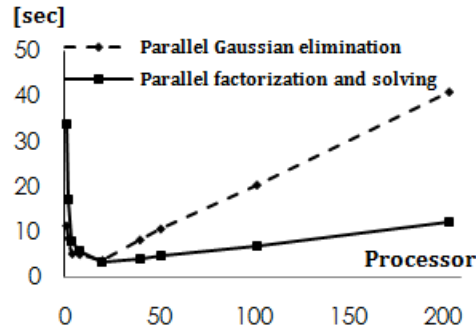


Figure 3.4. Costs of parallel factorizations attained from numerical simulations of a test system (size=2040): parallel Gaussian elimination (dashed line) and parallel factorization followed by triangular system solving (solid line).

The second one is the pipelined algorithm following the key notion of “*pipelining*,” in which logical topology is well incorporated. In the scheme, every processor knows its logically closest one, and upon receiving the crucial data, a processor always passes the buffer to the closest processor, and then performs $U(k)$. In this fashion, waiting cost between processors can be remarkably reduced and the communication is efficiently accelerated. However, there still exists some latency, so-called “*pipeline bubble*” due to the difference of the computation time between the predecessor and successor, and the strictly fixed stream—namely, $P(k) \rightarrow$ receiving/immediate sending $\rightarrow U(k)$.

The third and most advanced parallel algorithm is the so-called “*look-ahead*” scheme, which is not only considering logical topology, but also reducing pipeline bubble by placing top priority on communication over computation—if necessary for fast communication, sacrificing a

consecutive computation often happens. It should be stressed, however, that in the look-ahead method the total time cost might become very expensive with small number of total processors, even worse than the simple broadcasting method, since with a small number of processors the serial computation usually governs the total cost rather than communication.

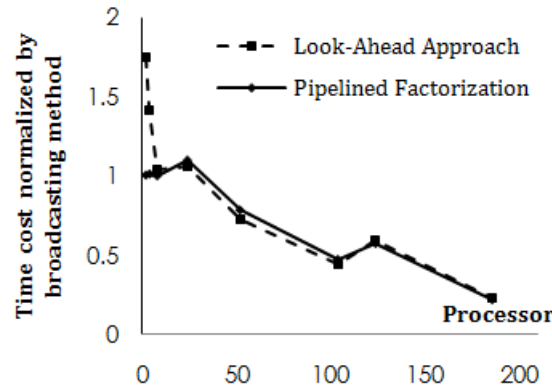


Figure 3.5. Costs of look-ahead and pipelined factorization normalized by that of broadcasting method, all attained from simulations of a test system (size = 19176).

Figure 3.5 shows that both pipelined and look-ahead methods exhibit highly improved efficiency compared to simple broadcasting method. As pointed out, however, the poor performance of look-ahead method for small number of processors is noteworthy (e.g., for processors less than 24). Unlike look-ahead approach, however, the pipelined factorization method does not show poor performance even for small number of processors compared to the simple broadcasting method.

In sum, provided that a sufficiently large number of total processors are available, the look-ahead method can be regarded as the best parallel algorithm, but the advantage over pipelined algorithm is not significantly noticeable for a moderate size system. Furthermore, the look-ahead algorithm tends to perform badly for small number of total processors. Therefore, the present parallel platform adopted the pipelined strategy as the starting point, on which optimization in accordance with key features of the program of interest were carried out.

3.5 Cost Model for Parallel Factorization

More often than not, it is of practical importance to have knowledge as to the cost trend of some representative parallel algorithms. So, we expand on the cost analysis of some representative parallel algorithms and investigate the overall behavior of the costs.

To begin with, we look into the cost of parallel factorization.

Many parallel algorithms are based on the uniform distribution scheme—blocks of consecutive matrix rows (or columns) are assigned across all the processors for matrix-vector or matrix-matrix multiplication as an instance. However, such simple distribution scheme ignored the distinct feature of main stream of factorization:

- (i) As the step number k increases, the number of columns to be updated decreases.
- (ii) Computation is not simply proportional to the amount of data, say column k needs k updates.

Therefore, in the present implementation, the cyclic allocation method is being employed to balance the computation load and communication cost. Before investigating the total running time of the parallel factorizations, it is valuable to start from the cyclic allocation to study its behavior and efficiency first.

3.5.1 Behavior of Cyclic Allocation Scheme

The column-based cyclic allocation scheme scatters columns (or rows in row-based one) of the given matrix in a cyclic manner as: column $j \rightarrow$ Processor $P_{j \bmod p}$. (i.e., mynode $q = k \bmod p$).

To investigate the computation cost in the cyclic allocation method, consider the number of update operation for column j at step k :

$$\begin{aligned} \text{Number of update operation for column } j \\ = (n - 1) - (k + 1) + 1 = n - k - 1 \end{aligned} \tag{3.2}$$

Hence, total number of update operation on elements by processor containing column j is defined by $ops(j)$:

$$\begin{aligned}
ops(j) &= \sum_{\text{step } k=0}^{(j-1)} (n - k - 1), \\
&= (n - 1)j - \frac{(j - 1)(j)}{2} = -\frac{1}{2}j^2 + \left(n - \frac{1}{2}\right)j.
\end{aligned} \tag{3.3}$$

Cyclic distribution causes processors P_i to contain $(lp + i)$ columns (for $l = 0, \dots, \frac{n}{p} - 1$). For instance, for $p=2$ and $n=6$, processor P_0 has column 0, 2 and 4 whereas P_1 holds column 1, 3 and 5.

Thus, the total update operations done by P_i are defined by $Ops(i)$:

$$Ops(i) = \sum_{\text{column } l=0}^{\frac{n}{p}-1} ops(lp + i) \tag{3.4}$$

$$= \sum_{\text{column } l=0}^{\frac{n}{p}-1} -\frac{1}{2}(lp + i)^2 + \left(n - \frac{1}{2}\right)(lp + i) \tag{3.5}$$

$$= \frac{n}{p} \left\{ -\frac{1}{2}i^2 + \frac{1}{3}\left(n - \frac{3}{4}\right)n + i \left(-\frac{1}{2} + \frac{1}{2}n + \frac{1}{2}p \right) + \frac{1}{4}p - \frac{1}{4}np - 0.0833p^2 \right\} \tag{3.6}$$

$$\therefore Ops(i) = \frac{n^3}{3p} + O(n^2). \tag{3.7}$$

And this total update operation of processor i is asymptotically independent on processor number i , so with large n all the processors performs the same amount of update operations, i.e., $\frac{n^3}{3p}$. Also, it turns out that the column preparation cost is asymptotically negligible by cyclic allocation.

3.5.2 Total Cost of Parallel Factorization with Cyclic Allocation

Then, consider the total cost of parallel factorization which is involving cyclic data distribution scheme. The major concern is the total cost of parallel factorization which is accompanied by triangular system solving, and the parallel Gaussian elimination will be dealt with separately in the following.

The total running time is comprised of two parts:

$$\text{Total Running Time} \equiv \text{Total Computation Cost} + \text{Total Communication Cost}.$$

Firstly, the total computation cost can be obtained as discussed in the previous section.

$$\text{Total Computation Cost} \approx \frac{n^3}{3p} \alpha \quad \text{for } n \gg 1, \quad (3.8)$$

where α is the basic operation cost per element.

As expected, the total computation cost has asymptotical parallel efficiency of 1 as n grows large. Next, the total communication cost is obtained as followings.

$$\text{Total Communication Cost} = p \times \left[\sum_{k=0}^{n-2} \{ \beta \cdot (n - 1 - k) \} + L \right], \quad (3.9)$$

where β is the transfer cost per element and L is the communication startup cost.

As n grows very large, this asymptotically approaches

$$\text{Total Communication Cost} \approx \frac{\beta n^2}{2} p + Lp \quad \text{for } n \gg 1. \quad (3.10)$$

Therefore, the total running time can be obtained as

$$\text{Total Running Time} \approx \frac{n^3}{3p} \alpha + \left(\frac{\beta n^2}{2} + L \right) p \quad \text{for } n \gg 1. \quad (3.11)$$

As n grows the first term will govern the total running time ($n^3 \gg n^2$) we can see the asymptotic parallel efficiency of 1: Total running time $\rightarrow \frac{n^3}{3p} \alpha$, for $n \gg 1$.

In sum, parallel factorization with cyclic allocation scheme yields total cost as

$$\text{Total Running Time} \approx \frac{\alpha'}{p} + \beta' p \quad \text{for a moderate } n, \quad (3.12)$$

where $\alpha' = \frac{n^3}{3} \alpha$; $\beta' = (\frac{\beta n^2}{2} + L)$.

It should be also noted that for the parallelized Gaussian elimination algorithm utilizing cyclic allocation scheme, the second term of the total running time for a moderate n takes slightly different form as

$$\text{Parallelized Gaussian Elimination: } \beta' = (L + n^2 \beta). \quad (3.13)$$

This difference indicates that the parallelized factorization followed by the triangular system solving holds better efficiency than the parallelized Gaussian elimination method approximately by a factor of two, as confirmed from the cost comparison plot in figure 3.4.

As mentioned before, it is of importance to note that, regardless of which parallel factorization scheme is employed, simply increasing the total number of processors cannot guarantee the parallel efficiency as long as they rely on simple broadcasting strategy. Rather, it will increase the total running time linearly as p grows large by the second term of eq. (3.12).

3.6 Optimized Parallel Factorizations with “Super Linear” Speedup

A successful tuning of the parallel factorization is twofold to fit the essentials of the present problem: (1) banded nature and (2) augmentation by penalty method. The detailed pseudocode is available in appendix D.

On one hand, as in the serial version, skipping update tasks beyond the maximum bandwidth on each processor can significantly save the cost. As expected, a test simulation of the parallel factorization (system size $n=11328$; bandwidth=768) costs only 5.99 seconds (2.8% of 214.28 seconds without consideration of banded nature.)

On the other hand, the penalty method-augmented analysis flow remarkably affects the parallelization strategy as well as the system solving. In fact, the penalty method had been adopted mainly for the stability purpose, since sudden degradation of force resistance and brittle failure during experiments of RC structures are normal. The penalty method can be physically understood by addition of highly stiff penalty elements to the nodes, on which the actual external forces are imposed (i.e., numerically by adding very large term, $10^3 \times \max(\mathbf{K})$ herein, to the associated diagonal terms in the structural stiffness matrix.)

If a specific consideration is not paid, the two separate parallel factorizations would be done in the static and nonlinear analysis stage, which is obviously inefficient in light of the key characteristic of penalty method—only small portion of the matrix is changed by the penalty elements, since the number of the loaded nodes is generally very restricted in the actual experimental setup.

We denote the optimized method herein as “*partial*” pipelined parallel factorization method whereas the one without optimization as “*full*.” The underlying idea is to resume the second parallel factorization from the indispensable part, and it is practically realized by storing submatrix which is under influence of the penalty elements on each processor during the first factorization. This is why we denoted it “*partial*.” Furthermore, its efficiency can be maximized by prudent numbering of the nodes where the penalty elements are attached. By assigning as large equation numbers to the associated nodes as possible, we can reduce the required storage of the submatrix, and also minimize the total cost for the second parallel factorization.

Table 3.2. Total time cost comparison of full-/partial- parallel factorizations without/with prudent numbering [sec]

Full or Partial Factorization	Prudent numbering	a. 1 st	b. 2 nd	Total cost (a + b) (t*, s**)	
Full	X	72.889	72.096	144.985	(3240, 829)
Partial	X	72.168	21.348	93.516	(3240, 829)
Partial	O	72.075	0.020	72.095	(3240, 3205)

Note: (t*, s**)=(total nodes, smallest node number related to the penalty element)

To ensure the efficiency of the optimized factorization, comparison results are summarized in table 3.2. For a sample system (size = 9672) 104 total processors were used. The first row indicates the case where “*full*” factorizations were duplicated without prudent numbering. As expected, this case costs exactly twice the cost of one parallel factorization. The second row shows the case where “*partial*” factorization without prudent equation numbering was carried out, and the improvement in time cost of the second factorization is apparent. Although prudent numbering scheme is not yet used, the partial pipelined factorization scheme enables the second factorization to be completed in only 21 sec (30% of the first factorization.) The third row reveals the result of the case where “*partial*” factorization with prudent numbering was performed. It gives tremendously improved performance for the second factorization with the cost of 0.02 sec (0.03% of the first factorization). It should be noted, however, that such a prudent numbering should be carefully applied without increasing the bandwidth. Otherwise, this practical remedy will lose its efficiency.

It is of notable interest that the parallel pipelined factorization implemented herein appears to achieve “*super-linear*” speedup as confirmed by the cost results of parallel factorization shown in Figure 3.6. For such favorable behavior, one of the plausible reasons would be the well known “*cache effect*” considering the memory hierarchy of CPUs—Essentially, the major task in the pipelined algorithm herein involves a single vector manipulation, and the amount of data appears to decrease with total processors available and to better fit into the cache.

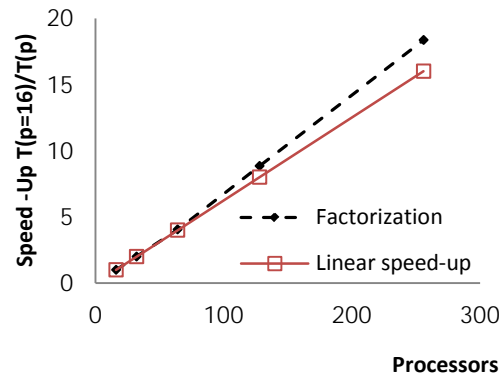


Figure 3.6. Super linear speedup attained from simulations of a test structure (system size $n = 32400$; bandwidth = 8145).

3.7 Parallel Triangular System Solving versus Parallel PCGM

After factorization, the solutions at all the remaining steps are obtained by solving triangular system in a parallel manner. In terms of parallel triangular system solving, a number of algorithms are available, e.g., simple broadcasting (Karniadakis and Kirby 2003) and pipelined scheme (Wilkinson and Allen 1999). Since the structure and performance of those methods are fairly similar for a moderate size system, a simple reduction scheme (Casanova et al. 2009) which is exploiting tree algorithm via “*MPI_Reduce*” has been optimized herein in such a way that column-based cyclic distribution and banded nature are well taken into account (see pseudocode provided in table 3.3). The line 2 and 3 is for the consideration of banded nature of the system. n_end (line 2) means the index of the last term within the bandwidth while r_end (line 3) indicates number of unknowns on each processor which must be updated. Especially the buffer s (line 4) is meaningful only on P_k since all t 's are summed up and sent to the buffer s on P_k by *MPI_Reduce* (line 7).

Table 3.3. Pseudocode of the optimized parallel algorithm for the upper triangular system, successfully exploiting column-based cyclic distribution and banded nature

Note: P_k = the processor holding unknown x_i ,	
Nband = Maximum bandwidth	
1:	For $i = n-1$ to 0
2:	$n_end = \min(n-1, i-Nband-1)$
3:	$r_end = \text{floor}(n_end / p)$
4:	$t = s = 0$
5:	forall $j \in (1, r_end]$
6:	$t = t + u_{i,j} \times x_j$
7:	<i>MPI_Reduce</i> ($t^{(send)}$, $s^{(recv)}$, 1, ..., <i>MPI_SUM</i> , P_k , ...)
8:	On P_k : $x_i = (b_i - s) / u_{i,i}$
9:	End

In order to bear out the advantage of the parallel strategy being proposed, we carried out some quantitative comparison with a representative, powerful parallel solver—parallel PCGM, which is widely accepted as one of the fastest and most reliable algorithms for positive definite and symmetric systems. Indeed, its parallel version can be easily realized due to clear parallelizable structure. As briefly described in table 3.4, the PCGM consists of just a few parallelizable procedures—namely, for α_k one matrix-vector multiplication and two inner products and for β_k one inner product, and these fall into embarrassingly parallelizable forms (denoted as summation in table 3.4). The only remaining task is the calculation of modified residual term $\tilde{\mathbf{r}}_{k+1}$ of which expense directly depends on the type of preconditioning. Fortunately, there exist some preconditioning methods such as “*diagonal scaling*” (also called Jacobi preconditioning with $\mathbf{M} = \text{diag}(k_{ii}), i \in [1, n]$), making the task for $\tilde{\mathbf{r}}_{k+1}$ embarrassingly parallelizable.

Table 3.4. Pseudocode of parallel PCGM for $\mathbf{K}\mathbf{x} = \mathbf{b}$

Note: p = total processors, and superscript (m) denotes local storage on processor P_m

Initialization: $\mathbf{r}_0 = \mathbf{b} - \mathbf{K}\mathbf{x}_0$; $\mathbf{c}_0 = \mathbf{M}^{-1}\mathbf{r}_0$; $\tilde{\mathbf{r}}_0 = \mathbf{c}_0$

For $k = 0$ to $\dim \mathbf{K} - 1$

$$\alpha_k = \frac{\tilde{\mathbf{r}}_k \cdot \mathbf{r}_k}{\mathbf{c}_k^T \mathbf{K} \mathbf{c}_k} = \frac{\sum_{m=0}^{p-1} \tilde{\mathbf{r}}_k^{(m)} \cdot \mathbf{r}_k^{(m)}}{\sum_{m=0}^{p-1} \mathbf{c}_k^{(m)T} \mathbf{K}^{(m)} \mathbf{c}_k^{(m)}} \rightarrow \mathbf{x}_{k+1} \text{ \& } \mathbf{r}_{k+1} \text{ such that}$$

$$\mathbf{x}_{k+1} = \sum_{m=0}^{p-1} (\mathbf{x}_k^{(m)} + \alpha_k \mathbf{c}_k^{(m)}), \quad \mathbf{r}_{k+1} = \sum_{m=0}^{p-1} (\mathbf{r}_k^{(m)} - \alpha_k \mathbf{K}^{(m)} \mathbf{c}_k^{(m)})$$

$\tilde{\mathbf{r}}_{k+1} = \mathbf{M}^{-1} \mathbf{r}_{k+1}$ - type of \mathbf{M} determines a proper parallel algorithm

(if the stopping criterion is met, exit)

$$\beta_k = \frac{\tilde{\mathbf{r}}_{k+1} \cdot \mathbf{r}_{k+1}}{\tilde{\mathbf{r}}_k \cdot \mathbf{r}_k} = \frac{\sum_{m=0}^{p-1} \tilde{\mathbf{r}}_{k+1}^{(m)} \cdot \mathbf{r}_{k+1}^{(m)}}{\sum_{m=0}^{p-1} \tilde{\mathbf{r}}_k^{(m)} \cdot \mathbf{r}_k^{(m)}} \rightarrow \mathbf{c}_{k+1} = \sum_{m=0}^{p-1} (\tilde{\mathbf{r}}_{k+1}^{(m)} + \beta_k \mathbf{c}_k^{(m)})$$

End

Table 3.5 shows total running time by parallel PCGM and parallel triangular system solving with increasing total processors. The cost of parallel factorization based on the pipelined scheme is also provided for a reference. Overall, the cost of parallel PCGM is too expensive to achieve superiority over parallel triangular system solving, although it clearly exhibits excellent scalability. Referring to table 3.5 if we have 64 processors, 100 iterations by the parallel triangular system solving would amount to 632 seconds, which is still smaller than one iteration cost of parallel PCGM, 766.018 seconds. Hence, provided that the solution converged within a relatively small number of iterations (this is generally guaranteed by the penalty method herein), this quantitative comparison bears out the practical superiority of the parallel system solving strategy proposed in this work.

Table 3.5. Cost of parallel PCGM, parallel factorization, and parallel triangular system solving in [sec] (system size $n = 32400$; bandwidth = 8145).

Total processors p	16	32	64	128	256
Parallel PCGM*	2904.6	1480.1	766.0	428.0	263.7
Parallel factorization**	2356.0	1177.5	581.9	266.3	128.3
Parallel triangular system solving	4.47	4.99	6.32	6.90	7.12

Note: * = with Jacobi preconditioning; ** = by pipelined algorithm

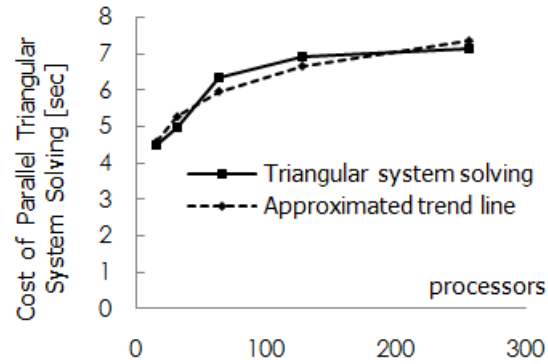
However, it should be noted that we were not able to achieve typical scalability in the parallel triangular system solving for a moderate size system, and this unfavorable behavior appeared to be found in most algorithms mentioned so far—in all numerical simulations by pipelined scheme, look-ahead, broadcasting, and reduction scheme. The total cost appeared to be gradually increasing with the number of total processors (figure 3.7a). This can be attributed to the fact that for a moderate size system the cost saved by parallel computation does not successfully surpass the communication overhead from increasing total processors. In order to expand on this problem, an approximated cost model of the parallel triangular system solving is proposed to take the form of

$$a \times \ln(p) + b, \quad (3.14)$$

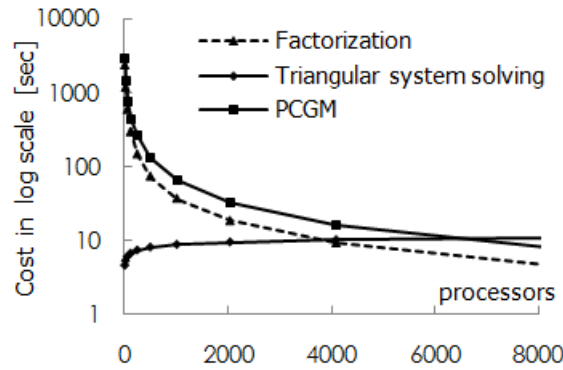
where p = number of total processors; a, b = constants.

This simple cost model results from intuitive understanding that the Taylor series of $\ln(p+1)$ is given by $p - p^2/2 + p^3/3 \dots$ and the typical cost of a parallel algorithm also takes a polynomial of p . In this sample simulation, an approximated cost model by eq. (3.14) reads $\ln p + 1.8$ (i.e., $a = 1.0$; $b = 1.8$), and it provides good agreement with actual cost up to 256 processors (see figure 3.7a). Plotting both approximated and actual running times reveals the marginal number of total

processors (figure 3.7b), at which the costs by the parallel triangular system solving and the parallel PCGM become equal, notably being far larger than the practical range of total processors (e.g., 600 processors available in this research). Even if the marginal number is reached, we should still count the additional cost for new tangent stiffness construction and redistribution, etc. Therefore, the superiority of the parallel triangular system solving over typical parallel solvers is still obvious, particularly in the present research.



(a) Cost for parallel triangular system solving and its approximated trend by a log function, obtained from simulations of a test system (size = 32400)



(b) Cost prediction of parallel PCGM and parallel triangular system solving

Figure 3.7. Cost comparison between parallel PCGM and parallel triangular system solving.

3.8 “Divide-and-Conquer” for Embarrassingly Parallelizable Procedures

When highly nonlinear material model is concerned, updating elements would behave as a significant bottleneck, e.g., overhead resulting from the micro-plane model in the parallel simulations by Danielson et al. (2008). Fortunately, a large portion of the program involving nonlinear element update is embarrassingly parallelizable: the numerical integration over global domain, handling nonlinear materials, and so on. One of the best and intuitively simple strategies handling such situations is the scheme so-called “*divide-and-conquer*,” in which a task is explicitly divided and carried out concurrently by the total processors available.

To more boost efficiency, the master-slaves concept is being employed. While master processor P_0 is dealing with all the global vector manipulations, slaves ($P_1 \sim P_{p-1}$) perform a part of global tasks associated with the assigned subdomain and hold only essential local data of the subdomains without overlapping (figure 3.8).

As briefly described in eq. (3.15), the parallel internal force update consists of a set of executions: first, a local internal force of the subdomain V_k , $k \in [1, p-1]$, is calculated on processors P_k and then passed to the master processor P_0 . Finally, the global summation is done on P_0 , and afterward P_0 calculates new unbalance force, determines convergence, and so on.

$$\mathbf{F}_{\text{internal}}^i = \sum_{k=1}^{p-1} \mathbf{F}_{\text{internal},k}^i = \sum_{k=1}^{p-1} \left(\int_{V_k} \mathbf{B}^T \boldsymbol{\sigma}_c^i dV_k + \int_{V_k} \mathbf{B}^T \boldsymbol{\sigma}_s^i dV_k \right) \quad (3.15)$$

where i = iteration step number; $\mathbf{F}_{\text{internal}}^i$ = global internal force vector on master node P_0 ; $\mathbf{F}_{\text{internal},k}^i$ = local internal force vector on processor P_k ; p = number of total processors; V_k = subdomain k on processor P_k ; \mathbf{B} = strain-displacement matrix; $\boldsymbol{\sigma}_c^i$ and $\boldsymbol{\sigma}_s^i$ = current concrete and steel stresses evaluated.

Special attention has been paid to the decomposition of perfectly bonded steels (realized by 3d truss elements herein) which might be shared by several subdomains. For steels lying on the boundary between subdomains, the processor with small id number is assumed to have the priority to hold those steels (e.g., a steel shared by subdomain 1 and 2 is assigned to subdomain 1). With these efforts, as shown in figure 3.9, the desired speedup in the construction of new internal force through nonlinear element update has been achieved, despite the inclusion of multidirectional smeared crack model and nonlinear steel material.

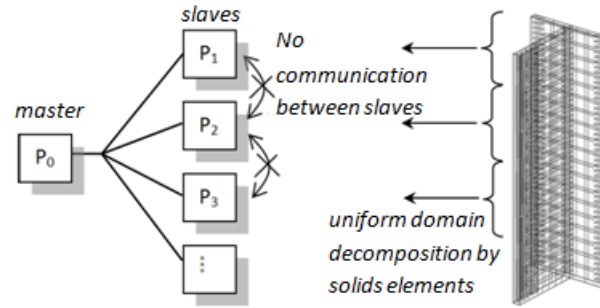


Figure 3.8. Master-slaves for all trivially parallelizable tasks along with nonoverlap uniform domain decomposition.

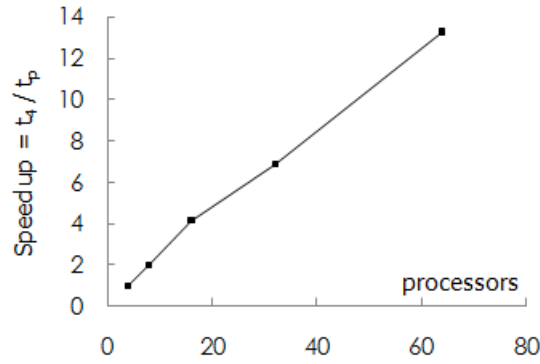


Figure 3.9. Speedup in nonlinear element updating procedure by “divide-and-conquer” strategy, attained from simulations of a test model consisting of 2784 concrete and 3372 steel bar elements.

For practical knowledge, we need to touch upon the effective data management in the parallelization. The key equation to be solved in most of the parallel explicit programs looks more or less like eq. (3.16) with the assumption of lumped mass on nodes (from Danielson and Namburu 1998).

$$\mathbf{M}\ddot{\mathbf{u}}^t = \mathbf{P}^t - \mathbf{F}^t \quad (3.16)$$

where \mathbf{M} = mass = $\text{diag}(m_{ii})$, $i \in [1, n]$; $\ddot{\mathbf{u}}^t$ = acceleration at time t ; \mathbf{P}^t = external force; \mathbf{F}^t = internal resistance force possibly including material/geometry nonlinearity.

Due to the lumped mass assumption, it is obvious that eq. (3.16) leads to an embarrassingly parallelizable situation resulting in only vector manipulations. In terms of a straightforward domain decomposition, various parallel tools have been developed and utilized: e.g., METIS and

its parallel version ParMETIS by Karypis and Kumar(1995a, 1995b) for weighted domain partitioning for the consideration of imbalance resulting from multiple-nonlinear materials; Domain distribution along heterogeneous processors (Sziveri and Topping 2000).

In general, such favorable conditions are not the case for implicit programs such as the one dealt with herein. As a successful remedy to the obstacle involving global data management, the column-based cyclic allocation is being exploited. As shown in figure 3.10, each column of the global stiffness matrix is cyclically distributed across all processors, as are the factorized triangular matrices (cf. row-based cyclic allocation performs almost equally). Indeed, the cyclic allocation scheme has been proved to balance the computation load very effectively (as an extreme case, if the system size is sufficiently large and stiffness is almost fully populated, the computation cost of each processor asymptotically converges to the same value). It should be stressed, however, that the block-based cyclic allocation is regarded to possess better performance, and thus it shall be a natural extension in the future.

Indexing problem naturally emerged from the cyclic data distribution, being far complicated than in serial version. To keep the portability and object-oriented nature of the parallel algorithms, one-to-one mapping function of the index would be a successful tool. In the present platform, an overloaded operator $()$ developed serves as the function, in which a global term $a(i, j)$ with global indexes $i, j \in [0, n-1]$ exactly indicates the corresponding term \tilde{a}_{IJ} in the compact storage where $I \in [0, 2b-1]$, $b = \text{band width}$, $J \in [0, r-1]$, $r = n/p = \text{number of columns per processor}$.

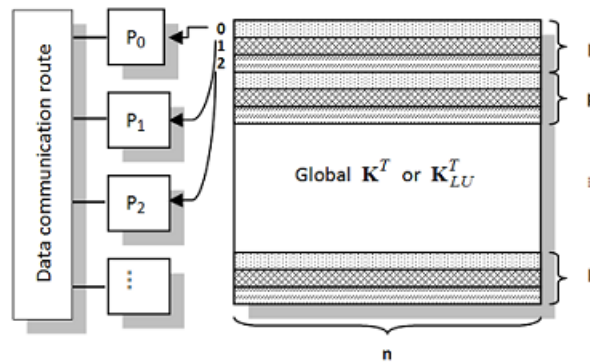


Figure 3.10. Column-based cyclic allocation on all processors for factorization and solving.

It should be noted that such a cyclic data distribution scheme is applied to the global matrix. All other data associated with subdomain are accordingly distributed over the slave processors available. In this sense, the present platform harmoniously exploits the uniform distribution of domain data and cyclic scattering of global matrix data, so as to boost the efficiency of the parallel performance.

3.9 *Issues on Load Balance and Error from Parallelization*

In problems involving a discrete crack or a propagating crack, extreme stress concentration emerging at the crack tip naturally necessitates the refined or biased meshing around the zone. Moreover, a multitude of nonlinear problems, e.g., continuum mechanics with plasticity theories or study of dynamic contact, requires local level iterations (sometimes in a large number of steps), to attain the converged state values. All of those situations are most likely to cause load imbalance among processors, requiring prudent domain decomposition along processors.

However, none of those difficult situations arises in the present problem of interest. The smeared crack model used is essentially linked to the total strain (cf. the decomposed strain which is common in classical plasticity theories and rotating crack models), and is evaluating current state values directly from microphysically defined local spaces—namely, the space of three orthogonal crack planes or particle-indentation couple for nonlinear shear. Furthermore, damage is considered to be distributed throughout the domain, and mesh refinement at a specific zone such as a crack tip is generally unnecessary during entire analysis. Consequently, work load on each processor is readily well balanced with the uniformly decomposed domain, mainly with respect to solid elements.

Based on the distinct characteristics of the present analysis platform, i.e., local iterations-free material models and total strain-based smeared crack, the errors which might arise from parallelization appear to be negligible. Indeed, a test simulation with a simple system of 40 concrete elements and 30 perfectly bonded steel bars was conducted up to severely damaged states, involving crushing and steel yielding under cyclic loading. Results revealed that the mean square errors (against 1 CPU case) from the analysis by 8 CPUs and 16 CPUs were $2.0\text{e-}16$ and $2.04\text{e-}14$ respectively, whereas ~ 0 with 4 and 6 CPUs.

It is noteworthy that if any of further complicated problems is to be tackled in the future extension, there should be pertinent consideration of dynamic load balance and domain decomposition techniques as well as error management in parallel processing, which fortunately have been well-established and available in the literature.

3.10 Physical Mechanisms and Randomness Fed by Parallelization

The implicit nonlinear FEA platform in its parallel version developed herein sparked our imagination to incorporate highly sophisticated physical mechanisms to tackle degradation phenomena. We shall touch upon some salient concepts only, and for the complete description and formulation one is referred to the corresponding sections in this thesis.

For degrading behavior of the concrete under cyclic loading, so-called multidirectional smeared crack model has been adopted—comparable with the key concept by Vecchio and Collins (1986); Selby and Vecchio (1993, 1997). For compression regime, as shown in figure 3.11(a), the Thorenfeldt concrete model (1987) has been employed to describe compressive stress in each crack direction—possibly three orthogonal crack surfaces can be initiated at the present framework as depicted in figure 3.11b (top). And generalization of the compression model has been conducted by incorporating un/reloading responses (Taucer et al. 1991) and nonlinear tension softening regime by Reinhardt (1984) as shown in figure 3.11(a-b). In all numerical simulations presented here, the softening parameter c is set 0.31 for smooth postpeak softening. To embrace the realistic nature of open crack, the present smeared crack model is obeying the notion of “*fixed*” type crack (as opposed to the “*rotating*” crack model). As well pointed out by many (e.g., Crisfield and Wills 1989), the fixed-type smeared crack model has the problem of spurious large stress transfer across crack surfaces when subjected to nonproportional loading. As illustrated in figure 3.11(c), to alleviate this pathological nature mainly with a physically plausible remedy, 3d interlocking mechanism has been proposed. And random particles used in the mechanism were generated from Gaussian distribution, in accordance with major trends in tribology (e.g., Jackson and Green 2005). At each step, active contacting areas of hemisphere-indentation couple yield the tangent shear stiffness—comparable to the Walraven’s 2D interlocking model (Walraven 1994). By virtue of the parallel platform, the random distribution of ideal particles in an unstructured manner over any real-scale structures of interest was made possible.

For reinforcing bar, an integrated model has been proposed by the authors: mainly based on the well-known Menegotto and Pinto (1973) steel model for smooth transition, initiation of compressive buckling by Dhakal and Maekawa (2002), and the strain parameter concept for early buckling in positive strain regime (Rodriguez et al. 1999). With the parallel platform, the topological transition, defined by the loss of surrounding element due to crushing or spalling, is being queried at each step so as to realistically lengthen the compressive buckling length of bar, whereas it is simply assumed constant during analysis in most existing research.

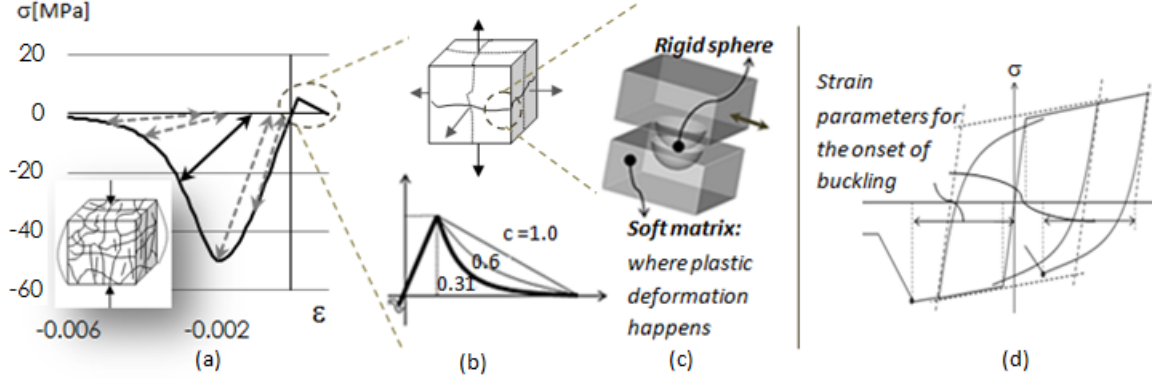


Figure 3.11. (a) Thorenfeldt compressive model generalized by un/reloading model; (b) tension softening regime defined on three orthogonal crack surfaces; (c) the fabric of rigid hemisphere-soft indentation proposed by the authors for nonlinear shear across opened crack; (d) Reinforcing steel bar model incorporating compressive buckling.

3.11 Concluding Remarks about Parallelization Strategies

As demonstrated so far, parallelization appears essentially to be problem-dependent, and how well embracing the key features of the problem under consideration determines the ultimate parallel efficiency. In the quantitative comparison among representative parallel strategies, particularly in terms of factorization, some practical knowledge had been attained: (1) the performance of “*broadcasting*” strategy tends to deteriorate beyond a certain range of total processors; (2) contrary to anticipation, the most advanced “*look-ahead*” strategy appears to exhibit poor performance with a small number of processors; (3) only the “*pipelined*” strategy reveals overall stable performance. Then, optimization of the pipelined factorization has been carried out, successfully taking advantage of penalty method and banded nature. Since the penalty method imparts remarkable smoothness to the global response, the parallel triangular system solving was able to achieve practical superiority over advanced parallel solvers such as parallel PCGM, as confirmed by quantitative comparison.

The implemented “*divide-and-conquer*” approach for all other embarrassingly parallelizable tasks is performing favorably on the master-slaves concept after nonoverlap uniform domain decomposition. Especially for a moderate size RC structure, the master-slaves approach enables nonlinear element update to be done without any intercommunication between slave processors, leading to clear scalability. By this successful parallelization of nonlinear element update procedure, the developed parallel platform was able to be imbued with a multitude of physical mechanisms to describe progressive and localized damage phenomena at the entire system level. It should be stressed, however, that the platform shall successfully harmonize with reliable parallel libraries, e.g., parallel sparse matrix solver and dynamic load balance scheme, in future research to achieve the general applicability.

By filling the gap between the microscopic physics and global degradation with localization, the parallel platform offers the unprecedented access to physics-based mechanisms (e.g., multidirectional smeared crack model, 3d interlocking model, and nonlinear steel with evolving buckling length) and even to the probabilistic randomness at entire system level. Indeed, random distribution of crucial mechanical parameter (i.e., interlocking particle size herein) across entire domain appears to be essential for the irrecoverable localization, as shall be addressed in later applications. Equipped with accuracy, stability and scalability, the implicit nonlinear FEA program in its parallel version is believed to serve as a fertile ground for the introducing of further physical mechanisms into various research fields as well as the earthquake engineering community.

Chapter 4 APPLICATIONS TO REAL-SCALE STRUCTURES

To some extent, it is fascinating to apply the parallel program to the simulation of real-scale structures with sufficient degree of complexity of both geometry and nonlinear behavior, since the analysis platform is essentially based on physical mechanisms and randomness over entire domain. Interestingly, the applications imply two poles: the one pole is the “*bottom-up*” formulation for degrading material at microscopic level while the other pole is the “*top-down*” validation of the simulation platform against large-scaled structures which is as big as state-of-the-art experimental facility allows.

On the other hand, investigation of the predicted behavior of the real-scale structure is believed to provide clear causal pathway between the microscopic mechanisms and the particular global response, due primarily to the existence of the persistently preserved physical counterparts. At the same time, a great deal of interesting knowledge might result from the fact that the entire domain is impregnated with randomness of the decisive material properties.

Hence, the act of validation of the platform would to be virtual experiments of actual structures of interest, rather than the conventional act of so-called “*fitting*” process for a number of key parameters required for the idealized governing models. Indeed, such virtual experiments might be thought of as a good realization of the “*third culture*” of science (the notion well pointed out by Kelly, 1998) in our field.

The virtual experiments conducted herein consist of two complicated real-scale shear wall systems—H-shaped wall and 4-story T-shaped wall system both under cyclic loading, as shall be provided in detail in following sections.

4.1 *H-Shaped Wall System under Cyclic Loading*

To validate the developed program, an experiment of real-scale RC structure exhibiting sufficient complexity of both geometry and nonlinear behavior had been selected: Model DP1, three-dimensional H-shaped wall system under cyclic loading conducted by Palermo and Vecchio (2002).

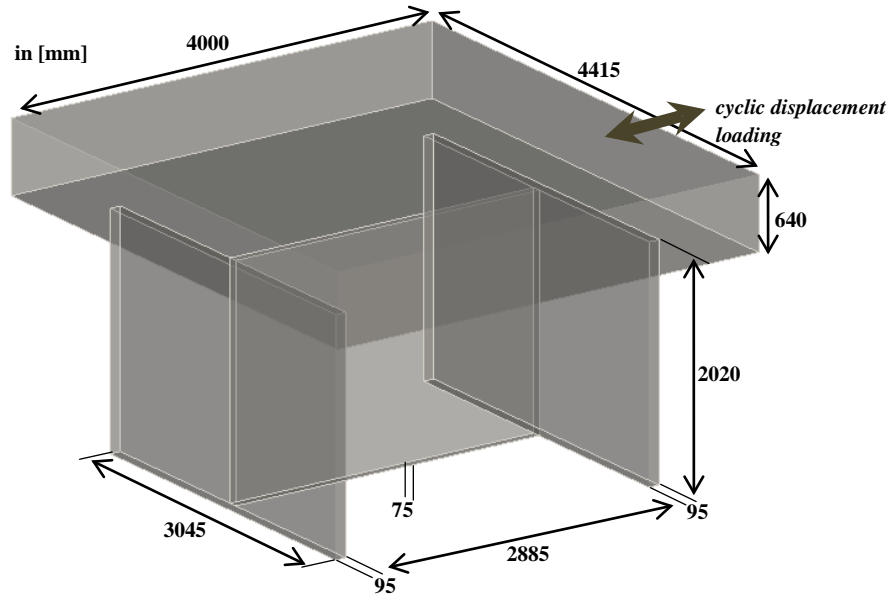


Figure 4.1. H-shaped wall system (DP1) details.

Figure 4.1 shows the dimensional details of DP1, and figure 4.2 gives reinforcement layout. Table 4.1 and table 4.2 present the material properties used in experimental program and simulation. In both web and flange, the concrete strength is 21.7 MPa and the strain at the peak is 0.00204. To realize uniformly distributed displacement loading and to enforce the nonlinear behavior to be fully absorbed in the H-shaped wall parts only, top slab is modeled by elastic material with artificially high stiffness, and bottom slab by firmly fixed boundary condition.

All the reinforcing bars are explicitly modeled by space truss elements which are assumed to be perfectly bonded to the surrounding solid elements. All bars are D6 type with 7 mm diameter, and the yielding stress and the corresponding strain are 605 MPa and 0.00318 respectively. The finite element model consists of 7784 solid elements and 11212 nodes, giving the total equation number of 32400 with bandwidth of 8145.

It is noteworthy that such “*perfectly bonded*” steel bars are intentionally adopted since this particular experimental program has no horizontal stirrups/hoops. Instead, only longitudinal bars in both vertical and horizontal directions are deployed, as seen in the reinforcement layout (figure 4.2). Therefore, we did not use the “*smart*” longitudinal bar model, which incorporates compressive buckling effect based on the topological transition.

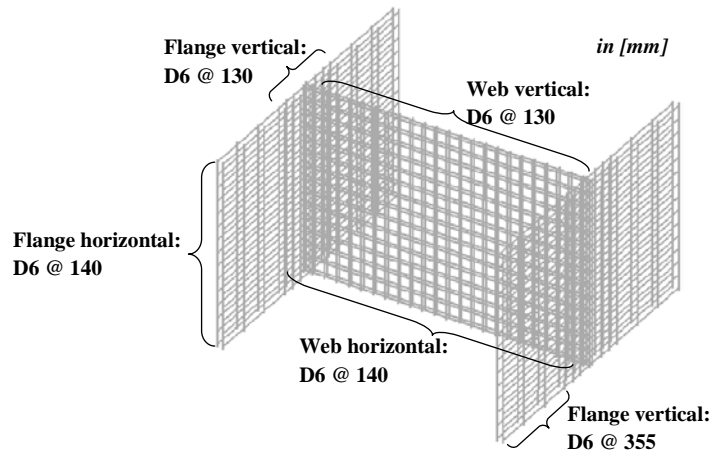


Figure 4.2. Reinforcement layout for H-shaped wall system (DP1).

Table 4.1. Concrete material property (DP1)

Zone	(ϵ'_c, f'_c)
Web & Flange wall:	(0.00204, 21.7 MPa)
Top slab:	(0.00193, 43.9 MPa)
Bottom slab:	(0.00166, 34.7 MPa)

Table 4.2. Steel material property (DP1)

Zone	Type	Diameter [mm]	ϵ_y	f_y [MPa]	f_{su} [MPa]
------	------	---------------	--------------	-------------	----------------

Web & Flange wall:	D6	7	0.00318	605	652
Top & Bottom slab:	No. 30	29.9	0.00251	550	696

To successfully utilize the 3d interlocking model for this particular experiment, ideal particles were generated from the Gaussian distribution, for which the mean of particle size was set 19 mm and the size ranges [0.1 mm, 38 mm], i.e., size values out of the range are excluded without significant loss of generality. Then, they were randomly distributed over the entire domain as depicted in figure 4.3. For visualization purpose, one particle is plotted at each element center whereas each integration point actually holds one particle in the analysis.

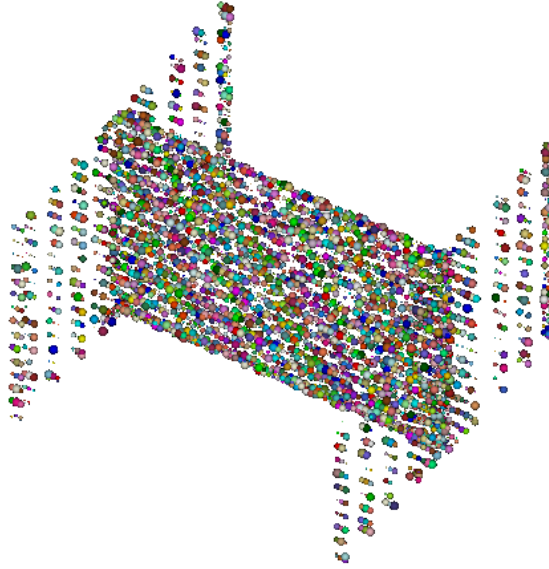


Figure 4.3. Unstructured random distribution of ideal particles over entire H-shaped RC wall system; the random particles are intended to realize the irregular asperity configuration, not the actual aggregate sizes.

The displacement history applied to DP1 is shown in figure 4.4. The history is defined identical to that acquired from actual experimental response.

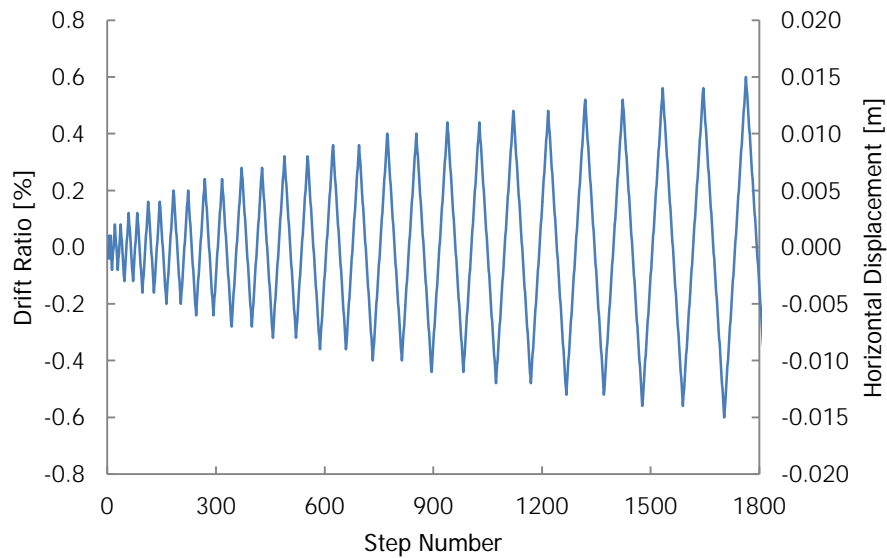


Figure 4.4. Applied displacement history to DP1 (by courtesy of D. Palermo and F. J. Vecchio).

According to experiment report, severe diagonal cracks emerged throughout the web part from the very early loading stage, and eventually compressive crushing takes place at the regions where diagonal cracks intersect. Contrarily, it is reported that the flange part exhibits U-shaped cracking combined with flexural cracking (figure 4.5). Ultimately, as the displacement loading proceeds beyond the point near 11~12 mm, significant damage on the web part appears to lead to emergence of localized sliding shear plane, interestingly running in vertical direction and parallel to each other as shown in figure 4.6.

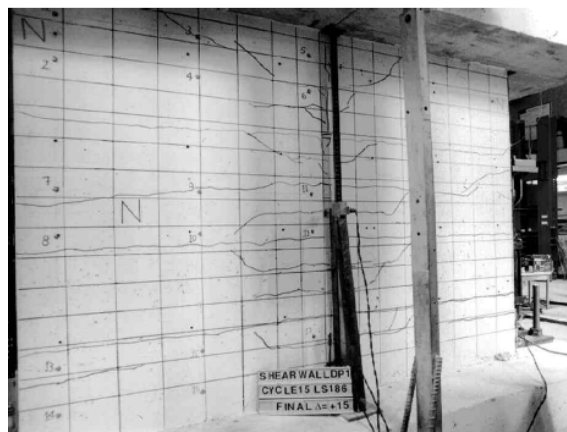


Figure 4.5. Ultimate damage on flange part showing U-shaped and flexural cracking (Palermo and Vecchio 2002, with permission from ACI publishing).

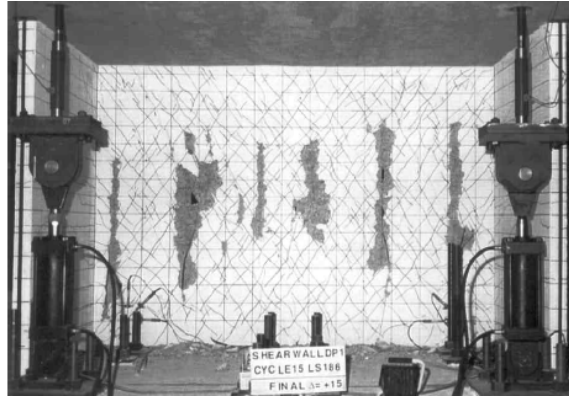


Figure 4.6. Ultimate damage on web part exhibiting distributed diagonal cracks and localized sliding planes with vertical directivity (Palermo and Vecchio 2002, with permission from ACI Publishing).

According to figure 4.7(a), without the 3d interlocking model, the multidirectional smeared crack model exhibits over-stiff responses as expected, which indeed confirms the pathological nature of the “*fixed-type*” smeared crack model. Although the smeared crack model is well equipped with reliable microscopic stress functions—namely, nonlinear tension softening model and postpeak softening regime in the compression model, the overall prediction reveals that the smeared crack model without the interlocking mechanism is incapable of accurately capturing load-carrying capacity of the structure under excessive cyclic loading. The plausible rationale to this is that, in the absence of the interlocking mechanism, the applied cyclic loading caused the development of large shear strain around the crack surfaces, and eventually led to hardening response which appears to gradually increase (figure 4.7a).

Contrariwise, figure 4.7(b) asserts that the contribution of the 3d interlocking mechanism to the smeared crack model is remarkably significant. Additional degradation of shear resistance resulting from the interlocking mechanism is playing an essential role in reducing shear transfer around the opened crack surfaces. Moreover, hardening behavior beyond peak point (i.e., displacement loading greater than ± 8 mm) is considerably alleviated by the interlocking model, showing successful agreement with experimental response.

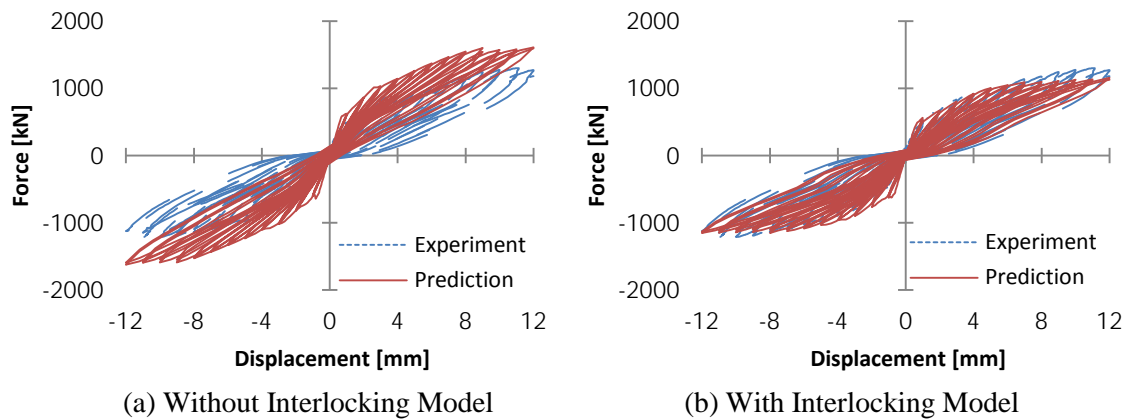


Figure 4.7. Effect of 3d interlocking model on the global force-displacement responses (simulated up to 12 mm near the peak load-carrying capacity).

According to the predicted deformation shown in figure 4.8(a), the damage appears to be well distributed along the entire domain, primarily due to the absence of the 3d interlocking model. Indeed, damage induced by the smeared cracking is so smoothly scattered along the wall system that it rarely leads to any noticeable formation of the localized damage. By introducing 3d interlocking model, however, the numerical simulation allows the development of noticeable localized damage, notably in a form of out-of-plane bulging with vertical directivity on the web part as marked by dashed line in figure 4.8(b).

It is of great interest to notice that such a localized damage on the web (notably, without some post-processing) is predicted even with vertical directivity, which is in agreement with the actual failure mode of the experimental program (cf. figure 4.6). The random distribution of ideal particles, originally introduced for the 3d interlocking model, over the entire domain is believed to be essential to reproduce such a localized damage rather than a smoothly distributed one. Indeed, it has been reported that the randomness of domain, e.g., heterogeneity of granular medium, appears to possess strong correlation with the emergence of localized failure modes of structure (e.g., Shahinpoor 1980 and Andrade et al. 2007).

In fact, this localized damage with vertical directivity is one of the unique features of this experimental program while typical localized damage on shear wall system is normally expected to exhibit diagonal directivity. It might be attributed to several facts of this particular experimental program—relatively thin web thickness, coarse reinforcing on the web, excessively wide flanges and so on. From the structural perspective, wide flange might cause stiff resistance in vertical direction near the web-flange connection part. This appears to cause the unique damage mode of the web, which is already weakened by diagonal cracks intersecting each other, and finally to form vertical slip planes.

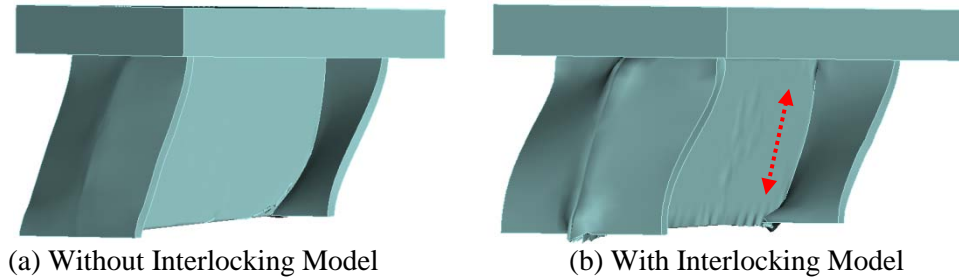


Figure 4.8. Deformed shape (amplified) with/without 3d interlocking model (Note: by introducing the 3d interlocking mechanism, the localized damage with vertical directivity marked in dashed arrow can be captured).

On the other hand, it is of practical importance to note that the three-dimensional contribution of the flanges is not ignorable. Although the out-of-plane stiffness of the flange parts is relatively small compared to the web, complicated deformation of the flanges asserts the strong necessity of the detailed three-dimensional analysis of the flanges, see figure 4.8(b). According to the experimental results, complicated deformation of the flange appears to be tied to the U-shaped cracking which would have not been understood by use of the “*flexural*” crack concept.

In terms of associated parallel efficiency, the parallel factorization reveals favorable scalability as shown in figure 4.9. We can also confirm from figure 4.9 that the intensive nonlinear element update was performed with a desired parallel efficiency. Such clear scalability found in the nonlinear element update procedure has significant meaning for applicability of the present parallel platform. Regardless of the complexity and kind of the nonlinear material models, the intensive computational procedure associated with the material is bounded within a part of NR-iteration, and thus, can be easily implemented into the program in the future. Furthermore, the parallelization effectively minimizes the expensive cost which might arise by the complexity of the material model.

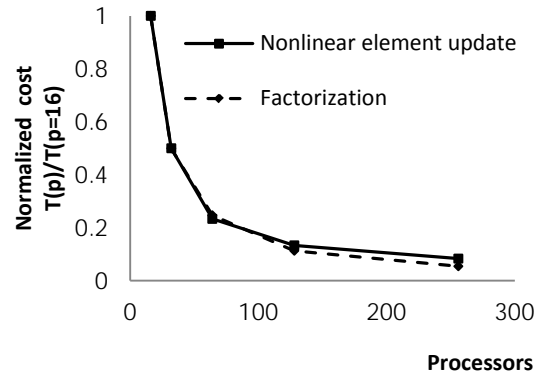


Figure 4.9. Cost plot of factorization and nonlinear element update after normalization by the cost for $p = 16$.

Influence of Consumed Energy-Based Damage Model

In the preceding section, we ascertained the desired accuracy of the advanced smeared crack model, localized failure modes being accessible by the intrinsic randomness of the 3d interlocking model, and even successful parallel efficiency.

It should be stressed, however, that it is still intractable to predict abrupt softening behavior of the structure during excessive cyclic loading excursions. Such a sudden loss of resistance appeared to be strongly related to rapid development of localized damage zone, e.g., in a form of vertical sliding shear plane in the present case DP1, or of localized shear band in other general cases. This phenomenon naturally necessitates further physical mechanisms.

In this context, we had proposed a novel damage model in the previous section 2.4, which is physically rooted in the consumed energy, especially more pertaining to the compression or cyclic/seismic loading rather than simple Mode-I cracking. As reflected in figure 4.10(b), the inclusion of the consumed energy-based damage model proposed in this study appears to be of capital influence on the capability of reproducing the “*sudden*” postpeak softening response. In the absence of the damage model, the postpeak response is predicted as a smooth softening behavior with almost linear degradation trend (figure 4.10a) whereas, in the presence of the damage model, the noticeably abrupt softening behavior is captured (figure 4.10b).

It is noteworthy that even with this damage model the total resistance of the system tends to approach the seemingly lower limit, and afterwards no apparent softening behavior is observed, i.e., in the ranges beyond ± 10 mm (figure 4.10b). This lower limit, a sort of residual resistance, appears to be tied to the reinforcing steels which are assumed to be “*perfectly bonded*” to the solids elements. In detail, even after the solids materials lose their mechanical strength, although being realistically captured by the damage model, the perfectly bonded nature of steel still continues to share the nodal deformation with the weakened solid elements, leading to a certain level of residual strength. Thus, unless further physical degradation mechanisms are additionally introduced (e.g., rapid compressive buckling, tensile rupture, plastic regime with very small hardening ratio $\ll 1$, or most important, partial/full detachment of steel from surrounding solid elements), the analysis would keep generating such residual resistances. Naturally, those supplementary remedies should be implemented in the future research.

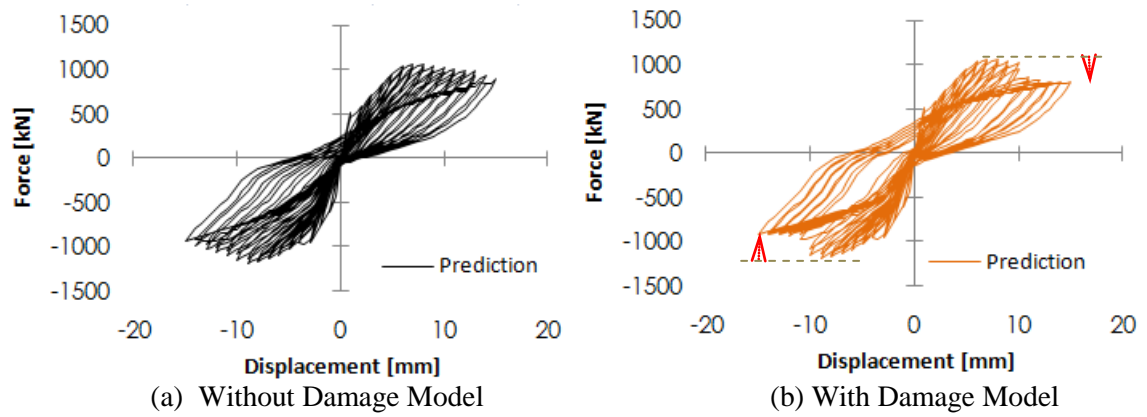


Figure 4.10. Influence of damage model on the rapid postpeak softening response (both simulations includes 3d interlocking model, run up to 15 mm).

4.2 4-story T-Shaped Wall System under Cyclic Loading

To demonstrate the capability of the parallel platform for more complicated real-scale structure exposed to cyclic loading, we had selected the well-documented experiment of 4-story T-shaped wall system (Thomsen and Wallace 1995, 2004). The wall system was loaded by cyclic displacement up to its ultimate damage states—namely, fully developed diagonal cracks, and crushing and spalling of concrete accompanied by compressive buckling of longitudinal reinforcing bars.

The experimental program, denoted by TW2 hereafter, is approximately one-quarter scale of a part of the original prototype building, similar to a typical multistory office structure in the high seismicity zone such as Los Angeles. The detailed geometric information is given in figure 4.11 and reinforcing bar details in figure 4.12. TW2 is 3.66 m (12 ft) tall and 102 mm (4 in.) thick, and the length of both web and flange is 1.22 m (4 ft). Stiff floor is placed at 914 mm (3 ft) interval and modeled by highly stiff elastic solids to exclude its structural effect on the global degradation in the simulation. Table 4.3 and 4.4 provide material properties of concrete and reinforcing bars used in the numerical simulations.

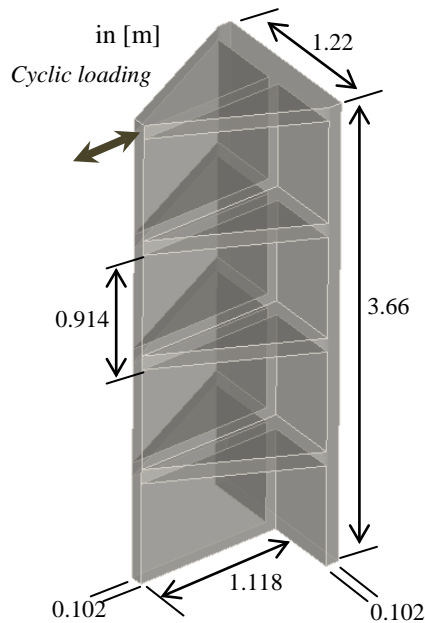


Figure 4.11. Overall geometry of TW2.

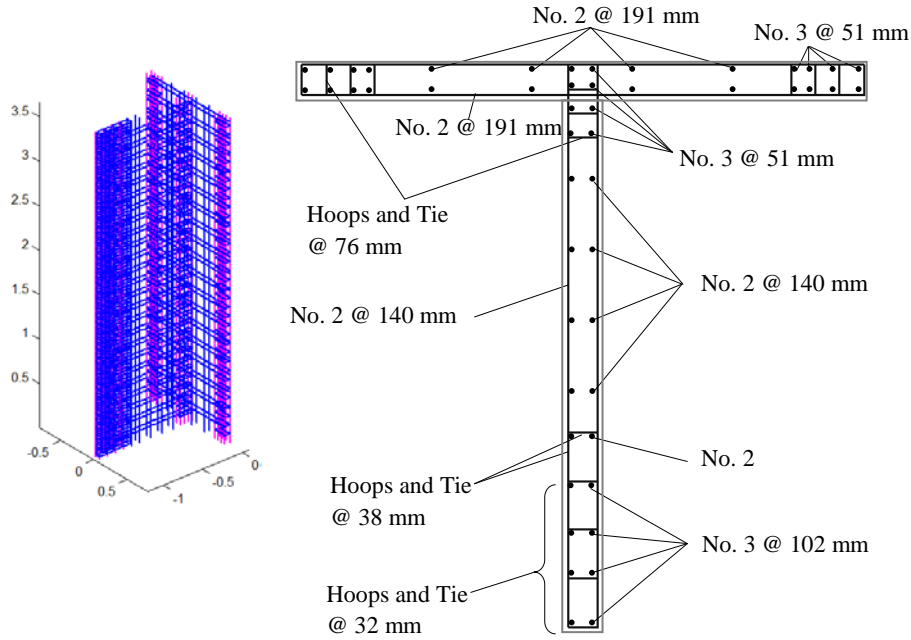


Figure 4.12. Reinforcing bar details with all cover concrete thickness 19 mm.

Table 4.3. Concrete material property (TW2)

Property	Values used in simulation
$(\epsilon'_c, f'_c)^*$	(0.002, 41.7 MPa)
f'_t^{**}	5.63 MPa
Softening parameter c	0.31

Note: * from the mean value of samples taken at the time of test

** approximately 13.5% of f'_c attained from beam rupture tests

Table 4.4. Steel material property (TW2)

Description	Type	Area [mm ²]	ε_y	f_y [MPa]
Longitudinal steel	Grade 60 No. 3	71	0.00207	414
Longitudinal steel	No. 2	32	0.00207	414
Hoop and Tie	D = 4.75 mm	18	0.00207	414

By virtue of the parallel platform, all the structural parts are explicitly modeled for the numerical simulation. In total, 67410 linear hexahedral elements for concrete and 20646 space truss elements for all reinforcing bars are used to realize the complete geometry as much detail as possible. Thus, 84211 nodes are generated, and resulting equation number amounts to 251838 with the maximum bandwidth 4038. It should be stressed that, in this manner, no artificial separation between cover and core concrete, which is normal in popular fiber section models, has been included, since all horizontal hoops and crossing ties are explicitly modeled, and thus play in concert to produce their actual resistance at each loading step. The displacement history applied to TW2 is given in figure 4.13. The history is defined identical to that acquired from the actual experimental records (by courtesy of Professor J. W. Wallace).

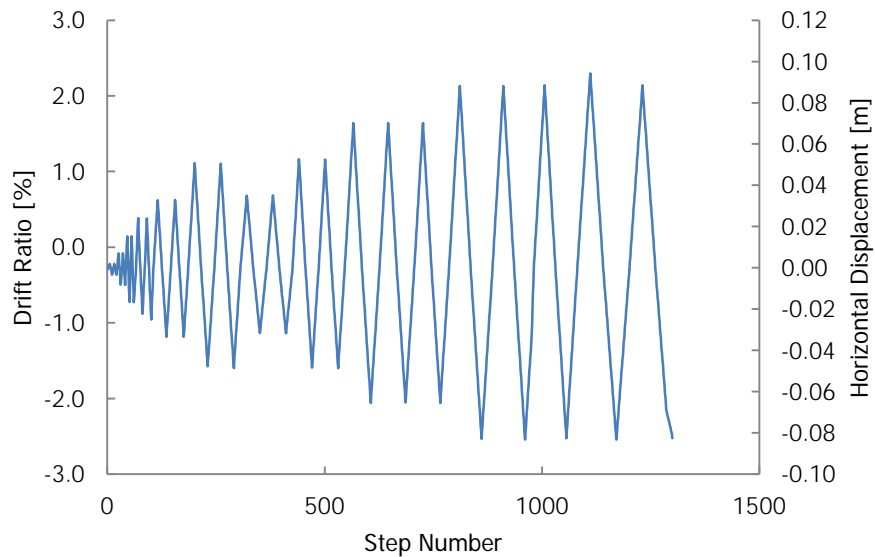


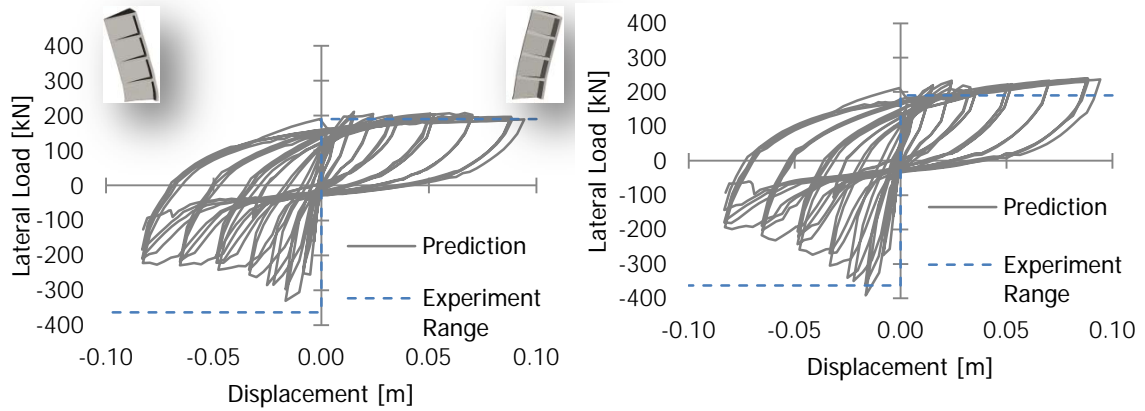
Figure 4.13. Applied displacement history (TW2).

As desired, the remarkable contribution of 3d interlocking model to resolving the pathological nature of “*fixed-type*” smeared crack model, i.e., over-stiff prediction, has been revealed from the simulation of TW2. Figure 4.14 compares the resultant force-displacement plots from predictions with/without 3d interlocking model. For comparison, the upper and lower limits of the recorded force range from the experiment are given by the dashed lines in both figure 4.14(a) and (b). Overall, the 3d interlocking model appears to successfully coordinate with the fixed-type smeared crack model in the simulation. The range of load-carrying capacity of the system is well captured as shown in figure 4.14(a). Contrarily, without 3d interlocking mode, the over-stiff nature of the smeared crack model is clearly visible (figure 4.14b).

Such over-estimated response is more apparent in the positive displacement loading range (i.e., flange under compression) than in the negative range (i.e., flange under tension). In the case of the flange under compression, with the asymmetric placement of wide flange, large portion of the bottom web undergoes tension and shear-governed deformation. This can be restated in more practical terms such that the so-called “*neutral axis*” of bottom section is located at near the wide flange, causing web under tension and flange under compression (Thomsen IV and Wallace 2004). Therefore, the interlocking mechanism, which always manifests itself in the presence of actively opened cracks, influences significantly on the global resistance when the flange under compression—i.e., positive displacement loading regime in figure 4.14.

On the other hand, when the flange is under tension (negative displacement range), both predictions with and without 3d interlocking model appear to commonly underestimate the load-carrying capacity of the system than that from experiment—see figure 4.14(a) and (b). This can be attributed to the fact that we intentionally excluded lateral confinement consideration from the microscopic compression model in the simulation, mainly to investigate the influence of the 3d interlocking model on the global prediction. Although all the lateral reinforcing bars had been explicitly modeled in the simulations, the compressive stress is fundamentally updated from the microscopic compressive stress function defined on three crack surfaces in the multidirectional smeared crack framework. In particular, relatively large compressive strain can develop in large portion of the web due to the wide width of the flange. Hence, the present stress function commonly tends to produce relatively weak compressive stress according to the excessively large compressive strain.

Thus, it would be a natural extension in future research to incorporate appropriate physical mechanisms in order to describe the lateral confinement effect in the multidirectional smeared crack model framework.



(a) With 3d Interlocking Model

(b) Without 3d Interlocking Model

Figure 4.14. Effect of 3d interlocking model on global force-displacement response; Negative displacement corresponds to the case of flange under tension while the positive range signifies flange under compression, as depicted in insets.

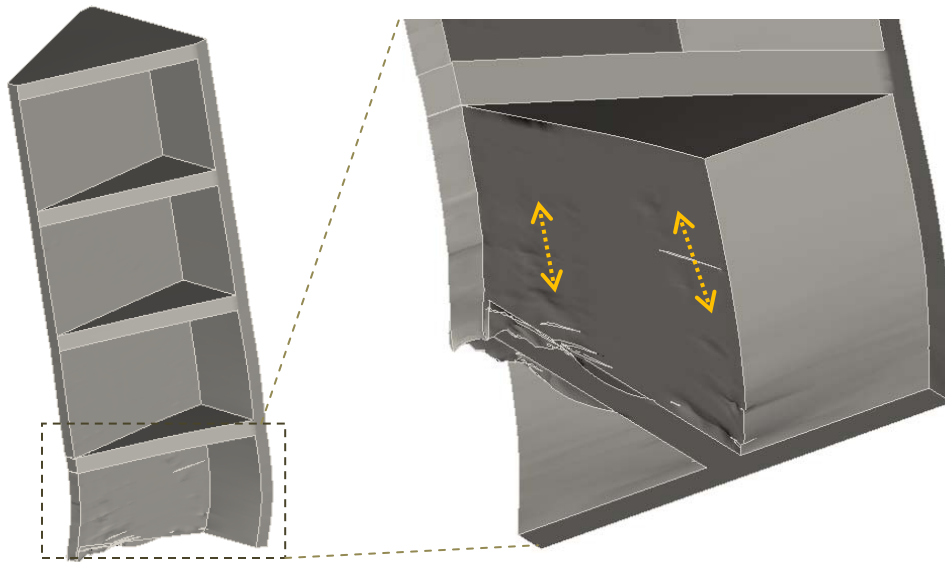


Figure 4.15. Deformed shape (amplified) at the last step of the simulation, revealing concentrated severe damage at boundary part of web and localized damage with diagonal directivity (marked by dashed arrows) by virtue of 3d interlocking model.

As shown in figure 4.15, the irrecoverable damage has been captured, notably in a localized manner. Emphasized by dashed arrow in the figure, the damage is concentrated at web part and

apparent diagonal directivity can be easily detected without the need of other post-processing. Intrinsic randomness of particles in 3d interlocking model is believed to hold strong influence on such a localized damage of the web. Compressive crushing at the web-toe is also well predicted and shown in a somewhat exaggerated manner.

As shown in figure 4.16, topological information involving the longitudinal steel bars and surrounding solid elements is systematically dealt with and updated at each analysis step, so as to ascertain topological transition and associated degradation of bars. Such mechanisms include the onset of compressive buckling of longitudinal steel bars induced by abrupt change in boundary conditions due to the spalling or crushing of surrounding elements as described in section 2.7.

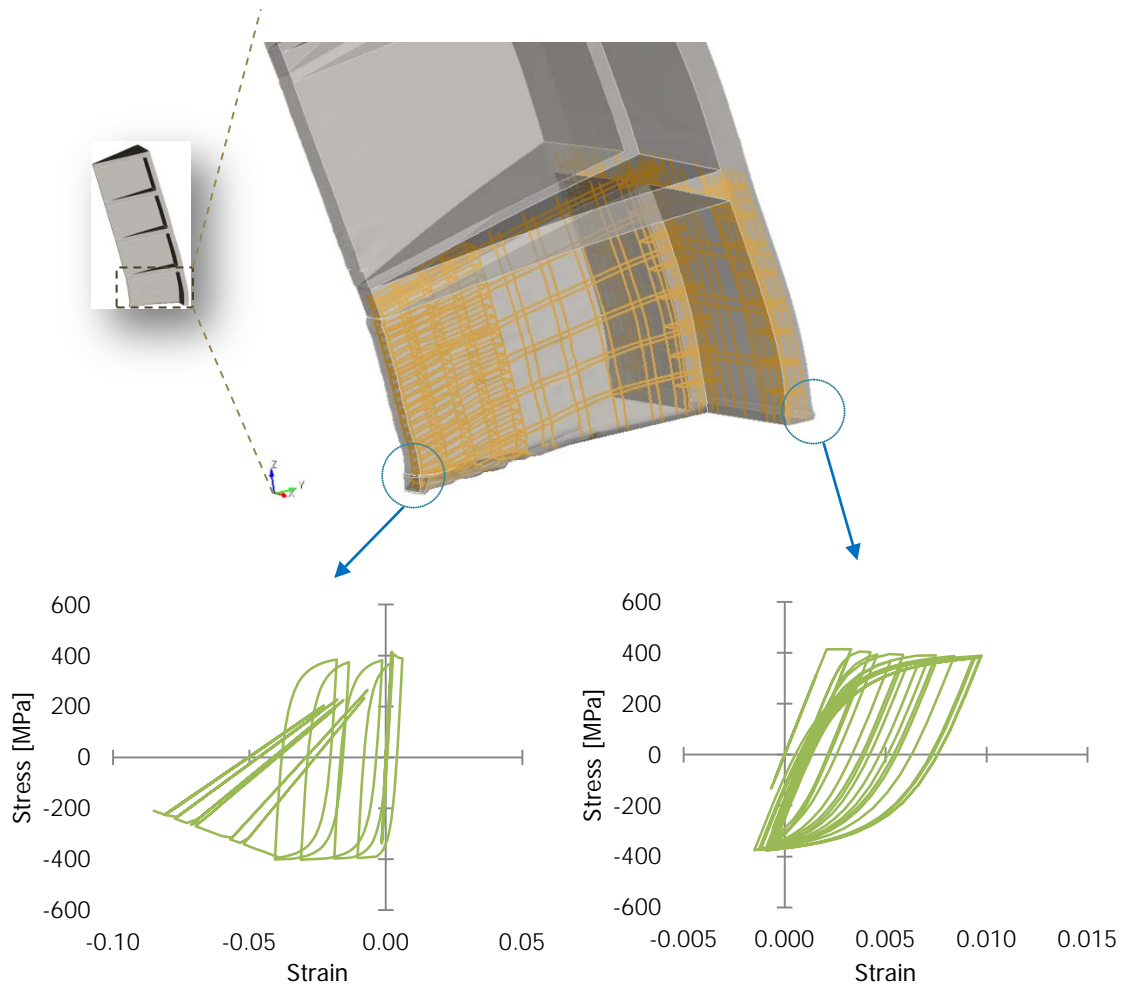


Figure 4.16. Contrast of stress-strain responses from longitudinal steel bars depending on the locations: the outermost positions of web toe (left) and of flange (right); Superimposed plot of deformed steel bars at bottom floor only (top).

Figure 4.16 reveals the significant effect of compressive buckling on the nonlinear behavior of longitudinal steels. It is apparent that longitudinal steel placed at the outermost position of web toe is experiencing compressive buckling according to the excessively large compressive strain as shown in figure 4.16(left). Contrarily, the longitudinal steel at the flange shows no buckling phenomenon, but typical stress-strain response with smooth transition after yielding is identified, with relatively small strain range (<0.01).

Figure 4.17 shows evolving compressive buckling length of a longitudinal steel at the outermost position of web toe (left), abruptly lengthened from 0.02 to 0.288 m during the

analysis. According to the criterion defined for the evolution of compressive buckling length, all concrete elements (up to 0.288 m height from the bottom) surrounding this longitudinal steel bar entered crushed phase, i.e., postpeak compressive regime. Comparing to the actual failure mode (figure 4.17 right), the predicted compressive buckling length is well consistent with the realistic failure mode of the region near web-toe experiencing crushing/spalling. This microscopic description of detailed damage on concretes and realistic illustration of longitudinal steel are all made accessible by the topological transition-based buckling model proposed herein.

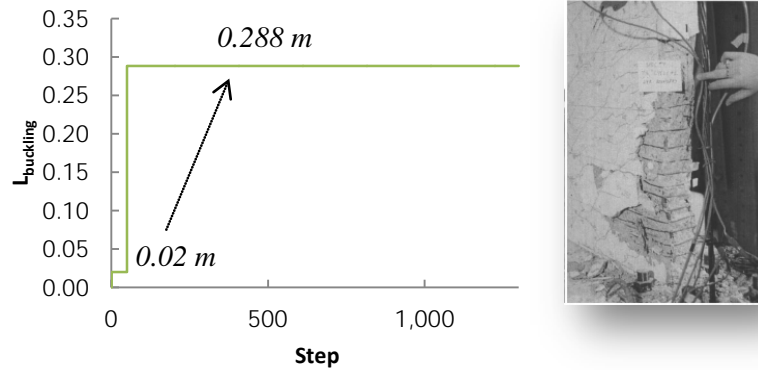


Figure 4.17. Evolution of compressive buckling length of the longitudinal steel at the outermost position of web toe; right inset shows actual damage states of the specimen (from Thomsen and Wallace 2004).

Chapter 5 CONCLUSION AND FUTURE DIRECTION

5.1 Conclusion

We presented the systematic review of existing microscopic analysis methodologies, with emphasis on quasi-brittle degrading materials, and placed the top priority on preserving “*physical counterparts*” when choosing and developing microscopic material models. In this effort, we have chosen the “*fixed-type*” multidirectional smeared crack model as the base mechanism to describe the degrading quasi-brittle materials, without losing the physical interpretation of real cracks normally found from structures exposed to cyclic loading. Following the central notion of smeared crack model, all the nonlinearity of material is described on the reduced crack surfaces and reliable microscopic stress update functions are harmoniously combined to give rise to an integrated normal stress-strain relationship on the crack surfaces.

3d interlocking model has been proposed to resolve the pathological problem of the fixed-type smeared crack model, notably by use of a tangible physical mechanism. Inspired by tribology, we adopted the fabric of rigid particle-soft matrix, of which interaction generates nonlinear shear stress on crack surfaces under cyclic loading. The Gaussian distribution has been adopted to generate random particle sizes, and then is distributed, notably over “*entire*” domain allowing realization of irregular asperity. Validation of the 3d interlocking mechanism against a well-known rough crack experiment reveals remarkable accuracy and possibility of the model.

Consumed energy based damage model has been suggested to fill the gap between the normal and shear stress on the crack surfaces, which are weakly correlated on the hybrid domain assumption. The damage model proposed herein was designed to hold a clear physical counterpart in evaluating the consumed energy on the crack surfaces. From the application to real-scale structure, the damage model shows strong influence on the “*sudden*” degradation phenomena in the postpeak regime.

Departing from well-established previous researches, we integrated the advantageous characteristics of reinforcing steel bar models, giving rise to a “*smart*” steel bar model. It is based

on the generalized Menegotto-Pinto steel model with evolving buckling length. Compressive buckling is taken into account in conjunction with progressive damage of surrounding quasi-brittle materials. Loss of adhesive energy of materials surrounding the longitudinal steel bars is interactively and comprehensively considered to determine realistic buckling length of the bars at a specific time. In some sense, we provided a systematic, novel union of the key ingredients of composite materials, which interact and exchange crucial information actively.

All aforementioned novelties in the analysis platform are all made possible by the problem-optimized parallel algorithms. During the optimization process of the parallel strategies we have obtained valuable understanding about parallel computing. In the quantitative comparison among representative parallel strategies, particularly in terms of factorization, some practical knowledge had been attained: (1) the performance of “*broadcasting*” strategy tends to deteriorate beyond a certain range of total processors; (2) contrary to anticipation, the most advanced “*look-ahead*” strategy appears to exhibit poor performance with a small number of processors; (3) only the “*pipelined*” strategy reveals overall stable performance. The pipelined factorization which was optimized herein has shown to successfully take advantage of penalty method and banded nature. Since the penalty method imparts remarkable smoothness to the global response, the parallel triangular system solving was able to achieve practical superiority over advanced parallel solvers such as parallel PCGM, as confirmed by quantitative comparison. The implemented “*divide-and-conquer*” approach for all other embarrassingly parallelizable tasks is performing favorably on the master-slaves concept after nonoverlapping uniform domain decomposition, especially for nonlinear element update. By this successful parallelization of nonlinear element update procedure, the developed parallel platform was able to be imbued with a multitude of physical mechanisms to describe progressive and localized damage phenomena at the entire system level.

Simulation of real-scale structures with the aid of the parallel platform is itself opening new possibility since uncompromised microphysical mechanisms and intrinsic randomness over “*entire*” domain are interacting in concert to give resultant nonlinear response—and the outcome appears to be promising.

The application was twofold: 3d H-shaped wall system and 4-story T-shaped wall system, both under cyclic loading. From the simulations, the well-known pathological nature of fixed-

type smeared crack model has been successfully resolved by the inclusion of 3d interlocking mechanism. It is fascinating to observe that the randomness of particles distributed over the entire domain for 3d interlocking mechanism appears to play an essential role to cause localized damage, while the damage would otherwise happen in a smoothly scattered manner.

5.2 *Future Directions*

As demonstrated so far, a harmonious combination of advanced parallel computing technology and microphysical mechanisms sparks our imagination to initiate a next generation parallel simulation platform. In particular, embracing more physical mechanisms pertaining to the lateral confinement effect, hydraulic pressure dependence, parallel nonlocal formulation, and so on, shall be a natural extension of the present work.

Furthermore, in future research, we hope to transplant the present parallel platform into a well-established FEA platform (e.g., *FRAME3D* or *OPENSEES*) for efficiently dealing with actual infrastructure exposed to extreme natural hazard. In this fashion, we can conduct hazard analysis of real infrastructure with unprecedented accuracy and efficiency. In particular, a major portion of the structural behavior is captured by the general FEA platform while only critical parts of the structure can be investigated by the parallel platform in great detail. To some extent, this can be thought of as a real-scale extension of the central notion of “*multiscale*” analysis technique.

As consistently addressed, the parallel simulation platform should be designed to incorporate as many physical mechanisms as possible rather than the traditional, compromised governing models. As such a novel philosophy flourishes, in the foreseeable future, we can conduct any kind of virtual experiments of any size and complexity with unprecedented accuracy at cheap cost—thus, “*virtual laboratory*” is rising.

Appendices

Appendix A Examples of Poisson Effect by Equivalent Strain Method

Example 1: Uniaxial Compression with Free Lateral Boundary

Provided that $\nu = 0.15$ and $\boldsymbol{\epsilon} = \{0.0006, 0.0006, -0.004, 0, 0, 0\}^T$, we obtain $\boldsymbol{\epsilon}^{cr} = \{0, 0, -0.004, 0, 0, 0\}^T$.

By $\boldsymbol{\epsilon}^{cr}$ calculated, we can perform nonlinear analysis with the microscopic stress functions and obtain the current compressive stress in crack direction as shown below. It should be noted that the lateral stresses are zero as expected by free boundary condition.

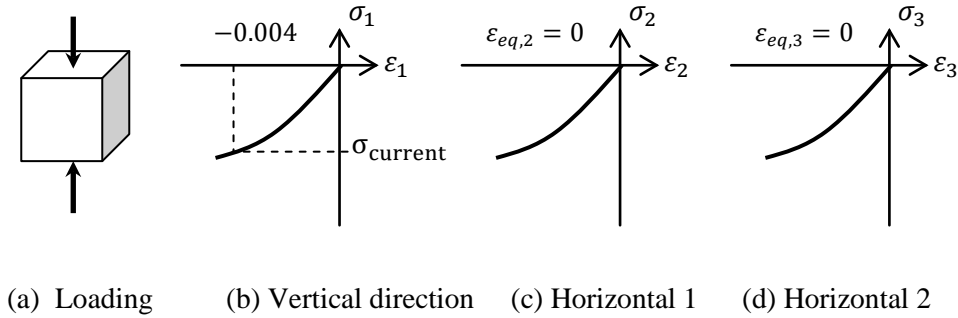


Figure A.1. Case of the uniaxial compression with free lateral boundary.

Example 2: Uniaxial Compression with Fixed Boundary Condition in the Lateral Directions

With $\nu = 0.15$, and $\boldsymbol{\varepsilon} = \{0, 0, -0.004, 0, 0, 0\}^T$, we can obtain

$$\boldsymbol{\varepsilon}^{cr} = \{-7.44 \times 10^{-4}, -7.44 \times 10^{-4}, -0.0042, 0, 0, 0\}^T.$$

As shown below, it should be noted that the resulting stresses in both horizontal directions have nonzero values as expected by constrained boundary conditions.

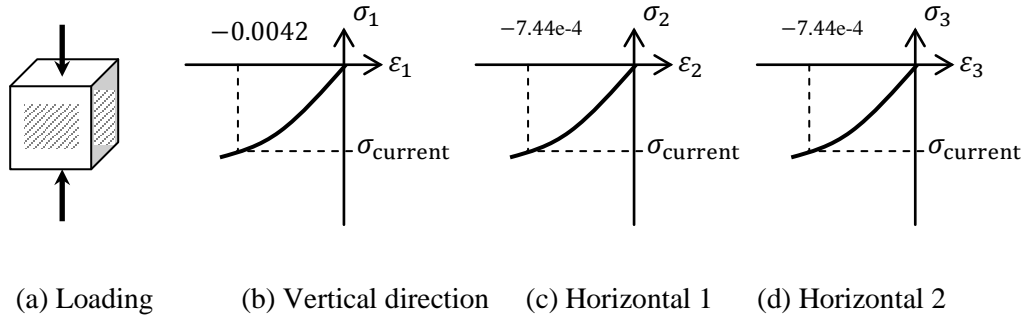


Figure A.2. Case of the fixed boundary condition.

Example 3: Unit Cube under Uniaxial Tension

Given $\nu = 0.15$, and $\boldsymbol{\varepsilon} = \{-0.00015, -0.00015, 0.001, 0, 0, 0\}^T$,

we can obtain $\boldsymbol{\varepsilon}^{cr} = \{0, 0, 0.001, 0, 0, 0\}^T$.

According to the resulting stresses shown below, we can confirm that the lateral stresses are zero as expected by free boundary condition, and the non-zero tensile stress within softening region.

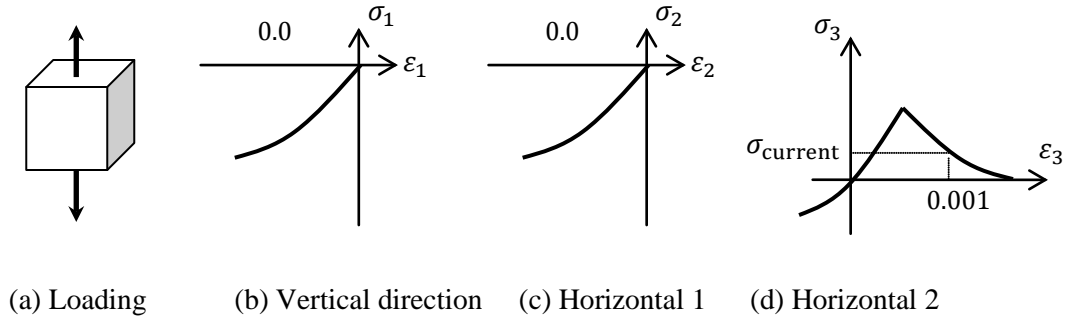


Figure A.3. Unit cube under uniaxial tension.

Appendix B Steel Bar Models

Type No. 21: Bilinear Steel Model

INPUT Form

Hysteresis number	Type number	A_s	σ_y	ε_y	c_0	(σ_u)
-------------------	-------------	-------	------------	-----------------	-------	--------------

Note: () means it can be omitted, and then default value will be used described below

- Hysteresis number = user defined sequential hysteresis number. Must be the same as the one designated in the material property

- Type number = 21

- A_s = Area of steel in $[m^2]$

- σ_y = Yielding stress in $[\frac{N}{m^2}]$

- ε_y = Strain at the yielding stress

- c_0 = Defined by $E_2/E_{initial}$

- σ_u = Ultimate tensile stress (if undeclared, set by unlimited value)

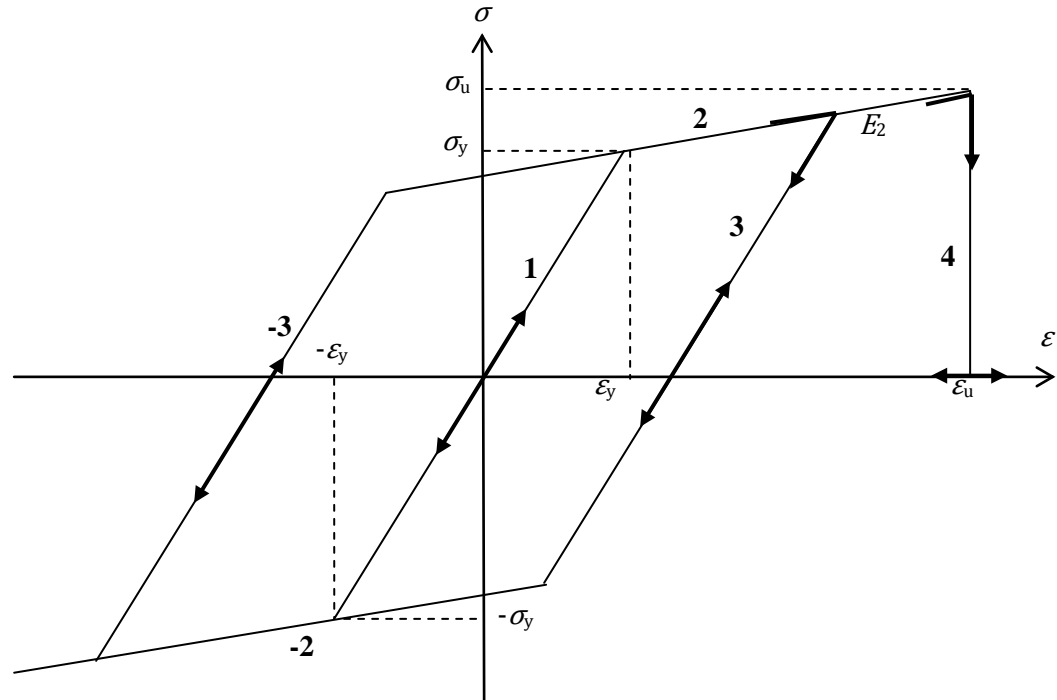


Figure B.1. Bilinear steel model with state indices.

Type No. 10001: Bilinear Steel Model with Compressive Buckling

INPUT Form

Hysteresis number	Type number	A_s	σ_y	ε_y	c_0	σ_u	c_1	c_2
-------------------	-------------	-------	------------	-----------------	-------	------------	-------	-------

- Hysteresis number = user defined sequential hysteresis number. Must be the same as the one designated in the material property

- Type number = 10001

(This type falls into the *longitudinal steel group* in which buckling length is updated by topological transition of surrounding elements of steel)

- A_s = Area of steel in $[m^2]$

- σ_y = Yielding stress in $[\frac{N}{m^2}]$

- ε_y = Strain at the yielding stress

- c_0 = Reduction factor for postyielding, hardening response, defined by E_2/E_s

- σ_u = Ultimate tensile stress

- $c_1(<0)$ = reduction factor for postbuckling, softening regime, used as $c_1 E_s$ (recommended 0.02)

- c_2 = factor for residual strength after buckling (recommended 0.2)

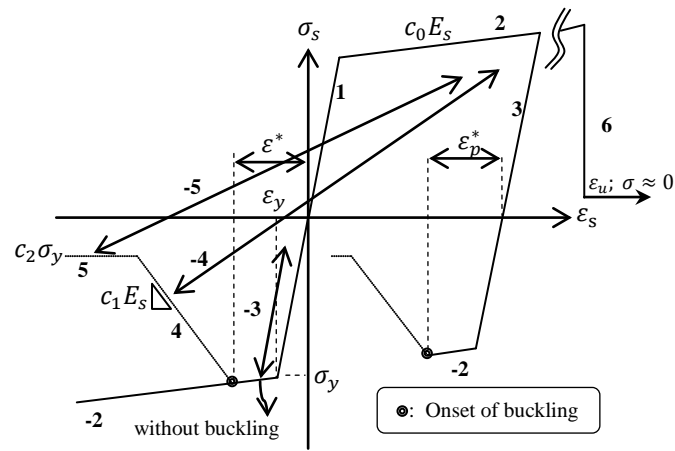


Figure B.2. Bilinear steel bar model incorporating compressive buckling with state indices.

Type No. 10002: Menegotto-Pinto Steel Model with Compressive Buckling

INPUT Form

Hysteresis number	Type number	A_s	σ_y	ε_y	b	σ_u	c_1	c_2
-------------------	-------------	-------	------------	-----------------	-----	------------	-------	-------

- Hysteresis number = user defined sequential hysteresis number. Must be the same as the one designated in the material property

- Type number = 10002

(This type falls into the *longitudinal steel group* in which buckling length is updated by topological transition of surrounding elements of steel)

- A_s = Area of steel in $[m^2]$

- σ_y = Yielding stress in $[\frac{N}{m^2}]$

- ε_y = Strain at the yielding stress

- b = Reduction factor for postyielding, hardening response, defined by E_2/E_s

- σ_u = Ultimate tensile stress

- $c_1(<0)$ = reduction factor for postbuckling, softening regime, used as $c_1 E_s$ (recommended 0.02)

- c_2 = factor for residual strength after buckling (recommended 0.2)

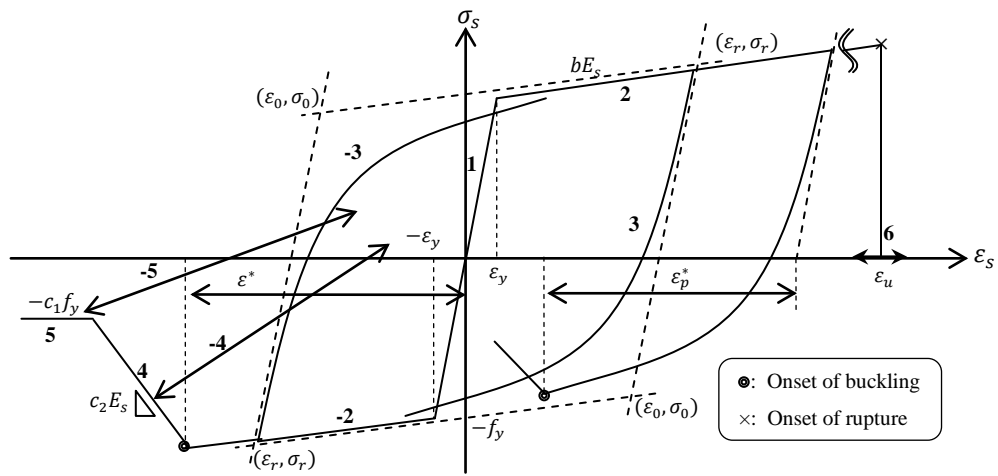


Figure B.3. Menegotto-pinto steel bar model incorporating compressive buckling with state indices.

Appendix C Detailed Pseudocodes of Parallel Factorizations

1. Simple Broadcasting-Based LU Factorization for Banded System

Let us define a function $q = k \bmod p$, which returns index of the processor containing the k_{th} column in order to broadcast the column k to all processors. Particularly, variables and executions pertaining to consideration of banded nature of the system are written in red color.

$[A] (n, r)$ *//local memory for $r (=n/p)$ columns of global $[A](n,n)$. note index is $0 \sim n-1$, $0 \sim r-1$*

$\{\text{Buffer}\} (n)$ *//temporary array to broadcast noncontiguous elements in bulk by single call*

Note: an alternative to this is n individual broadcast, however, network latencies are typically expensive than cost for memory copy

Table C.1. Pseudocode of broadcasting-based parallel factorization for banded system

```

Nband = Maximum bandwidth
 $q$  = my node number
 $p$  = total node number
 $l = 0$ 
//l is the index indicating the next columns to be updated in the local memory and being incremented by 1 after calling

For  $k=0$  to  $n-2$ 
    n_min = min(Nband-1,  $n-k-1$ ) //number of essential subelements to be updated
                                     //i.e., smaller one between bandwidth and remaining subrows

    if  $k = q \bmod p$  // number of processor containing  $k_{th}$  column =  $ALLOC(k)^{(root)}$ 
        PREP( $k$ ): i_temp=0
        For  $i=k+1$  to  $n-1$  //for elements below the  $k_{th}$  diagonal term in  $k_{th}$  column
             $buffer[i-(k+1)] = a_{il} = -a_{il}/a_{kl}$ 
            i_temp++; if(i_temp = n_min) break //loop for only essential element

         $l++$  // incremented and stored as local static matrix

    MPI_Bcast(buffer, n_min, MPI_DOUBLE,  $ALLOC(k)^{(root)}, \dots$ ) //previously (n-k-1)

    For  $j=l$  to  $r-1$  //since local [A] has r columns and update needs only for (r-l) last ones
        UPDATE( $k,j$ ): i_temp=0
        For  $i=k+1$  to  $n-1$ 
             $a_{ij} = a_{ij} + buffer[i - (k + 1)] \times a_{kj}$ 
            i_temp++; if(i_temp = n_min) break //loop for only essential element

End

```

2. Pipelining-Based LU Factorization for Banded System

As in the broadcasting scheme, variables and executions pertaining to the consideration of banded nature of the system are written in red color. It should be noted that for logical topology this scheme necessitates a special function $f(q)$ which provides each processor the numbers of logically nearest processors—sender and receiver denoted as P_{from} and P_{next} herein.

Table C.2. Pseudocode of pipelining-based parallel factorization for banded system

```

Nband = Maximum bandwidth
 $q$  = my node number
 $p$  = total node number
 $l = 0$ 
//l is the index indicating the next columns to be updated in the local memory and being incremented by 1 after calling

For  $k=0$  to  $n-2$ 

    n_min = min(Nband-1,  $n-k-1$ )           //number of essential sub elements to be updated
                                           //i.e., smaller one between bandwidth and remaining sub rows

    if  $q = k \bmod p$                           // number of processor containing  $k_{th}$  column
        PREP( $k$ ) : i_temp=0
        For  $i=k+1$  to  $n-1$                     //for elements below the  $k_{th}$  diagonal term in  $k_{th}$  column
            buffer[  $i-(k+1)$  ] =  $a_{il} = -a_{il}/a_{kl}$ 

            i_temp++; if(i_temp = n_min) break           //loop for only essential element

         $l++$                                 // incremented and stored as local static matrix
        MPI_Send(buffer, n_min, MPI_DOUBLE, Pnext(dest), ...) //previously, (n-k-1)
                                           //f(q) determines Pnext or Pfrom
    Else
        MPI_Recv(buffer, n_min, MPI_DOUBLE, Pfrom(root), ...) //previously, (n-k-1)
        If  $q \neq (k-1) \bmod p$                 //except the last processor on the current pipeline
            MPI_Send(buffer, n_min, MPI_DOUBLE, Pnext(dest), ...)

    For  $j=l$  to  $r-1$                           //since local [A] has r columns and update needs only for (r-l) last ones

        UPDATE( $k,j$ ): i_temp=0
        For  $i=k+1$  to  $n-1$ 
             $a_{ij} = a_{ij} + \text{buffer}[i - (k + 1)] \times a_{kj}$ 

            i_temp++; if(i_temp = n_min) break           //loop for only essential element

End

```

3. Look-Ahead Strategy for LU Factorization

The look-ahead method performs PREP() procedure and then sends the data during or before UPDATE() procedure as soon as it becomes ready to be sent to successor. It should be noted that in the pipeline algorithm PREP() procedure is carried out only after the current UPDATE() procedure in the processor is fully finished. In this way, the “*pipeline bubble*” of pipelining scheme can be remarkably reduced by the look-ahead scheme.

In the successive processor, which holds the column corresponding to the next diagonal term, the UPDATE() procedure is divided into two parts: (1) update only the column holding next diagonal term, (2) defer remaining UPDATE() procedure after PREP(). Therefore, the PREP() is followed by supplementary UPDATE() procedure which deals with the stored {buffer_rcv}.

As in the pipelined algorithm, the received buffer is immediately sent to successive processors. Also the local index l to indicate the remaining columns in each processor is used in this algorithm. This is equivalent to the expression, i.e., all j such that $j \bmod p = q$ & $j > k$, to find out column numbers to be updated in each processor.

Since on a processor two sending and receiving procedures can take place, this algorithm requires two separate buffers such as {buffer_rcv} and {buffer_send} whereas local memory $[A](n,r)$ is the same as other schemes.

{buffer_send} (n), {buffer_rcv}(n) //separate buffers for sending and receiving

Table C.3. Pseudocode of look-ahead strategy for parallel factorization

```

 $q$  = my node number
 $p$  = total node number
 $l = 0$  //  $l$  is the index indicating the next columns to be updated in the local memory and being
incremented by 1 after calling

For  $k=0$  to  $n-2$ 
  if  $q = k \bmod p$  // on processor containing  $k_{th}$  column
    PREP( $k$ , buffer_send) :
      For  $i=k+1$  to  $n-1$  //for elements below the  $k_{th}$  diagonal term in  $k_{th}$  column
        buffer_send[  $i-(k+1)$  ] =  $a_{il} = -a_{il}/a_{kl}$ 
       $l++$  //incremented by 1 to indicate the remaining columns to be updated

      MPI_Send(buffer_send, ( $n-k-1$ ), MPI_DOUBLE,  $P_{next}^{(dest)}$ , ...) //f( $q$ ) determines  $P_{next}$  or  $P_{from}$ 

  If  $k > 0$  //perform the delayed update for advanced PREP() while  $k=0$  this becomes unnecessary
    For  $j=l$  to  $r-1$  //For all  $j \bmod p = q$  &  $j > k$ 
      UPDATE( $k-1, j$ , buffer_rcv): //k-1 means previous delayed diagonal term
      For  $i=(k-1)+1$  to  $n-1$ 
         $a_{ij} = a_{ij} + \text{buffer\_rcv}[i - (k - 1 + 1)] \times a_{k-1,j}$ 

    For  $j=l$  to  $r-1$  // perform normal UPDATE() on the processor holding current diagonal

      UPDATE( $k, j$ , buffer_send):
      For  $i=k+1$  to  $n-1$ 
         $a_{ij} = a_{ij} + \text{buffer\_send}[i - (k + 1)] \times a_{k,j}$ 

  Else // on processors except the one containing  $k_{th}$  column
    MPI_Recv(buffer_rcv, ( $n-k-1$ ), MPI_DOUBLE,  $P_{from}^{(root)}$ , ...)
    If  $q \neq (k - 1) \bmod p$  //except the last processor on the current pipeline
      MPI_Send(buffer_rcv, ( $n-k-1$ ), MPI_DOUBLE,  $P_{next}^{(dest)}$ , ...)
    If  $q = (k + 1) \bmod p$  //for the successive proc holding next diagonal term defer the normal
      UPDATE() and do PREP() first in the following step
      UPDATE( $k, k+1$ , buffer_rcv): //UPDATE() only the col. corresponding to next diagonal
      For  $i=k+1$  to  $n-1$ 
         $a_{i,l} = a_{i,l} + \text{buffer\_rcv}[i - (k + 1)] \times a_{k,l}$ 
        //Note: in above, local index  $l$  points to the column possessing the next diag. term
        //and will be updated in the following PREP() procedure in the next step
    Else if  $q \neq (k + 1) \bmod p$  //for all other proc's do UPDATE() normally

      For  $j=l$  to  $r-1$  //For all  $j \bmod p = q$  &  $j > k$ 

        UPDATE( $k, j$ , buffer_rcv):
        For  $i=k+1$  to  $n-1$ 
           $a_{ij} = a_{ij} + \text{buffer\_rcv}[i - (k + 1)] \times a_{k,j}$ 

END

```

Appendix D Partial Pipelined Parallel Factorization for Banded System

(A) In Static Analysis: 1st Pipelined Factorization

The variables and executions pertaining to consideration of banded nature of the system are written in red color. It should be noted that for logical topology this scheme necessitates a special function $f(q)$ which provides each processor the number of logically nearest processors—sender and receiver denoted as P_{from} and P_{next} herein. Most of the code is similar to that of parallel pipelined factorization except STORE() procedure for storing essential part pertaining to penalty methods.

Table D.1. Pseudocode of 1st partial pipelined parallel factorization for banded system

```

Nband = Maximum bandwidth
 $q$  = my node number
 $p$  = total node number
 $l = 0$ 
//l is the index indicating the next columns to be updated in the local memory and being incremented by 1 after calling

On all Processors: LU_sub( $n-m$ ,  $r$ ) = 0.0    //storage for the following partial pipelined factorization

For  $k=0$  to  $n-2$ 

    n_min = min(Nband-1,  $n-k-1$ )    //number of essential sub elements to be updated
                                     //i.e., smaller one between bandwidth and remaining sub rows

    if  $q = k \bmod p$     // On the processor containing  $k_{th}$  diagonal term and its column
        PREP( $k$ ) : i_temp=0
        For  $i=k+1$  to  $n-1$     //for elements below the  $k_{th}$  diagonal term in  $k_{th}$  column
            buffer[  $i-(k+1)$  ] =  $a_{il} = -a_{il}/a_{kl}$ 

            i_temp++; if(i_temp = n_min) break    //loop only for essential element

             $l++$     // incremented and stored as local static matrix
            MPI_Send(buffer, n_min, MPI_DOUBLE, P_next(dest), ...)    //previously  $n-k-1$ 
        Else
            MPI_Recv(buffer, n_min, MPI_DOUBLE, P_from(root), ...)
            If  $q \neq (k-1) \bmod p$     //except the last processor on the current pipeline
                MPI_Send(buffer, n_min, MPI_DOUBLE, P_next(dest), ...)

            For  $j=l$  to  $r-1$     //since local [A] has  $r$  columns and update needs only for  $(r-l)$  last ones

                UPDATE( $k,j$ ): i_temp=0
                For  $i=k+1$  to  $n-1$ 
                     $a_{ij} = a_{ij} + \text{buffer}[i - (k + 1)] \times a_{kj}$ 

                    i_temp++; if(i_temp = n_min) break    //loop only for essential element

            If  $k=(m-1)$     //store sub matrix of LU( $n-m$ ,  $n-m$ ) after  $m-1$  step of factorization
                STORE:
                For  $i=m$  to  $(n-1)$     //sub rows
                    For  $j=l$  to  $(r-1)$     //sub column to be updated later
                        LU_sub[ $i-m$ ][ $j-l$ ] =  $a_{ij}$     //fill from LU_sub(0,0)

End

```

(B) In Nonlinear Analysis: 2nd Pipelined Factorization

Most of the code is similar to that of parallel pipelined factorization except RESTORE() procedure for pull back to the point of essential part pertaining to penalty methods and ADD() procedure to consider penalty element explicitly.

Table D.2. Pseudocode of 2nd partial pipelined parallel factorization for banded system

<i>l</i> is reset in RESTORE()	
RESTORE:	<i>//pullback to the point right after m-1 step of previous factorization</i>
<i>l</i> = from a function to get <i>l</i> for each processor	
For <i>i=m</i> to (<i>n-1</i>)	<i>//sub rows</i>
For <i>j=l</i> to (<i>r-1</i>)	<i>//sub column to be updated later</i>
$a_{ij} = \text{LU_sub}[i-m][j-l]$	
Undo $-L \rightarrow L$	<i>// corresponding parts only</i>
For <i>k=m</i> to <i>n-2</i>	
$n_min = \min(\text{Nband}-1, n-k-1)$	<i>//number of essential sub elements to be updated</i>
if $q = k \bmod p$	<i>//On the processor containing k_{th} diagonal term and column</i>
ADD(k) :	
if $k \in M, a_{kl} += \alpha$	<i>//add the stiff term to the diagonal;</i>
	<i>M is the set of penalty elements-related degree of freedom</i>
PREP(k) : $i_temp=0$	
For $i=k+1$ to $n-1$	<i>//ratio of k_{th} diagonal term to its sub column</i>
$buffer[i-(k+1)] = a_{il} = -a_{il}/a_{kl}$	
i_temp++ ; if($i_temp = n_min$) break	<i>//loop only for essential element</i>
$l++$	<i>// incremented and stored as local static matrix</i>
MPI_Send(buffer, n_min , MPI_DOUBLE, $P_{next}^{(dest)}, \dots$)	<i>//previously $n-k-1$</i>
Else	<i>//On all other processors</i>
MPI_Recv(buffer, n_min , MPI_DOUBLE, $P_{from}^{(root)}, \dots$)	
If $q \neq (k-1) \bmod p$	<i>//except the last proc on the current pipeline</i>
MPI_Send(buffer, n_min , MPI_DOUBLE, $P_{next}^{(dest)}, \dots$)	
For $j=l$ to $r-1$	<i>//since local [A] has r columns and update needs only for (r-l) last ones</i>
UPDATE(k,j): $i_temp=0$	
For $i=k+1$ to $n-1$	
$a_{ij} = a_{ij} + buffer[i-(k+1)] \times a_{kj}$	
i_temp++ ; if($i_temp = n_min$) break	<i>//loop only for essential element</i>
End	
if $q = (n-1) \bmod p$	
ADD(k=n-1) : if $k \in M, a_{kl} += \alpha$	<i>//add the stiff term to the last diagonal</i>

Bibliography

- Andrade, J. E., Baker, J. W., and Ellison, K. C. (2007). "Random porosity fields and their influence on the stability of granular media." *International Journal for Numerical and Analytical Methods in Geomechanics*, 32, 1147-1172.
- Bae, S., Miseses, A. M., and Bayrak, O. (2005). "Inelastic buckling of reinforcing bars." *Journal of Structural Engineering*, ASCE, 131(2), 314-321.
- Bažant, Z. P. (1984). "Size effect in blunt fracture: concrete, rock, metal." *Journal of Engineering Mechanics*, ASCE, 110(4), 518-535.
- Bažant, Z. P., and Gambarova, P. G. (1984). "Crack shear in concrete: Crack band microplane model." *Journal of Structural Engineering*, 110(9), 2015-2035.
- Bažant, Z. P., and Jirásek, M. (2002). "Nonlocal integral formulation of plasticity and damage: Survey of progress." *Journal of Engineering Mechanics*, 128(11), 1119-1149.
- Bazant, Z. P., and Oh, B. H. (1983). "Crack band theory for fracture of concrete." *Matériaux et Constructions*, 16(93), 155-177.
- Bažant, Z. P., Xiang, Y., and Prat, P. C. (1994). "Microplane model for concrete. I: Stress-strain boundaries and finite strain." *Journal of Engineering Mechanics*, 122(3), 245-254.
- Briseghella, L., and Gori, R. (1984). "Aggregate interlock cyclic response of R. C. critical section." *Proc., 8th World Conf. on Earthquake Engineering, San Francisco*, Englewood Cliffs, N. J., Prentice-Hall.
- Carmeliet, J., and de Borst, R. (1995). "Stochastic approaches for damage evolution in standard and non-standard continua." *Int. J. Solids Structures*, Vol. 32, No. 8/9, 1149-1160.
- Carol, I., and Prat, P. C. (1990). "A statically constrained microplane model for the smeared analysis of concrete cracking." *International Conference on Computer Aided Analysis and Design of Concrete Structures*, Vol. 2, 919-930.
- Casanova, H., Legrand, A., and Robert, Y. (2009). *Parallel Algorithm*. CRC Press.
- Chang, G., and Mander, J. (1994). "Seismic energy based fatigue damage analysis of bridge columns: Part I—Evaluation of seismic capacity." *NCEER Technical Rep. No. 94-0006*, Buffalo, N.Y.

- Cheng, F. Y., Mertz, G. E., Sheu, M. S., and Ger, J. F. (1993). "Computed versus observed inelastic seismic low rise RC shear walls." *Journal of Structural Engineering*, 119(11), 3255-3275.
- Clematis, A., Coda, A., and Spagnuolo, M. (1998). "Developing non-local iterative parallel algorithms for GIS on a workstation network." *Parallel and Distributed Processing (PDP)*, Proceedings of Sixth Euromicro Workshop, Madrid, Spain, 250-256.
- Colotti, V. (1993). "Shear behavior of RC structural walls." *Journal of Structural Engineering*, 119(3), 728-746.
- Cope, R. J., Rao, P. V., Clark, L. A., and Norris, P. (1980). "Modeling of reinforced concrete behavior for finite element analysis of bridge slabs." *Numerical Models for Nonlinear Problems I*, ed. Taylor *et al.*, 457-470.
- Crisfield, M. A. (1997). "Non-linear finite element analysis of solids and structures volume 2: Advanced topics." John Wiley & Sons Ltd., England, 135-157.
- Crisfield, M. A., and Wills, J. (1989). "Analysis of R/C panels using different concrete models." *J. Eng. Mech.*, 115(3), 578-597.
- Cundall, P. A., and Strack, O. D. L. (1979) "A discrete numerical model for granular assemblies." *Geotechnique*, **29**, 47-65.
- Cusatis, G., Bažant, Z. P., and Cedolin, L. (2003a). "Confinement-shear lattice model for concrete damage in tension and compression:I. Theory." *Journal of Engineering Mechanics*, 129(12), 1439-1448.
- Cusatis, G., Bažant, Z. P., and Cedolin, L. (2003b). "Confinement-shear lattice model for concrete damage in tension and compression:II. Computation and Validation." *Journal of Engineering Mechanics*, 129(12), 1449-1458.
- Danielson, K. T., Akers, S. A., O'Daniel, J. L., Adley, M. D., and Garner, S. B. (2008). "Large-scale parallel computation methodologies for highly nonlinear concrete and soil applications." *Journal of Computing in Civil Engineering*, 22(2), 140-146.

- Danielson, K. T., and Namburu, R. R. (1998). "Nonlinear dynamic finite element analysis on parallel computers using FORTRAN 90 and MPI." *Advances in Engineering Software*, Vol. 29, No. 3-6, 179-186, Published by Elsevier Science Ltd.
- Dhakal, R., and Maekawa, K. (2002a). "Modeling for postyielding buckling of reinforcement." *Journal of Structural Engineering*, 128, 1139-1147.
- Dhakal, R., and Maekawa, K. (2002b). "Reinforcement stability and fracture of cover concrete in reinforced concrete members." *Journal of Structural Engineering*, ASCE, 128(10), 1253-1262.
- de Borst, R. (2001). "Some recent issues in computational failure mechanics." *International Journal for Numerical Methods in Engineering*, 52, 63-95.
- de Borst, R., and Nauta, P. (1985). "Non-orthogonal cracks in a smeared finite element model." *Engineering Computations* 2, 33-46.
- de Borst, R., and Pamin, J. (1996). "Some novel developments in finite element procedures for gradient-dependent plasticity." *International Journal for Numerical Methods in Engineering*, 39, 2477-2505.
- DeGroot, A. J., Sherwood, R. J., Badders, D. C., and Hoover, C. G. (1997). "Parallel contact algorithms for explicit finite element analysis (DYNA3d)." *Proceedings of the Fourth U.S. National Congress on Computational Mechanics*, San Francisco.
- Elkadi, Ahmed S. K. (2005). "Fracture scaling of concrete under multiaxial compression." PhD thesis, Delft University of Technology (NL).
- Feenstra, P. H., Rots, J. G., Arnesen, A., Teigen, J. G., and Høiseth, K. V. (1998). "Computational modelling of concrete structures." Edited by René de Borst, *et al.*, Balkema, Rotterdam, 13-22.

- Gan, W., and Hall, J. F. (1995). "Static and dynamic behavior of steel braces under cyclic displacement." *Journal of Engineering Mechanics*, 124(1), 87-93.
- Geers, MGD, de Borst R., Brekelmans WAM, and Peerlings RHJ (1999). "Validation and internal length scale determination for a gradient damage model: Application to short glass-fibre-reinforced polypropylene." *International Journal of Solids and Structures*, 36, 2557-2583.
- Greenwood, J. A., and Williamson, J. B. P. (1966). "Contact of nominally flat surfaces." *Proc R Soc Lond A*, 295, 300-319.
- Gutiérrez, M. A., and de Borst, R. (1999). "Numerical Analysis of Localization using a Viscoplastic Regularization: Influence of Stochastic Material Defects." *International Journal for Numerical Methods in Engineering*, 44, 1823-1841.
- Hicher, P. Y. et al. (2008). "Constitutive Modeling of Soils and Rocks." Edited by Pierre-Yves Hicher and Jian-Fu Shao, ISTE Ltd. and John Wiley & Sons, 143-185.
- Hoover, C. G., DeGroot, A. J., Maltby, J. D., and Procassini, R. J. (1995). "ParaDyn-DYNA3d for massively parallel computers." *Engineering, Research, Development and Technology FY94*, Lawrence Livermore National Laboratory, UCRL 53868-94.
- Jackson, R. L., and Green, I. (2005). "A statistical model of elasto-plastic asperity contact between rough surfaces." *Tribology International* 39, 906-914.
- Jirásek, M. (1998). "Embedded Crack Models for Concrete Fracture." *Computational Modelling of Concrete Structures*, Balkema, Rotterdam.
- Jirásek, M., and Bažant, Z. P. (1995a). "Macroscopic fracture characteristics of random particle systems." *Int. J. Fract.*, 69(3), 201-228.

Jirásek, M. and Bažant, Z. P. (1995b). "Particle model for quasibrittle fracture and application to sea ice." *J. Eng. Mech.*, 121(9), 1016-1025.

Jirásek, M. and Zimmermann, T. (1998). "Rotating crack model with transition to scalar damage." *Journal of Engineering Mechanics*, 124(3), 277-284.

Karniadakis, G. E., and Kirby II, R. M. (2003). *Parallel Scientific Computing in C++ and MPI (A Seamless Approach to Parallel Algorithms and Their Implementation)*. Cambridge University Press.

Karsan, I.D., and Jirsa, J.O. (1969). "Behavior of Concrete under Compressive Loadings." *Journal of the Structural Division*, ASCE, 95(ST12).

Karypis, G., and Kumar, V. (1995a). "A fast and high quality multilevel scheme for partitioning irregular graphs." *Technical Rep. No. TR 95-035*, Dept. of Computer Science, University of Minnesota, Minneapolis.

Karypis, G., and Kumar, V. (1995b). "A parallel algorithm for multilevel graph partitioning and sparse matrix ordering." *Technical Rep. No. TR 95-036*, Dept. of Computer Science, University of Minnesota, Minneapolis.

Kawai, T. (1980) "Some consideration on the finite element method." *Int. J. Numer. Meth. Eng.*, **16**, 81-120.

Kelly, K. (1998). "The Third Culture." *Science*, 279(5353), 992-993.

Kim, S. W., and Vecchio, F. J. (2008). "Modeling of shear critical reinforced concrete structures repaired with fiber reinforced polymer composites." *Journal of Structural Engineering*, 134(8), 1288-1299.

Krishnan, S. (2010). "Modified Elastofiber Element for Steel Slender Column and Brace Modeling." *Journal of Structural Engineering*, 136(11), 1350-1366.

Kunnath, S. K., Heo, Y. A., and Mohle, J. F. (2009). "Nonlinear Uniaxial Material Model for Reinforcing Steel Bars." *Journal of Structural Engineering*, ASCE, 135(4), 335-343.

- Lasry, D., and Belytschko, T. (1988). "Localization limiters in transient problems." *International Journal of Solids and Structures*, 24, 581-597.
- Li, C. C., and der Kiureghian, A. (1993). "Optimal discretization of random fields." *J. Eng. Mech.* ASCE, 119(6), 1136-1154.
- Liu, Z., Neville, A., and Reuben R. L. (2000). "Analytical solution for elastic and elastic-plastic contact models." *Trib Trans*, 43(4), 627-634.
- Man, HK., and van Mier, J. G. M. (2008). "Size effect on strength and fracture energy for numerical concrete with realistic aggregate shapes." *International Journal of Fracture*, 154(1-2), 61-72.
- Menegotto, M., and Pinto, P. (1973). "Method of analysis of cyclically loaded RC plane frames including changes in geometry and nonelastic behavior of elements under normal force and bending." *Struct. Eng. Int. (IABSE, Zurich, Switzerland)*, 13, 15-22.
- Miehe, C., Dettmar, J., and Zäh, D. (2010). "Homogenization and two-scale simulations of granular materials for different microstructural constraints." *International Journal for Numerical Methods in Engineering*, Vol. 83, 1206-1236.
- Monti, G., and Nuti, C. (1992). "Nonlinear cyclic behavior of reinforcing bars including buckling." *Journal of Structural Engineering*, ASCE, 118(12), 3268-3284.
- Mühlhaus, H. B., and Aifantis, E. C. (1991). "A variational principle for gradient plasticity." *International Journal of Solids and Structures*, 28, 845-857.
- Namazifard, A., and Parsons, I. D. (2004). "A distributed memory parallel implementation of the multigrid method for solving three-dimensional implicit solid mechanics problems." *International Journal for Numerical Methods in Engineering*, 61, 1173-1208.

- Orakcal, K., and Wallace, J. W. (2006). "Flexural Modeling of Reinforced Concrete Walls—Experimental Verification." *ACI Structural Journal*, 103(2), 196-206.
- Ortiz, M. (1987). "An Analytic Study of the Localized Failure Modes of Concrete." *Mechanics of Materials* 6, 159-174.
- Palermo, D., and Vecchio, F. J. (2002). "Behavior of Three-Dimensional Reinforced Concrete Shear Walls." *ACI Structural Journal*, 99(1), 81-89.
- Pantazopoulou, S. J. (1998). "Detailing for reinforcement stability in RC members." *Journal of Structural Engineering*, ASCE, 124(6), 623-632.
- Peerlings, R. H. J., de Borst, R., Brekelmans, W. A. M., and de Vree, H. P. J. (1996). "Gradient-enhanced damage for quasi-brittle materials." *International Journal for Numerical Methods in Engineering*, 39, 3391-3403.
- Polycarpou, A. A., and Etsion, I. (1999). "Analytical approximations in modeling contacting rough surfaces." *ASME J Tribol.*, 121(2), 234-239.
- Rahul, and Suvranu De (2010). "An efficient coarse-grained parallel algorithm for global-local multiscale computations on massively parallel systems." *International Journal for Numerical Methods in Engineering*, 82, 379-402.
- Rashid, Y. R. (1968). "Ultimate strength analysis of prestressed concrete pressure vessels." *Nuclear Engineering and Design* 7, 334-344.
- Regan, P. (1971). "Shear in reinforced concrete." *Rep.*, Imperial College, London, England, 93-110.
- Reinhardt, H. W. (1984). "Fracture mechanics of an elastic softening material like concrete." *Heron* 29(2).
- Rodriguez, M. E., Botero, J. C., and Villa, J. (1999). "Cyclic stress-strain behavior of reinforcing steel including effect of buckling." *Journal of Structural Engineering*, ASCE, 125(6), 605-612.

- Rots, J. G. (1988). "Computational modeling of concrete fracture." PhD thesis, Delft University of Technology (NL).
- Selby, R. G., and Vecchio, F. J. (1993). "Three-dimensional Constitutive Relations for Reinforced Concrete." *Tech. Rep. 93-02*, University of Toronto, Dept. Civil Eng., Toronto, Canada.
- Selby, R. G., and Vecchio, F. J. (1997). "A constitutive model for analysis of reinforced concrete solid." *Can. J. Civ. Eng.*, Vol. 24, 460-470.
- Shahinpoor, M. (1980). "Statistical mechanical considerations on the random packing of granular materials." *Powder Technology*, 25, 163-176.
- Simo, J. C., and Ju, J. W. (1987a). "Strain- and Stress-Based Continuum Damage Models-I. Formulation." *Int. J. Solids Structures*, 23(7), 821-840.
- Simo, J. C., and Ju, J. W. (1987b). "Strain- and Stress-Based Continuum Damage Models-II. Computational Aspects." *Int. J. Solids Structures*, 23(7), 841-869.
- Sotelino, E. D. (2003). "Parallel Processing Techniques in Structural Engineering Applications." *Journal of Structural Engineering*, 129(12), 1698-1706.
- Spacone, E., and El-Tawil, S. (2004). "Nonlinear Analysis of Steel-Concrete Composite Structures: State of the Art." *Journal of Structural Engineering*, 130(2), 159-168.
- Steglich, D., Pirondi, A., Bonora, N., and Brocks, W. (2005). "Micromechanical modelling of cyclic plasticity incorporating damage." *International Journal of Solids and Structures*, 42, 337-351.

- Suda, K., Murayama, Y., Ichinomiya, T., and Shimbo, H. (1996). "Buckling behavior of longitudinal reinforcing bars in concrete column subjected to reverse lateral loading." *Proc. 11th World Conference on Earthquake Engineering*, Elsevier Science, New York, Amsterdam.
- Sziveri, J., and Topping, B. H. V. (2000). "Transient Dynamic Nonlinear Analysis Using MIMD Computer Architectures." *Journal of Computing in Civil Engineering*, 14(2), 79-91.
- Taucer, F., Spacone, E., and Filippou, F. C. (1991). "A Fiber Beam-Column Element for Seismic Response Analysis of Reinforced Concrete Structures." *UCB/EERC-91/17*.
- Thomsen IV, J. H. and Wallace, J. W. (1995). "Displacement-based design of reinforced concrete structural walls: Experimental studies of walls with rectangular and T-shaped cross sections." *Rep. No. CU/CEE-95/06*, Department of Civil and Environmental Engineering, Clarkson University, Potsdam, N. Y.
- Thomsen IV, J. H. and Wallace, J. W. (2004). "Displacement-Based Design of Slender Reinforced Concrete Structural Walls-Experimental Verification." *Journal of Structural Engineering*, 130(4), 618-630.
- Thorenfeldt, E., Tomaszewicz, A., and Jensen, J. J. (1987). "Mechanical properties of high-strength concrete and applications in design." In *Proc. Symp. Utilization of High-Strength Concrete*, Stavanger, Norway, Trondheim, Tapir.
- USGS/EERI Advanced Reconnaissance Team, *Team report (The M_w 7.0 Tahiti earthquake of January 12, 2010)*, V. 1.0, 2010.
- van Mier, J. G. M., van Vilet, M. R. A., and Wang, T. K. (2002). "Fracture mechanisms in particle composites: Statistical aspects in lattice type analysis." *Mech. Mater.*, 34(11), 705-724.
- Vecchio, F. J., and Collins, M. P. (1986). "The modified compression field theory for reinforced concrete elements subjected to shear." *ACI Journal* 83(22), 219-231.
- Vecchio, F. J., Omar, de la Peña, A. H., Bucci, F., and Palermo, D. (2002). "Behavior of Repaired Cyclically Loaded Shearwalls." *ACI Structural Journal*, 99(3), 327-334.

Walraven, J. C. (1981). "Fundamental analysis of aggregate interlock." *J. Struct. Div.*, ASCE, 107(11), 2245-2270.

Walraven, J. C. (1994). "Rough Cracks Subjected to Earthquake Loading." *Journal of Structural Engineering*, Vol. 120, No. 5, 1510-1524.

Weihe, S., König, M. and Kröplin, B. (1994). "A treatment of mixed mode fracture in debonding." *Computational Material Science* 3, 254-262.

Weihe, S., Kröplin, B., and de Borst, R. (1998). "Classification of smeared crack models based on material and structural properties." *International Journal of Solids and Structures*, 35(12), 1289-1308.

Wilkinson, B., and Allen, M. (1999). *Parallel Programming*. Prentice Hall.